A kinetic analysis of morphing continuum theory for fluid flows

by

Louis Blais Wonnell

B.S., Wake Forest University, 2010

M.S., University of California at San Diego, 2011

M.N.E., North Carolina State University, 2014

_____

AN ABSTRACT OF A DISSERTATION

submitted in partial fulfillment of the
requirements for the degree

DOCTOR OF PHILOSOPHY

Department of Mechanical and Nuclear Engineering
College of Engineering

KANSAS STATE UNIVERSITY
Manhattan, Kansas

2018

Abstract

To describe the behavior of a gas composed of spherical particles that rotate, the kinetic theory approach is presented. First-order approximations to the Boltzmann-Curtiss transport equation yield conservation equations that govern the translational velocity and rotation of the particles. The resulting equations match the form of the equations of morphing continuum theory (MCT), a theory derived from the principles of rational continuum thermomechanics. A direct comparison of corresponding terms provides expressions related to the new coefficients within MCT, showing a clear departure from classical expressions derived from a kinetic treatment of classical fluids. The identical expressions for the coefficients in the Cauchy stress and viscous diffusion terms in the kinetic linear momentum equation suggests that the coupling coefficient introduced by MCT outweighs the contribution of the classical kinematic viscosity. The kinetic theory equations reduce to the form of the Navier-Stokes equations when the local rotation is equated to the angular velocity, but the predominance of the coupling coefficient results in a viscous term that differs slightly from the classical expression derived using the Boltzmann distribution function. For simple cases of irrotational and incompressible flows, the kinetic equations mimic the form of the classical momentum equations derived from classical kinetic theory. This result is consistent with the fact that the difference between the two kinetic approaches is the local rotation of spherical particles.

Preliminary numerical simulations of the MCT governing equations are discussed, with an emphasis on the importance of the new coupling coefficient. Turbulent incompressible profiles are achieved by setting dimensionless parameters to particular values. The key parameter involves the ratio of the coupling coefficient to the kinematic viscosity. The relationship between the coupling coefficient and kinematic viscosity is shown to be the driving

force for the development of transitional and turbulent boundary layer profiles. Compressible turbulence results are generated using the same dimensionless parameter values that generated turbulence in the incompressible case. For supersonic flow over a cylinder, MCT displays an inverse energy cascade from small to large scales. In addition to visualizing turbulent processes, the results from MCT display the importance of coupling the linear and angular momenta equations, which is strengthened when the coupling coefficient increases. The expressions from kinetic theory coupled with the numerical results in MCT indicate that the physical phenomena driving a fluid composed of spherical particles depends heavily on the physical properties of the coupling coefficient.

A kinetic analysis of morphing continuum theory for fluid flows

by

Louis Blais Wonnell

B.S., Wake Forest University, 2010

M.S., University of California at San Diego, 2011

M.N.E., North Carolina State University, 2014

_____

A DISSERTATION

submitted in partial fulfillment of the
requirements for the degree

Doctor of Philosophy

Department of Mechanical and Nuclear Engineering
College of Engineering

KANSAS STATE UNIVERSITY
Manhattan, Kansas

2018

Approved by:

Major Professor
James Chen

Copyright

Abstract

To describe the behavior of a gas composed of spherical particles that rotate, the kinetic theory approach is presented. First-order approximations to the Boltzmann-Curtiss transport equation yield conservation equations that govern the translational velocity and rotation of the particles. The resulting equations match the form of the equations of morphing continuum theory (MCT), a theory derived from the principles of rational continuum thermomechanics. A direct comparison of corresponding terms provides expressions related to the new coefficients within MCT, showing a clear departure from classical expressions derived from a kinetic treatment of classical fluids. The identical expressions for the coefficients in the Cauchy stress and viscous diffusion terms in the kinetic linear momentum equation suggests that the coupling coefficient introduced by MCT outweighs the contribution of the classical kinematic viscosity. The kinetic theory equations reduce to the form of the Navier-Stokes equations when the local rotation is equated to the angular velocity, but the predominance of the coupling coefficient results in a viscous term that differs slightly from the classical expression derived using the Boltzmann distribution function. For simple cases of irrotational and incompressible flows, the kinetic equations mimic the form of the classical momentum equations derived from classical kinetic theory. This result is consistent with the fact that the difference between the two kinetic approaches is the local rotation of spherical particles.

Preliminary numerical simulations of the MCT governing equations are discussed, with an emphasis on the importance of the new coupling coefficient. Turbulent incompressible profiles are achieved by setting dimensionless parameters to particular values. The key parameter involves the ratio of the coupling coefficient to the kinematic viscosity. The relationship between the coupling coefficient and kinematic viscosity is shown to be the driving

force for the development of transitional and turbulent boundary layer profiles. Compressible turbulence results are generated using the same dimensionless parameter values that generated turbulence in the incompressible case. For supersonic flow over a cylinder, MCT displays an inverse energy cascade from small to large scales. In addition to visualizing turbulent processes, the results from MCT display the importance of coupling the linear and angular momenta equations, which is strengthened when the coupling coefficient increases. The expressions from kinetic theory coupled with the numerical results in MCT indicate that the physical phenomena driving a fluid composed of spherical particles depends heavily on the physical properties of the coupling coefficient.

Table of Contents

List of Figures

List of Tables

Acknowledgments

Chapter 1

Introduction

1.1 Motivation of this Work

A recurring difficulty for the theoretician is to obtain a comprehensive mathematical description of a complex, multiscale physical system. In turn, the numerical analyst desires to apply this model to this system in a robust, efficient manner and obtain data consistent with experimental data. The tension between these two goals increases as the complexity of the physical system increases. Existing mathematical terms in a theory may account for new physical phenomena, but the practical challenges of implementing the theory may lead researchers to introduce approximations or ad-hoc models for specific cases. While these modifications to the original theory may result in an efficient method of obtaining data for that specific case, the ad-hoc nature of the additional model can limit its repeated use. Therefore, alternative theories that mitigate the costs associated with precise descriptions of complex systems continue to advance the progress of their respective fields.

The historical success of the direct numerical simulation (DNS) of turbulent flows by solving the Navier-Stokes equations[1–7] ensures that researchers will continue to press for its use into modeling flows with lower Knudsen numbers, higher Mach numbers, and higher temperatures. In these flow regimes, the small-scale dynamics can affect the evolution of the mean flow.[8–11] As numerical analysts seek to make these extreme regimes more accessible to

current methods, the problem of resolving small length and time scales, and tracking how the physics at these scales affect the mean flow, will continue to strain the cost of computational resources involved in the application of DNS.

The key challenge in applying DNS to smaller length scales is that the smallest mesh element must be the size of the minimally relevant length. The difficulties of implementing DNS for turbulent flows are well documented,[12–17] and have led to modifications of the Navier-Stokes equations that help distinguish important length scales in the problem. The Reynolds-averaged Navier-Stokes equations (RANS) and large-eddy simulation techniques (LES) look to establish the presence of a mean flow through time-averaging the N-S equations or a minimal length scale through the process of filtering the N-S equations. Such theories are necessarily accompanied by closure models that approximate the dynamics at the length scales not covered by these models. Smagorinsky developed, in association with LES, the well-known eddy-viscosity model,[18] a model based on the assumption that turbulent kinetic energy and energy dissipation are at equilibrium. Germano et al noted that Smagorinsky's model did not incorporate energy transfer from small to large scales, and updated the eddy-viscosity subgrid model to relate sub-grid scale stresses to resolved turbulent shear stresses with an algebraic identity.[19] The universality of this model, however, was questioned when Lilly noticed that coefficients needed to be altered for shear-driven turbulent flows.[20] This effort to adjust and accomodate subscale flow with newer models underlies the problem associated with extending the Navier-Stokes equations to length scales of an individual particle or structure. The velocity perturbation introduced in RANS, for instance, emerges as a mathematical artifact from the time-averaging of the Navier-Stokes equations, and therefore is introduced as a mathematical term with no *a priori* physical meaning. Since its application is reserved exclusively for small-scale flow, however, the variable becomes useful for discussing the dynamics of subscale motion and the interactions between separate length scales within the flow. The chosen model for the velocity fluctuation still varies based on the chosen case.

The problem of accounting for small-scale dynamics within the Navier-Stokes equations becomes clear when looking at the theoretical approaches to deriving these equations. The

equations were originally derived from the assertion that a fluid can be described as a continuum, or a medium of infinitesimal points with no internal structure.[21] The governing equations were derived from balance laws applied to the continuum, and then expressed as partial differential equations for the macroscopic properties of the flow. Absent this abstract approach, the kinetic description employed Boltzmann's transport equation, characterizing a fluid as a distribution of point particles.[22] Taking moments of this transport equation with respect to conserved quantities the particles possess, i.e. mass or momentum, also yielded equations that mirrored the form of the Navier-Stokes equations. In both cases, the individual components of the system possessed no size, and therefore gave no explicit information on other degrees of freedom such as rotation or vibration, found in more complex systems. Therefore, numerical methods based on DNS must confront the burden of making the size of a cell small enough to capture the relevant physics at that scale.

1.2   Introduction to Morphing Continuum Theory

Recently, multiscale theories have been adopted to resolve, numerically, small-scale physics within complex flows.[17;23–25] A key attraction for incorporting multiscale theories into numerical simulations is the ability to track small-scale motion without developing an additional ad-hoc subgrid model. If the fluid can be envisioned as a body containing internal structure, numerical analysts can avoid the need to develop models for the behavior of that internal structure.

Morphing continuum theory (MCT) considers the fluid to be a space composed of spherical rotating bodies. These bodies can represent any fundamental structure that is of interest to the researcher. Since turbulent flows often depend on the behavior of the smallest relevant eddies, these spherical bodies can represent the smallest relevant eddies. Furthermore, collections of these spheres can accumulate to mimic the behavior of large eddies, which may themselves be composed of smaller eddies. Richardson noted that turbulent flows contain this inherent multiscale character, where the apparent smallest eddy in a turbulent flow may itself be composed of smaller eddies.[26] A key result from the description of a fluid as a set

of rotating spheres is that each point in the continuum contains its own rotation. Multiple points are not required, as in the classical case, to resolve the smallest length scales associated with rotation. The implications of this aspect of MCT for numerical simulations of turbulent boundary layers and small-scale interactions within turbulent flows will be discussed in later chapters.

The mathematical framework of MCT, due to this pointwise rotational component of the fluid description, includes an additional variable related to the gyration of the spherical bodies. The stress tensors affecting the linear and angular momentum of a fluid element incorporate this gyration, and an independent angular momentum equation governing the gyration is obtained. This additional equation is not present in the classical Navier-Stokes formulation, since angular momentum is described entirely by the vorticity. The angular momentum equation in MCT focuses specifically on the dynamics governing an individual particle's rotation, but does account for the effect of the vorticity on the gyration. Indeed, when the gyration becomes large enough, the vorticity is all that is required to describe the angular motion of the flow. Chapter 3 will demonstrate how the MCT governing equations lead to the Navier-Stokes equations when the gyration is equal to the angular velocity.

The independent angular momentum equation within MCT is accompanied by new stresses and strains related to the behavior of the gyration of the spherical bodies. The relationship between stresses and strains within MCT is characterized by new coefficients. A lingering problem in the analysis of MCT is the physical role these new coefficients play in complex flows. In particular, a coupling coefficient emerges that couples the linear and angular momentum equations and seems to add to the total viscosity of the fluid. This coefficient, in addition to additional stresses that MCT introduces with no classical counterpart, is currently described by its apparent impact on the physics of the flow when its value is modified. The kinetic approach is an attempt to characterize the new stresses and coefficients of MCT in terms of the physics of individual particle interactions.

1.3   The Kinetic Theory Approach

When particles contain additional independent motions, the Boltzmann transport equation can be extended to accomodate these motions, leading to the development of the Boltzmann-Curtiss transport equation.[27–31] If this kinetic approach can provide governing equations that match the form of governing equations derived from conservation laws, the multiscale framework of MCT retains a deeper physical meaning. Fluid properties and new coefficients in MCT are shown to be dependent on basic conditions in the system.

The extension of kinetic theory to flows composed of spherical particles is the main focus of this work. A simplified form of the Boltzmann-Curtiss transport equation is used to derive governing equations for this system, with an additional equation characterizing the new independent rotation these particles possess. These equations are obtained from a first-order approximation to the Boltzmann-Curtiss transport equation. With a careful series of assumptions, the form of the kinetic equations will be shown to match the form of the governing equations in MCT. The common terms in both equations allow for a direct comparison of the coefficients in MCT with corresponding expressions involving properties of the fluid.

The significance of new coefficients in MCT, and their relationship to traditional coefficients in N-S equations, can be discussed in more detail by showing how the kinetic theory equations reduce to the form of the Navier-Stokes equations. The assumptions behind the final form of the kinetic theory equations are clearly stated, with possible explanations given for disparities from classical expressions for corresponding material properties. The implications of these findings are investigated by simulating compressible and imcompressible flows using finite-volume solvers based on MCT. The MCT equations also reduce to the N-S form, allowing for an observation of the influence of the added rotation and new material properties.

Numerical simulations of MCT have produced turbulent boundary layer profiles only for certain values of the new coefficients in MCT. The expressions in the kinetic theory equations can give a physical basis for the relative magnitudes of these coefficients, and their

importance for producing turbulent profiles. The goal, then, will be to reduce the need for speculation of the values for the new coefficients within MCT, and to provide a further incentive to test its application to more complex flows. Providing this physical grounding for MCT will help ensure that multiscale theories such as MCT remain as an attractive option for tackling flows with local spin, reducing the need to incur the high costs associated with DNS or navigate the ad-hoc models needed to implement RANS or LES.

Chapter 2

The Kinetic Approach: Approximations to the Boltzmann-Curtiss Transport Equation

Flows with strong local spin have been the focus of extensive theoretical, experimental, and numerical work for decades.[32–37] High-speed, turbulent, compressible, reacting, and polyatomic gas flows all involve complex interactions based on strong local spin. The Wang Chan-Uhlenbeck equation accounts for molecular spin through the lens of quantum mechanics, treating each different quantum state as a separate species of molecule.[38] This additional rigor adds more complexity to the distribution function and the dynamics of the collisional integral. For classical physics, however, local rotation may affect the dynamics of the entire flow. Turbulent flows, in particular, may produce additional angular momentum from the smallest eddies. The rotation of these smallest eddies affects the energy and momentum transfer at the inertial length scales, requiring researchers to develop methods that capture this additional small-scale angular momentum. The most effective of these analytical methods have revealed deeper physical or mathematical characteristics to previously well-tested

theories of fluid dynamics.[32;39–43]

Several different fields of research have adapted to flows with local spin, by either modifying classical theories or developing entirely new approaches. Meng et al constructed a thermal lattice Boltzmann model based on the ellipsoidal statistical Bhatnagar-Gross-Krook (ES-BGK) equation to capture dynamics of rarefied gas thermal flows.[44] When these flows approach higher Mach numbers, the higher nonequilibrium flows were more difficult to capture in the transition regime without driving up computational costs. For hypersonic flows, Munafo et al proposed a Boltzmann rovibrational collisional coarse-grained model, which grouped internal energies associated with vibration and rotation into separate energy bins.[45] These groups of internal energies were treated as separate species. The main flow equation was simplified to a one-dimensional inviscid flow, also to save on computational resources. For polyatomic gases, theoretical approaches often treat local spin as an internal degree of freedom, similar to molecular vibration. Arima et al modified the approach of rational extended thermodynamics to treat the molecular and vibrational relaxation processes in polyatomic gases as separate processes, but included all effects of vibration and rotation in a separate variable denoting internal motions in the gas.[46] For rotation in nonequilibrium flows, Eu added to his generalized hydrodynamic relations[47;48] by introducing excess normal stress associated with a bulk viscosity.[49] Myong et al developed computational models based on Eu's relations to analyze high Knudsen number, rarefied diatomic gas flows.[50–52]

The models previously discussed have typically been modifications to classical approaches, treating rotation in separate closure models. The history of theoretical work on flows with local spin, however, shows that much can be learned about these flows by challenging the assumptions behind the classical approach. From the perspective of statistical mechanics, Grad developed the generalized thermodynamic relations for nonequilibrium distributions of molecules.[53] These relations were then applied to systems of molecules where individual molecules possessed internal rotation. When molecular rotation was treated as an internal variable dependent on the coordinates local to a molecule, the angular momentum equation's dependence on the linear momentum equation no longer held for nonequilibrium flows. Additionally, the pressure tensor become asymmetric due to the added internal rotation. De

Groot considered the effects of an asymmetric pressure tensor on the production of entropy, linear momentum, and angular momentum. The stresses produced by the difference between internal rotation and the vorticity in the flow were characterized by the "rotational viscosity."[54] Since this new coefficient appeared in the linear and angular momentum equations, the new parameter played the role of a coupling coefficient. Furthermore, when the material parameters were assumed to be homogeneous in space, the Navier-Stokes equations were recovered, with the rotational viscosity included.[54]

Snider later generalized this work to account for more complex rotational motions in anisotropic fluids, or fluids where the local equilibrium properties depended on the presence of this local spin.[55] At the small and large scales, fundamental forces and properties of the fluid are recharacterized when molecules possess strong internal spin. The pressure tensor becomes asymmetric, and the torque caused by local spin gives rise to a couple stress tensor. This couple stress is not to be confused with Stokes' formulation of the couple stress, which emerges from the vorticity vector.[56] Evans added depth to Snider and De Groot's work by calculating the transport coefficients in the linear constitutive equations that related stresses to deformations in the fluid.[57] Molecular dynamics simulations of dense polyatomic fluids between parallel plates produced preliminary data on the so-called "vortex viscosity," which corresponded to De Groot's coupling coefficient, and showed how the variable for internal rotation approached the angular velocity in the classical limit.[57] The characteristic time that the local rotation approached the macroscopic angular velocity was referred to as the relaxation time. De Groot and Evans both derived an expression for the relaxation constant for constant vorticity and zero classical viscosity.[54;57] For this simple case, the relaxation time was shown to be inversely proportional to the coupling coefficient. This analysis was the first indication that the return to equilbrium for these flows required a reformulation of the relaxation time. This concept will be treated with greater depth when the kinetic theory approach to polyatomic gases is discussed.

The presence of the new transport properties in multiple approaches to the problem of flows with local spin,[54;57] and their relevance to the departure from classical fluids suggests the need for a deeper treatment of their physical meaning. As has been shown for

the Navier-Stokes equations, the physics behind derived material constants can only come from an approach that achieves a macroscopic description of the fluid from modeling the interactions of individual particles. Maxwell and Boltzmann showed that these classical fluid descriptions could arise from the collisions of several particles in a monatomic gas.[58;59] Given enough collisions, a probability distribution function could predict how many particles would occupy a given point in space and possess a certain translational velocity. Maxwell and Boltzmann showed that a zeroth-order approximation of this distribution function demonstrates symmetries in physical and velocity space.[58;59] Furthermore, the substitution of the Maxwell-Boltzmann distribution into the balance laws for mass, momentum, and energy yield governing equations that take the form of the Euler equations. The first-order approximation to the exact solution to the Boltzmann transport equation, in turn, yields equations that mirror the Navier-Stokes formulation.

This initial work for monatomic gases expanded to fluids that contained particles with structure. Curtiss extended the Boltzmann transport equation to account for variables associated with separate internal motions apart from the translational velocity.[27–29] Additional rotation from diatomic molecules[27] and molecules of arbitrary structure[28] all resulted in additional terms to the Boltzmann transport equation, and complicated the physics behind collisional integrals and transport coefficients. The resulting transport equation became known as the Boltzmann-Curtiss tranpsort equation. From this bottom-up approach to flows with structure, Curtiss employed the Chapman-Enskog method[29] to obtain explicit expressions for the transport coefficients of a dilute gas mixture of rigid, non-spherical, symmetric-top molecules. Curtiss found that the resulting kinetic theory for this specific case matched the "loaded-sphere" formalism presented by Dahler and Sather.[60] She et al generalized this approach to molecules with arbitrary internal degrees of freedom with intermolecular central potential forces,[30] deriving a solution to the Boltzmann-Curtiss equation for molecules with translational and rotational motion. She also applied the Chapman-Enskog approach to find transport coefficients for this limited case.[30] When well-known potentials were substituted in for the perturbations to the equilibrium distribution, the resulting coefficients compared with well-known models such as the "rough-sphere" approximation. Solutions to the Boltzmann-

Curtiss equation that accounted for nonequilibrium entropy production consistent with the second law of thermodynamics were introduced by Eu[47;48] and investigated by Myong[50–52;61] for cases of high thermal nonequilibrium, where the complexity in the constitutive equations required a more in-depth theoretical and numerical treatment. The effects of rotational motion in Eu's solution were encapsulated by the rotational Hamiltonian, but the fluid was assumed to have no intrinsic angular momentum.[48]

The extension of kinetic theory to polyatomic gases also required a detailed investigation into the process of the gas departing from and returning to an equilibrium state. As mentioned in the statistical mechanical approach, the relaxation time typically gives a characteristic time for the return to equilibrium. In the classical approach, this relaxation time could be approximated as the time between two collisions. For the Boltzmann distribution, the only parameters needed to obtain this time were the mean free path and the most probable velocity value.[22] For kinetic theories involving local rotation as an independent variable, the transfer of kinetic energy between translation and rotation needed to be considered. Parker et al focused on deriving the rotational relaxation time for homonuclear diatomic molecules.[62] This description relied on the simplification that the translational energies already reached equilibrium, and that the rotational energy was initially unexcited. Furthermore, Parker did not consider rotation as a fundamental degree of freedom with its own equilibrium temperature.[62] In the loaded-sphere approximation, Dahler et al established local equilibrium temperatures for both translation and rotation, and derived the rotational relaxation time from an approximation of the rate of transfer of energy between these motions.[63] This approximation came from assuming a pair distribution for translation and rotation as the product of each of the two local Boltzmann distributions. Monchick et al was later able to establish singular relaxation times for rotation and other internal degrees of freedom based off of the Chapman-Enskog process to the linearized Boltzmann equation.[64] Determination of the relaxation time associated with rotation or vibration of gas molecules was determined experimentally via absorption of ultrasound frequencies and by measurements of heat conductivity.[65;66] Recently, molecular dynamics simulations have been performed to give better approximations of the rotational relaxation time[67] as well as other

11

transport properties such as the shear viscosity. Still, these methods treat rotation as an internal degree of freedom, and evaluate how well the values match with classical treatments of the rotation in the flow. The effects of molecular rotation to the total relaxation time of a polyatomic gas still require a more detailed treatment.

When rotation is treated as an internal or quantum state, the theoretician is challenged with the task of isolating its contribution from all other internal or quantum states. Distribution functions corresponding to each quantum state, as solutions to the Wang Chan-Uhlenbeck equation are formulated,[38] must be obtained and compared with avaliable data. This challenge is eliminated if rotation is treated as an explicit, independent variable, allowing for a single distribution function to describe the small-scale rotation in the system. Recently, an additional theory derived from the perspective of rational continnum thermo-mechanics (RCT) has provided governing equations for the mass, momenta, and energy of a fluid composed of spherical particles.[32;40;41;68;69] These equations start from a description of the fluid that deviates from any classical mechanical fluid. In the framework of MCT, the fluid is now posed as a morphing continuum, composed of individual spheres that possess intrinsic rotation as a separate, independent motion. Similar to Snider's work,[55] the governing equations of morphing continuum theory (MCT) present a series of new coefficients directly related to the contribution of local spin to various stresses in the fluid. Chen showed that the inviscid equations of MCT could be derived from a zeroth-order approximation to the solution of the Boltzmann-Curtiss transport equation.[31] The meaning of the additional coefficients in MCT, and their precise contribution to turbulent flows with local spin, has yet to be explained through kinetic theory. Peddieson et al derived dimensionless parameters[70] that produced a range of boundary layer profiles, including profiles that demonstrated aspects of turbulence. Still, the choice of the values for these parameters was arbitrary, with no expectation for which material constants were indispensable for the generation of turbulent fluctuations. When governing equations derived from kinetic theory descriptions of a fluid mirror the form of similar equations derived from first principles, further insight into the role of new material constants arises. Material properties are shown to have intrinsic dependencies on other properties of the fluid. Furthermore, differences in the two sets

of equations may reveal hidden assumptions in the mathematical approach or the need for higher orders of accuracy in the kinetic theory description. The focus of this paper is to apply the Chapman-Enskog approach from kinetic theory to extend Chen's analysis of fluids with spherical particles to the first-order approximation to the Boltzmann-Curtiss transport equation. The final form of this approximation is intended to give a deeper insight into the new coefficients introduced by MCT, and to present a kinetic description of a fluid possessing independent local rotation. The benefit of this approach of treating the local rotation as independent will be evident as the need for developing complex constitutive relations is avoided. These first-order equations should possess familiar terms from the Navier-Stokes equations, and introduce key terms that arise from local rotation. An analysis of these new equations will require a discussion of the relaxation time used to make this first-order approximation, due to the presence of local rotation.

First, section 2.1 specifies the assumptions for the fluid and outlines the mathematical consequences of making these assumptions. The distribution function, conservation equations, and balance laws will obtain a certain form from these assumptions. In section 2.2, the first-order approximation to the distribution function is derived from the zeroth order balance laws by following the Chapman-Enskog approach. With the distribution function, the expressions for key stresses in the original balance laws are derived and discussed briefly. Then, section 2.3 derives the governing equations by substituting the stress tensors back into the original balance laws. A brief comparison with the Navier-Stokes and MCT linear momentum equations is done to highlight the new terms brought about by the local rotation of the spherical particles. In section 2.4, the physics underlying the new relaxation time is investigated. For section 2.5, the equivalence between the gyration and the macroscopic angular velocity results in a reduction of the governing equations to the Navier-Stokes description. These reduced equations, however, do not match classical kinetic equations obtained using the Boltzmann distribution function. The differences between these two sets of equations are explored. Finally, section 2.6 concludes by remarking on the next steps for verifying and expanding the influence of this work to pressing problems for turbulent flows and other flows involving strong local spin.

2.1 Background

For monatomic gases composed of infinitesimal particles, any kinetic theory needs to track only the position and translational velocity of the particles. These assumptions greatly simplify the probability distribution of particles, as well as the transport equation used to describe the evolution of that distribution. When the particles are given a finite size and allowed to rotate, additional motions bring additional degrees of freedom to the system. If the angular motion of the particles is independent from the translational motion and is dependent on its orientation, then the transport equation has the form:[28;68]

$$(\frac{\partial}{\partial t} + \frac{p_i}{m}\frac{\partial}{\partial x_i} + \frac{M_i}{I}\frac{\partial}{\partial \Phi_i})f = (\frac{\partial f}{\partial t})_{coll} \tag{2.1}$$

Here m denotes the mass of a particle, p_i represents the linear momentum, M_i the angular momentum, I the moment of inertia of a particle, and Φ_i the Euler angle with respect to the center of mass of the particle.

The solution $f(p_i, \Phi_i, x_i, t)$ gives the probability a particular particle will possess the values of the given variables, and generalizes the motion of the system by simplifying the interactions of individual particles. For instance, this solution is absent of dependencies on vibrational energy or vibrational motion, as the dynamics of individual collisions are assumed to be independent of these variables. The right-hand side of equation 2.1 accounts for the cumulative effect of collisons on the distribution. For this description, the particles are treated as spheres, so all axial orientations of the distribution are equivalent, i.e. independent of the Euler angle. Therefore, the Boltzmann-Curtiss transport equation becomes:

$$(\frac{\partial}{\partial t} + \frac{p_i}{m}\frac{\partial}{\partial x_i})f = (\frac{\partial f}{\partial t})_{coll} \tag{2.2}$$

Equilibirum solutions to this equation should look similar to the Maxwell-Boltzmann distribution function, as the remaining terms are concerned with linear momentum. Still, the presence of an independent angular rotation, ω_i, changes the distribution of kinetic energy of the particles. From Boltzmann's principle, the equilibrium solution to equation 2.2 can

14

be approximated as:[31]

$$f^0(x_i, v_i, \omega_i, t) = n(\frac{\sqrt{mI}}{2\pi\theta})^3 \, exp(-\frac{m(v'_l v'_l) + I(\omega'_p \omega'_p)}{2\theta}) \tag{2.3}$$

Here, the perturbed velocity, $v'_l = v_l - U_l$, for mean velocity U_l and the perturbed gyration, $\omega'_p = \omega_p - W_p$ for mean gyration W_p, are introduced. The form of this distribution function differs from the classical Boltzmann distribution function,[10;71] which assigns a 3/2 power to the terms in front of the exponential. The increased exponential in equation 2.3 arises due to the additional contribution to the momentum by the gyration, ω'_p. The number density, n, of the particles is found by integrating the distribution function f over all the perturbed variables, $\mathbf{v}'$ and ω', which is now a six-dimensional integral:

$$n = \int \int d^3 v' d^3 \omega' f^0 \tag{2.4}$$

The superscript indicates that this function only serves as a zeroth-order approximation to the true solution. In equation 2.3, the mean thermal energy θ, mean velocity and mean gyration are assumed to vary slowly in time due to the rapid number of collisions, ensuring a rapid return to equilibrium. The thermal energy, $\theta = kT$, contains the Boltzmann constant k and absolute temperature T. Classical kinetic approaches by Huang[22] and by Gupta et al for granular fluids[72] often group the Boltzmann constant with the characteristic temperature to focus on the thermal energy of the system. The velocity and gyration perturbations represent the rapid fluctuations of the spheres, and provide the main source of any dynamics at equilibrium. Furthermore, the moment of inertia of a sphere can be expressed in terms of a parameter j,[17] known as the microinertia. This parameter comes from the averaging of spatial coordinates attached to the sphere, allowing one to show that $j = \frac{2}{5}d^2$, where d is the diameter of the sphere.[17] Substituting $I = mj$ into equation 2.3 yields:

$$f^0(x_i, v_i, \omega_i, t) = n(\frac{m\sqrt{j}}{2\pi\theta})^3 exp(-\frac{m(v'_l v'_l + j\omega'_p \omega'_p)}{2\theta}) \tag{2.5}$$

This equilibrium distribution function represents the starting point for the kinetic theory derivation, providing an abstract description of the system. To account for the evolution of the physical motion of a particle, the balance laws must be derived. The average of a quantity A is here defined by the following expression:

$$\langle A \rangle = \frac{1}{n} \int \int A f(x_i, v_i, \omega_i, t) d^3 v' d^3 \omega' \tag{2.6}$$

where n is the number density of the particles and is found by integrating the distribution function f over all the perturbed variables, $\mathbf{v}'$ and ω'. The mean velocity and gyration are naturally obtained from $\langle \mathbf{v} \rangle$ and $\langle \omega \rangle$. Therefore, any balance laws governing the mean velocity and mean gyration must come by averaging the transport equation 2.2 for some conserved quantity $\chi(x_i, p_i)$:

$$\frac{\partial}{\partial t} \langle n\chi \rangle + \frac{\partial}{\partial x_i} \langle n \frac{p_i}{m} \chi \rangle - n \langle \frac{p_i}{m} \frac{\partial \chi}{\partial x_i} \rangle = 0 \tag{2.7}$$

Note that all potential time derivatives vanished as χ is a function of momentum and position alone. The collisional term emerging from the averaging of the right-hand side of equation 2.2 is also presumed to vanish, namely, $\langle \chi(x_i, p_i)(\frac{\partial f}{\partial t})_{coll} \rangle = 0$. Huang proved this statement for any conserved quantity,[22] and his proof will be discussed in section 2.2 when the effects of collisions are discussed in more detail.

The balance laws come by letting χ equal the conserved values of mass m, linear momentum $m(v_i + \epsilon_{ipl} r_l \omega_p)$, angular momentum $m r_i r_p \omega_p$ and total energy $m(e + \frac{1}{2} v_l' v_l' + r_p r_q \omega_p' \omega_q')$. The new velocity associated with the linear momentum arises from the combined motion of the classical translational velocity, v_i, and the contribution of the gyration to the total velocity, $\epsilon_{ipl} r_l \omega_p$.[73] The angular momentum is the standard expression involving the the cross product of the local angular velocity induced by the gyration, $r_p \omega_p$, and the radial coordinate emerging from the center of mass of the particle, r_i. The Levi-Civita tensor, ϵ_{ipq}, is used for

cross products of two vectors, and has the properties:

$$\epsilon_{ipq} = \begin{cases} +1, & \text{if } (i,p,q) = (x,y,z), (z,x,y), or \ (y,z,x) \\ -1, & \text{if } (i,p,q) = (y,x,z), (z,y,x), or \ (x,z,y) \\ 0, & \text{otherwise} \end{cases} \tag{2.8}$$

Finally, the conserved quantity of energy contains the kinetic energy associated with the local angular velocity, $r_n\omega_n$, and adds this to the traditional translational kinetic energy. Substituting the conserved quantities of mass, linear momentum, angular momentum, and energy for χ into the conservation equation 2.7 yields:

Continuity $\left(\chi_1 = m\right)$

$$\frac{\partial}{\partial t}\langle mn \rangle + \frac{\partial}{\partial x_i}\langle mnv_i \rangle = 0 \tag{2.9}$$

Linear Momentum $\left(\chi_2 = m(v_i + \epsilon_{ipl}r_l\omega_p)\right)$

$$\frac{\partial}{\partial t}\langle mnv_i \rangle + \frac{\partial}{\partial t}\langle mn\epsilon_{ipl}r_l\omega_p \rangle + \frac{\partial}{\partial x_l}\langle mnv_iv_l \rangle + \tag{2.10}$$
$$\frac{\partial}{\partial x_s}\langle mn\epsilon_{ipl}v_sr_l\omega_p \rangle = 0$$

Angular Momentum $\left(\chi_3 = mr_ir_p\omega_p\right)$

$$\frac{\partial}{\partial t}\langle mnr_ir_p\omega_p \rangle + \frac{\partial}{\partial x_l}\langle mnr_ir_p\omega_pv_l \rangle = 0 \tag{2.11}$$

Energy $\left(\chi_4 = m(e + \frac{1}{2}[v_l'v_l' + r_pr_q\omega_p'\omega_q'])\right)$

$$\frac{\partial}{\partial t}(mne) + \frac{\partial}{\partial x_i}(mnev_i) + \frac{\partial}{\partial x_i}\frac{1}{2}\langle mnv_l'v_l'v_i' + r_pr_q\omega_p'\omega_q'v_i' \rangle - \tag{2.12}$$
$$mn\langle v_i\frac{\partial e}{\partial x_i} \rangle = 0$$

Here e is internal energy and is already itself a mean quantity of the system. Since the velocity, $\mathbf{v}$, and gyration, ω, are separate coordinates, any derivative of the positional coordinate with respect to these variables vanishes. Letting the averages of the variables equal their mean values and splitting total variables into mean and fluctuating components, the balance

17

laws become:

Continuity

$$\frac{\partial}{\partial t}\rho + \frac{\partial}{\partial x_l}(\rho U_l) = 0 \tag{2.13}$$

Linear Momentum

$$\frac{\partial}{\partial t}(\rho U_s) + \frac{\partial}{\partial x_l}(\rho U_s U_l) + \frac{\partial}{\partial x_l}(\rho\langle v'_s v'_l\rangle + \langle \rho\epsilon_{spq}v'_l r_q \omega'_p\rangle) = 0 \tag{2.14}$$

Angular Momentum

$$\frac{\partial}{\partial t}(\rho i_{sp}W_p) + \frac{\partial}{\partial x_l}(\rho i_{sp}W_p U_l) + \frac{\partial}{\partial x_l}(\rho\langle i_{sp}\omega'_p v'_l\rangle) = 0 \tag{2.15}$$

Energy

$$\frac{\partial}{\partial t}(\rho e) + \frac{\partial}{\partial x_l}(\rho e U_l) + \frac{\partial}{\partial x_l}\frac{1}{2}\langle \rho v'_s v'_s v'_l + i_{pq}\omega'_q\omega'_p v'_l\rangle - \rho\langle v_l\frac{\partial e}{\partial x_l}\rangle = 0 \tag{2.16}$$

Here, the properties $\langle v'\chi\rangle = 0$ and $\langle \omega'\chi\rangle = 0$ are employed. Additionally, the term $\langle \epsilon_{ipl}v_s r_l W_p\rangle = 0$ as this can be viewed as an integral of the fluctuating component of the total velocity.[31;74] Also, the term $i_{pq} = r_p r_q$ is used to represent the product of the coordinates, r_p, emerging from the center of mass of the particle. These coordinates measure the relative deformation of a particle, tracking how the surface varies about the center of mass. The tensor i_{pq} is related to the earlier parameter j, known as the microinertia. For spherical particles, i_{pq} is reduced to $i_{pq}\delta_{pq} = i_{pp}$, which can be shown to equal $\frac{3j}{2}$.[17] Applying this

reduction to i_{pq} the balance laws become:

Continuity

$$\frac{\partial}{\partial t}\rho + \frac{\partial}{\partial x_l}(\rho U_l) = 0 \qquad (2.17)$$

Linear Momentum

$$\frac{\partial}{\partial t}(\rho U_s) + \frac{\partial}{\partial x_l}(\rho U_s U_l) + \frac{\partial}{\partial x_l}(\rho\langle v'_s v'_l\rangle + \langle\rho\epsilon_{spq}v'_l r_q \omega'_p\rangle) = 0 \qquad (2.18)$$

Angular Momentum

$$\frac{\partial}{\partial t}\left(\frac{3\rho j W_s}{2}\right) + \frac{\partial}{\partial x_l}\left(\frac{3\rho j W_s U_l}{2}\right) + \frac{\partial}{\partial x_l}\rho\langle\frac{3j\omega'_s v'_l}{2}\rangle = 0 \qquad (2.19)$$

Energy

$$\frac{\partial}{\partial t}(\rho e) + \frac{\partial}{\partial x_l}(\rho e U_l) + \frac{\partial}{\partial x_l}\frac{1}{2}\langle\rho v'_s v'_s v'_l + \frac{3j\omega'_p\omega'_p v'_l}{2}\rangle - \rho\langle v_l\frac{\partial e}{\partial x_l}\rangle = 0 \qquad (2.20)$$

These conservation equations feature material derivatives for the mean flow variables as well as gradients of products of perturbed variables. These perturbations are variables in the distribution function, and so can be treated separately. Defining these expressions in the following way:

$$q_\alpha = \frac{1}{2}\langle\rho v'_l v'_l v'_\alpha + \frac{3j\omega'_p\omega'_p v'_\alpha}{2}\rangle \qquad (2.21)$$

$$t^{\text{Bol}}_{\alpha\beta} = -\rho\langle v'_\alpha v'_\beta\rangle \qquad (2.22)$$

$$t^{\text{Cur}}_{\alpha\beta} = -\rho\langle v'_\alpha\epsilon_{\beta pq}r_q\omega'_p\rangle \qquad (2.23)$$

$$m_{\alpha\beta} = -\rho\langle\frac{3j\omega'_\beta v'_\alpha}{2}\rangle \qquad (2.24)$$

Here, q_α denotes the heat flux, $t^{\text{Bol}}_{\alpha\beta}$ gives the Boltzmann stress, $t^{\text{Cur}}_{\alpha\beta}$ yields the Curtiss stress, and $m_{\alpha\beta}$ introduces the moment stress. Plugging these expressions into the balance laws

gives:

Continuity

$$\frac{\partial}{\partial t}\rho + \frac{\partial}{\partial x_l}(\rho U_l) = 0 \tag{2.25}$$

Linear Momentum

$$\frac{\partial}{\partial t}(\rho U_s) + \frac{\partial}{\partial x_l}(\rho U_s U_l) - \frac{\partial}{\partial x_l}(t_{ls}^{\text{Bol}} + t_{ls}^{\text{Cur}}) = 0 \tag{2.26}$$

Angular Momentum

$$\frac{\partial}{\partial t}(\rho j W_s) + \frac{\partial}{\partial x_l}(\rho j W_s U_l) - \frac{2}{3}\frac{\partial}{\partial x_l}(m_{ls}) = 0 \tag{2.27}$$

Energy

$$\frac{\partial}{\partial t}(\rho e) + \frac{\partial}{\partial x_l}(\rho e U_l) + \frac{\partial q_l}{\partial x_l} - \rho\langle v_l \frac{\partial e}{\partial x_l}\rangle = 0 \tag{2.28}$$

Indeed, the expressions 2.21, 2.22, 2.23, and 2.24 refer to familiar stresses that require a more detailed treatment. At the moment, they represent only source or sink terms for the momentum and energy of the flow. These terms can be determined from the definition of the average in equation 2.6 using the equilibrium distribution in equation 2.5, which would give a very rough approximation of how they contribute to the balance laws. A more thorough treatment of their contribution, however, requires the derivation of a distribution function that accounts for departures in the fluid from equilibrium. For this function, the Chapman-Enskog process is followed to derive a first order approximation to the solution of the Boltzmann transport equation 2.2.

2.2 First-Order Approximation

2.2.1 Distribution Function

The right-hand side of the transport equation 2.2 tracks the gain or loss of particles due to collisions in some small time interval. For the equilibrium distribution function in equation 2.5, the assumption was made that a large number of binary collisions occurred over

a short time interval, meaning that any deviation from equilibrium would result in a rapid return to equilibrium. These binary collisions affect the initial rotation and velocity of the particle instantaneously at the moment the particles collide. Huang studied these binary collisions considering molecules with only translational velocities.[22] The existence of spin within molecules was treated through the lens of quantum mechanics, denoting different spin states as separate species of molecules. In order to account for these different spins, then, one would need to solve the Wang Chang-Uhlenbeck equation[38] for the distribution function of each of these molecular species, with a collisional integral that accounts for the cross-section calculated from the quantum states of these species. Here, the Boltzmann-Curtiss distribution function described in equation 2.5 treats gyration as an additional classical variable applicable to the same molecules throughout the domain, thus requiring only one solution to describe the distribution of rotation throughout the system. Additionally, the collisional integral is easier to calculate since the rotational motion is treated as a classical motion.

The collision rate on the right-hand side of the Boltzmann transport equation 2.2 is given by the following integral:

$$(\frac{\partial f}{\partial t})_{coll} = \int d^3p_2 \; d^3p'_1 \; d^3p'_2 \; \delta^4(P_f - P_i) \left|T_{fi}\right|^2 (f'_2 f'_1 - f_2 f_1) \qquad (2.29)$$

Here, P_f and P_i refer to the total final and initial momenta, p_1 and p_2 refer to the initial momenta of the colliding particles while their primed counterparts, p'_1 and p'_2 each refer to their respective final linear momentum. As mentioned in the previous section, these linear momenta contain an added term to the classical linear momentum, $p_i = mv_i$, found in the Boltzmann transport equation. Here, the Boltzmann-Curtiss linear momentum, $p_i = m(v_i + \epsilon_{ipl}r_l\omega_p)$, includes an additional contribution from the component of the local rotation moving in the direction of the translational velocity. The transition matrix T_{fi} contains the elements of the operator $T(E)$ that converts the particle from its initial to final state in the collision. Finally the distribution functions f_1 and f_2 refer to the distributions of particles containing momenta p_1 and p_2 respectively while the primed distribution functions contain the final momenta values denoted by the primed counterparts p'_1 and p'_2. Any conserved quantity for a particle initiating a binary collision, χ, integrated with the collision integral 2.29 vanishes.

Hunag proved this result by interchanging the momenta variables before and after the collison and integrating over pre-collision and post-collision linear momenta.[22] When equation 2.29 is used on the right-hand side of the Boltzmann-Curtiss transport equation 2.2, the Wang Chan-Uhlenbeck equation is obtained:[38]

$$(\frac{\partial}{\partial t} + \frac{p_i}{m}\frac{\partial}{\partial x_i})f = \int d^3p_2 \, d^3p_1' \, d^3p_2' \, \delta^4(P_f - P_i) \, |T_{fi}|^2 \, (f_2'f_1' - f_2f_1) \tag{2.30}$$

This treatment will look at a simplified version of this equation.

In observing the effect of collisions on equation 2.30, it is important to recognize that $(\frac{\partial f^0}{\partial t})_{coll} = 0$ for the equilibrium Boltzmann-Curtiss distribution function defined in equation 2.5. This result emerges from the fact that the coefficients in equation 2.5 do not depend on the velocity v_i.[22] To get a good approximation of the collision integral 2.29, higher order approximations of f are needed. If the distribution function g is defined by the expression:

$$g(x_i, p_i, t) = f(x_i, p_i, t) - f^0(x_i, p_i, t) \tag{2.31}$$

then the collision integral 2.29 can be approximated with the following expression:

$$(\frac{\partial f}{\partial t})_{coll} \approx \int d^3p_2 \, d^3p_1' \, d^3p_2' \, \delta^4(P_f - P_i)|T_{fi}|^2(f_2^{0'}g_1' - f_2^0g_1 + g_2'f_1^{0'} - g_2f_1^0) \tag{2.32}$$

where squared terms involving g have been neglected due to their presumed smaller magnitude in relation to f^0. Indices associated with different distribution functions again correspond to the initial and final distributions of the particles in the binary collisions. To assess the relative magnitude of the terms within equation 2.32, the second term on the right-hand side can be calculated by the expression:

$$- g_1(\mathbf{x}, \mathbf{p}_1, t) \int d^3p_2 \, d^3p_1' \, d^3p_2'[\delta^4(P_f - P_i) \, |T_{fi}|^2 \, f_2^0 = -\frac{g_1}{\tau} \tag{2.33}$$

Here, the time constant τ incorporates all the physics associated with the transition from initial to final states, including the transfer of angular momentum through the new variable of gyration. A more in-depth treatment of the gyration and the characteristic time constants associated with its evolution will be given in the next section.

Given the order-of-magnitude estimate to the collision integral 2.32, the right-hand side of the Boltzmann transport equation can be given a simpler treatment with the expression:

$$(\frac{\partial f}{\partial t})_{coll} = -\frac{f - f^0}{\tau} = -\frac{g}{\tau} \tag{2.34}$$

The first-order distribution function, g, measures the probability that large numbers of particles will exit their equilibrium state purely through collisions. The time constant τ now gives an approximation for the entire distribution departing from equilibrium through collisions. Therefore, this time constant should characterize the transition of all degrees of freedom to and from their equilibrium states. If the time-scale of the problem is reduced such that only one motion departs from equilibrium, as Parker considered for internal rotation,[62] then this time constant can be scaled to focus on this relaxation process. If further approximations are needed to account for additional physics, the relaxation time can be expanded into a series of terms that take into account these additional interactions. Chen et al applied this approach[75] to generate an expression for the characteristic collisional time scale of turbulent eddy interactions. Such expansions have the benefit of incorporating multiple physical processes within one time constant, allowing for the interaction of rotation and translation to affect the relaxation of the distribution function simultaneously.

If equation 2.34 is substituted into the transport equation 2.2, an approximate form of the transport equation known as the Bhatnagar, Gross, and Krook (BGK) equation is obtained:[76]

$$g = -\tau(\frac{\partial}{\partial t} + v_i \frac{\partial}{\partial x_i})(f^0 + g) \tag{2.35}$$

Since g measures the probability of large numbers of particles deviating from their equilibrium state, its relative magnitude to f^0 matters greatly in terms of what kind of system is being described. For this paper, it suffices to show what forces and properties are influencing the mean flow when slight deviations to equilibrium occur. Therefore, it can be assumed that $g << f^0$, reducing equation 2.35 to the form:

$$g = -\tau(\frac{\partial}{\partial t} + v_i \frac{\partial}{\partial x_i})f^0 \tag{2.36}$$

This equation gives a formula for finding g entirely in terms of derivatives of f^0. Still, the variables in the transport equation 2.36 are present in f^0 only through its independent variables. Therefore, to get the spatial derivates of f^0, the following derivatives of its independent variables are calculated:

$$\frac{\partial f^0}{\partial \rho} = \frac{f^0}{\rho} \tag{2.37}$$

$$\frac{\partial f^0}{\partial \theta} = -(3 - \frac{m(v'^2 + j\omega'^2)}{2\theta})\frac{f^0}{\theta} \tag{2.38}$$

$$\frac{\partial f^0}{\partial U_i} = \frac{mv'_i}{\theta}f^0 \tag{2.39}$$

$$\frac{\partial f^0}{\partial W_i} = \frac{mj\omega'_i}{\theta}f^0 \tag{2.40}$$

Using the chain rule, the expression for g in equation 2.36 can be written as:

$$\begin{aligned} g = -\tau f^0(\frac{1}{\rho}D(\rho) + \frac{1}{\theta}(\frac{m(v'^2 + j\omega'^2)}{2\theta} - 3)D(\theta) + (\frac{mv'_i}{\theta})D(U_i) \\ + (\frac{mj\omega'_i}{\theta})D(W_i)) \end{aligned} \tag{2.41}$$

where $D(X) = (\frac{\partial}{\partial t} + v_i\frac{\partial}{\partial x_i})X$. The material derivatives present in equation 2.41 can be derived from the zeroth order balance laws. To obtain the zeroth order approximations of the equations 2.25, 2.26, 2.27, 2.28, the terms related to the perturbation of the velocity and gyration are eliminated, yielding:

$$\frac{\partial \rho}{\partial t} + \frac{\partial \rho U_l}{\partial x_l} = 0 \tag{2.42}$$

$$\frac{\partial}{\partial t}(\rho U_s) + \frac{\partial}{\partial x_l}(\rho U_l U_s) = -\frac{\partial}{\partial x_s}(n\theta) \tag{2.43}$$

$$\frac{\partial}{\partial t}(\rho j W_s) + \frac{\partial}{\partial x_l}(\rho j W_s U_l) = 0 \tag{2.44}$$

$$\frac{\partial}{\partial t}(n\theta) + \frac{\partial}{\partial x_l}(n\theta U_l) = -\frac{n\theta}{3}\frac{\partial U_q}{\partial x_q} \tag{2.45}$$

From these approximations to the balance laws, the material derivatives found in equa-

tion 2.41 are obtained:

$$D(\rho) = v_l'\frac{\partial}{\partial x_l}\rho - \rho\frac{\partial U_q}{\partial x_q} \tag{2.46}$$

$$D(\theta) = v_l'\frac{\partial}{\partial x_l}\theta - \frac{1}{3}\theta\frac{\partial U_q}{\partial x_q} \tag{2.47}$$

$$D(U_i) = v_l'\frac{\partial}{\partial x_l}U_i - \frac{1}{\rho}\frac{\partial}{\partial x_i}(n\theta) \tag{2.48}$$

$$D(W_i) = v_l'\frac{\partial}{\partial x_l}W_i \tag{2.49}$$

With these final expressions substituted back into equation 2.41, the final form of g is given as:

$$\begin{aligned}
g = -\tau f^{(0)}[\frac{1}{\rho}(v_i'\frac{\partial\rho}{\partial x_i} - \rho\frac{\partial U_i}{\partial x_i}) - (\frac{3}{\theta} - \frac{m(v'^2 + j\omega'^2)}{2\theta^2})(v_i'\frac{\partial\theta}{\partial x_i} - \frac{\theta}{3}\frac{\partial U_q}{\partial x_q}) \\
+ (\frac{mv_i'}{\theta})(v_l'\frac{\partial U_i}{\partial x_l} - \frac{1}{\rho}\frac{\partial}{\partial x_i}(n\theta)) + (\frac{mj\omega_i'}{\theta})(v_l'\frac{\partial W_i}{\partial x_l})]
\end{aligned} \tag{2.50}$$

Here, the first order distribution is now expressed entirely in terms of the mean and perturbed flow properties. All that remains is to find the first order approximations to the equations 2.21, 2.22, 2.23, and 2.24 to obtain non-zero expressions for the missing terms in the first-order balance laws 2.17, 2.18, 2.19, and 2.20.

2.2.2 Stresses and Heat Flux

With the definition of the heat flux in equation 2.21, and the stresses in equations 2.22, 2.23, and 2.24, along with the definition of the average in equation 2.6, the zeroth and first-order approximations to the missing terms in the balance laws can be calculated. Beginning with

25

the zeroth order approximations, the averaging is carried out with f^0:[68]

$$q_\alpha^0 = \frac{m\rho}{2n} \int (v_l' v_l' v_\alpha' + j\omega_p'\omega_p' v_\alpha')(\frac{m\sqrt{j}}{2\pi\theta})^3 exp(-\frac{m(v_l'v_l' + j\omega_p'\omega_p')}{2\theta}) \, d^3v' d^3\omega'$$

$$= 0 \tag{2.51}$$

$$t_{\alpha\beta}^{Bol,0} = -\rho \int v_\alpha' v_\beta' (\frac{m\sqrt{j}}{2\pi\theta})^3 exp(-\frac{m(v_l'v_l' + j\omega_p'\omega_p')}{2\theta}) d^3v' d^3\omega'$$

$$= -n\theta\delta_{\alpha\beta} \tag{2.52}$$

$$t_{\alpha\beta}^{Cur,0} = -\rho\epsilon_{\beta pq} r_p \int \omega_q' v_\alpha' (\frac{m\sqrt{j}}{2\pi\theta})^3 exp(-\frac{m(v_l'v_l' + j\omega_p'\omega_p')}{2\theta}) d^3v' d^3\omega'$$

$$= 0 \tag{2.53}$$

$$m_{\alpha\beta}^0 = -\frac{3\rho j}{2} \int \omega_\beta' v_\alpha' (\frac{m\sqrt{j}}{2\pi\theta})^3 exp(-\frac{m(v_l'v_l' + j\omega_p'\omega_p')}{2\theta}) d^3v' d^3\omega'$$

$$= 0 \tag{2.54}$$

Due to the functional form of f^0, those integrals possessing odd powers of v_p' or ω_l' vanish. A key note is that the Boltzmann stress in equation 2.52 yields the hydrostatic pressure P from $n\theta$ due to the assumption that the fluid is an ideal gas. This result is expected as the zeroth-order Boltzmann stress should reflect the zeroth order pressure of an ideal gas at equilibrium.

For the first-order approximations to the above stresses, the definitions must now involve volume integrals of the first-order distribution function g:

$$q_\alpha^1 = \frac{m\rho}{2n} \int \int (v_l' v_l' v_\alpha' + \omega_p'\omega_p' v_\alpha') g d^3v' d^3\omega' \tag{2.55}$$

$$t_{\alpha\beta}^{Bol,1} = -\rho \int \int v_\alpha' v_\beta' g d^3v' d^3\omega' \tag{2.56}$$

$$t_{\alpha\beta}^{Cur,1} = -\rho \int \int \epsilon_{\beta pq} r_q \omega_p' v_\alpha' g d^3v' d^3\omega' \tag{2.57}$$

$$m_{\alpha\beta}^1 = -\frac{3\rho j}{2} \int \int \omega_\alpha' v_\beta' g d^3v' d^3\omega' \tag{2.58}$$

These volume integrals are more easily evaluated if they can be converted into surface inte-

grals. Since there is no angular dependence in these integrals, the spherical symmetry of the integrands implies:

$$\int \int G(v', \omega') d^3 v' d^3 \omega' = 16\pi^2 \int \int v'^2 \omega'^2 G(v', \omega') dv' d\omega' \tag{2.59}$$

Additionally, due to the functional form of f^0, terms involving the average of vector components of different indices, such as $\langle v'_\alpha v'_\beta \rangle$, retain non-zero values for the integral only when indices match. Therefore, the identities $\langle v'_\alpha v'_\beta \rangle = \delta_{\alpha\beta} \frac{\langle v'^2 \rangle}{3}$ and $\langle v'_\alpha v'_\beta v'_i v'_l \rangle = \frac{\langle v^4 \rangle}{15} (\delta_{\alpha\beta} \delta_{il} + \delta_{\alpha i} \delta_{\beta l} + \delta_{\alpha l} \delta_{\beta i})$ are employed for both the velocity and gyration variables. Applying all these properties to our volume integrals yields:

$$q_\alpha^1 = - \left[\frac{8\pi^2 m \rho \tau}{3} \int \int dv' d\omega' (v'^6 \omega'^2 + j v'^4 \omega'^4) [-\frac{4}{\theta} + \frac{m(v'^2 + j\omega'^2)}{2\theta^2}] \right.$$
$$\left. (\frac{m\sqrt{j}}{2\pi\theta})^3 exp(-\frac{m(v'^2 + j\omega'^2)}{2\theta}) \right] \frac{\partial \theta}{\partial x_\alpha} \tag{2.60}$$
$$= -(4n\tau\theta) \frac{\partial \theta}{\partial x_\alpha}$$

$$t_{\alpha\beta}^{\text{Bol},1} = \left[\frac{16\pi^2 \tau \rho}{15\theta} \int v'^6 \omega'^2 (\frac{m\sqrt{j}}{2\pi\theta})^3 exp(-\frac{m(v'^2 + j\omega'^2)}{2\theta}) d\omega' dv' \right] (\frac{\partial U_\alpha}{\partial x_\beta} + \frac{\partial U_\beta}{\partial x_\alpha} + \delta_{\alpha\beta} \frac{\partial U_l}{\partial x_l})$$
$$- \left[\frac{16\pi^2 \rho \tau}{3\theta} \int v'^4 \omega'^2 \frac{(v'^2 + j\omega'^2)}{6} (\frac{m\sqrt{j}}{2\pi\theta})^3 exp(-\frac{m(v'^2 + j\omega^2)}{2\theta}) dv' d\omega' \right] \delta_{\alpha\beta} \frac{\partial U_l}{\partial x_l}$$
$$= n\tau\theta (\frac{\partial U_\alpha}{\partial x_\beta} + \frac{\partial U_\beta}{\partial x_\alpha}) - \frac{n\tau\theta}{3} (\frac{\partial U_l}{\partial x_l} \delta_{\alpha\beta})$$

$$\tag{2.61}$$

$$t_{\alpha\beta}^{\text{Cur},1} = \left[\frac{16\pi^2 \rho \tau m j}{9\theta} (\frac{m\sqrt{j}}{2\pi\theta})^3 \int v'^4 \omega'^4 exp(-\frac{m(v'^2 + j\omega'^2)}{2\theta}) d\omega' dv' \right] \epsilon_{\beta pq} r_q \frac{\partial W_p}{\partial x_\alpha}$$
$$= (n\tau\theta) \epsilon_{\beta pq} r_q \frac{\partial W_p}{\partial x_\alpha} \tag{2.62}$$

$$m_{\alpha\beta}^1 = \left[\frac{48\pi^2 \tau \rho j^2 m}{2\theta} \int \omega'^2 v'^2 \omega'_\beta v_\alpha \omega'_l v'_p (\frac{m\sqrt{j}}{2\pi\theta})^3 exp(-\frac{m(v'^2 + j\omega'^2)}{2\theta}) d\omega' dv' \right] \frac{\partial W_l}{\partial x_p}$$
$$= (\frac{3n\tau j\theta}{2}) \frac{\partial W_\beta}{\partial x_\alpha} \tag{2.63}$$

The reduced forms of these stresses appear to follow familiar patterns. The heat flux in equation 2.60 appears to demonstrate a direct proportionality relationship with the tem-

27

perature gradient. The Boltzmann stress contains terms related to the familiar strain-rates and divergences of the velocity. Still, these stresses all have nonlinear dependence on the temperature, meaning that simplifications will have to be made before direct comparisons with classical fluids can occur.

2.3   Governing Equations

A direct substitution of the stresses found in equations 2.60, 2.61, 2.62, and 2.63 into the first-order balance laws 2.25, 2.26, 2.27, and 2.28 yields:

Continuity

$$\frac{\partial}{\partial t}\rho + \frac{\partial}{\partial x_l}(\rho U_l) = 0 \tag{2.64}$$

Linear Momentum

$$\frac{\partial}{\partial t}(\rho U_s) + \frac{\partial}{\partial x_l}(\rho U_l U_s) - \frac{\partial}{\partial x_l}[-P\delta_{sl} + n\tau\theta(\frac{\partial U_l}{\partial x_s} + \frac{\partial U_s}{\partial x_l}) - \frac{n\tau\theta}{3}\frac{\partial U_q}{\partial x_q}\delta_{sl}] - \tag{2.65}$$
$$\frac{\partial}{\partial x_l}(n\tau\theta\epsilon_{spq}r_q\frac{\partial W_p}{\partial x_l}) = 0$$

Angular Momentum

$$\frac{\partial}{\partial t}(\rho j W_s) + \frac{\partial}{\partial x_l}(\rho j W_s U_l) - \frac{\partial}{\partial x_l}[(n\tau j\theta)\frac{\partial W_s}{\partial x_l}] = 0 \tag{2.66}$$

Energy

$$\frac{\partial}{\partial t}(\rho e) + \frac{\partial}{\partial x_l}(\rho e U_l) - \frac{\partial}{\partial x_l}(4n\tau\theta\frac{\partial \theta}{\partial x_l}) - \rho\langle v_l\frac{\partial e}{\partial x_l}\rangle = 0 \tag{2.67}$$

These equations contain derivatives of nonlinear terms and products of spatially varying variables. For this first-order approximation to the balance laws, the products of gradients of terms are presumed to vanish. Furthermore, equation 2.66 contains a spatial derivative of the spatial coordinate r_p that has its origin at the center of mass of the spherical particle. Looking at Figure 2.1, the expression for this coordinate is easily derived in terms of the Eulerian coordinates: $r_i = x_i' - x_i$. Therefore:

$$\frac{\partial r_i}{\partial x_l} = -\delta_{il} \tag{2.68}$$

Clearly the derivative is zero unless the components of x and r are the same. Taking this derivative into account, removing terms associated with products of gradients, and allowing for the existence of body forces, the governing equations become:

Continuity

$$\frac{\partial}{\partial t}\rho + \frac{\partial}{\partial x_l}(\rho U_l) = 0 \tag{2.69}$$

Linear Momentum

$$\frac{\partial}{\partial t}(\rho U_s) + \frac{\partial}{\partial x_l}(\rho U_s U_l) + \frac{\partial P}{\partial x_s} - n\tau\theta\left(\frac{\partial^2 U_s}{\partial x_l \partial x_l} + \frac{2}{3}\frac{\partial^2 U_l}{\partial x_l x_s}\right) - \tag{2.70}$$
$$n\tau\theta\epsilon_{spq}\frac{\partial W_q}{\partial x_p} - \rho F_s = 0$$

Angular Momentum

$$\frac{\partial}{\partial t}(\rho j W_s) + \frac{\partial}{\partial x_l}(\rho j W_s U_l) - n\tau j\theta\frac{\partial^2 W_s}{\partial x_l \partial x_l} - \rho L_s = 0 \tag{2.71}$$

Energy

$$\frac{\partial}{\partial t}(\rho e) + \frac{\partial}{\partial x_l}(\rho e U_l) - (4n\tau\theta)\frac{\partial^2 \theta}{\partial x_l \partial x_l} - \rho\langle v_l\frac{\partial e}{\partial x_l}\rangle - \rho H = 0 \tag{2.72}$$

In the preceding equations the body forces ρF_s and ρL_s have been introduced to account for external phenomena unrelated to the stresses previously introduced. Body forces for the linear momentum are easily found from the classical approach and require no special treatment. In the independent angular momentum equation, however, the factors affecting ρL_s are more subtle. Figure 2.2 illustrates a body force created by the presence of vorticity near an individual particle. The connection between the two particles is symbolized by the coefficient κ. The motion of the right-hand particle creates the classical rotational motion, or macroscopic angular velocity, which induces the local rotation of the left particle. The amount of influence the angular velocity has on the gyration is determined by the value of κ. The body force disappears once the local rotation of the left particle equals the angular velocity, represented by half of the vorticity. De Groot and Mazur characterized this body force as an asymmetric pressure tensor,[54] which had a linear relationship with the difference
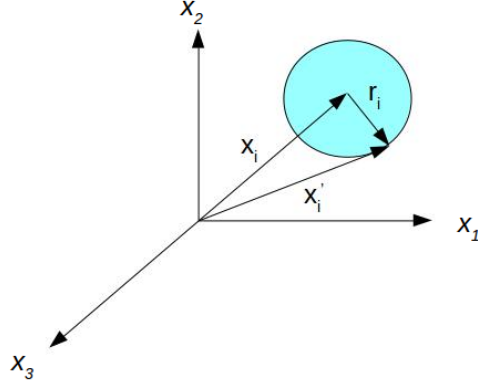
Figure 2.1: *Illustration of the relationship between coordinates r_i and x_i*

between the gyration and the angular velocity:

$$\rho L_s^{\text{interior}} = \nu_r (\epsilon_{spq} \frac{\partial U_q}{\partial x_p} - 2W_s) \tag{2.73}$$

Here, ν_r is designated as the "rotational viscosity," measuring the strength of induced gyration on a particle caused by the presence of a difference between its gyration and the local vorticity. This interior body force couples the local rotation with the translational velocity, ensuring that the linear momentum equation 2.70 and angular momentum equation 2.71 remain intertwined as long as the value of $\rho L_s^{\text{interior}}$ remains non-zero. The total angular momentum body force, ρL_s, can be viewed as the sum of this induced interior force and any external body moment force, $\rho L_s = \rho(L_s^{\text{interior}} + L_s^{\text{exterior}})$.

The continuity equation 2.69 is clearly the classical continuity equation for the mean velocity field. The deviation from classical kinetic theory becomes clear in the momenta equations. The compressible Navier-Stokes linear momentum equation, with the assumed satisfaction of Stokes's hypothesis, has the form:

$$\frac{\partial}{\partial t}(\rho U_s) + \frac{\partial}{\partial x_l}(\rho U_s U_l) + \frac{\partial P}{\partial x_s} - \mu \frac{\partial^2 U_s}{\partial x_l \partial x_l} - \frac{\mu}{3} \frac{\partial^2 U_l}{\partial x_l \partial x_s} - \rho F_s = 0 \tag{2.74}$$

Here, μ is the dynamic viscosity of the classical fluid. Comparing equations 2.74 and 2.70, the formulations are very similar, with the molecular viscosity from the Navier-Stokes equations represented by the expression $n\tau\theta$, as is expected from the first-order approximation to the
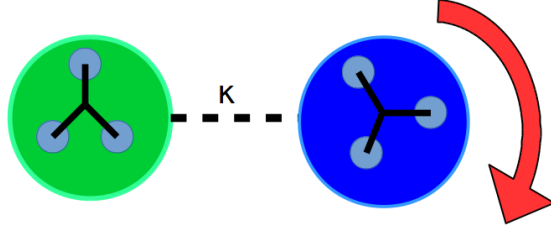
Figure 2.2: *Diagram of the angular momentum body force L_s. Presence of vorticity induces gyration of left structure, with the strength of the coupling effect determined by $2\nu_r$.*

Boltzmann transport equation.[22] The reduction of equations 2.69, 2.70, and 2.71 to the Navier-Stokes description will be discussed in more detail in the next section. The new term introduced by the preceding kinetic description has the form, $n\tau\theta\epsilon_{spq}\frac{\partial W_q}{\partial x_p}$. Here, the new variable of gyration, W_q, produces an additional source of linear momentum due to its transverse gradient. A notable insight is that the expression in front of the gyration gradient is also $n\tau\theta$, suggesting that the new term may contain a coefficient similar to the viscosity presented in classical fluids theory. To understand the meaning and importance of this new term in the linear momentum equation, the linear momentum equation from MCT is presented:[77]

$$\frac{\partial}{\partial t}(\rho U_s) + \frac{\partial}{\partial x_l}(\rho U_s U_l) + \frac{\partial P}{\partial x_s}$$
$$- (\lambda + \mu)\frac{\partial^2 U_l}{\partial x_l \partial x_s} - (\mu + \kappa)\frac{\partial^2 U_s}{\partial x_l \partial x_l} - \kappa\epsilon_{spq}\frac{\partial W_q}{\partial x_p} - \rho F_s = 0 \tag{2.75}$$

Here, λ represents the second coefficient of viscosity and a new coupling coefficient, κ, is added to the total viscosity of the MCT fluid. Additionally, this coupling coefficient corresponds to the coefficient described in Figure 2.2, as it determines the strength of the force induced by relative rotation within the MCT fluid. This theory, derived from the approach of rational continuum thermomechanics (RCT),[32;40;41;69] starts with the same picture of the fluid and derives governing equations from kinematic and thermodynamic principles for a fluid with spherical particles. Comparing equations 2.70 and 2.75, the term associated with the transverse gradient in the kinetic equation now has a counterpart term associated with

the coupling coefficient κ. Therefore, the first-order approximation to the Boltzmann-Curtiss transport equation produces a linear momentum equation consistent with the MCT formulation. Comparisons between the expressions for the coefficients in front of identical terms in these equations will shed light into the validity of these expressions for the new coefficients in MCT.

2.4 Physical Meaning of Relaxation Time

The simplification of the collisional term in equation 2.34 presumes that a singular relaxation time can be used to describe the transition from the real distribution function f to the equilibrium distribution function f^0. Due to the extra degrees of freedom introduced by the local rotation of the molecules, this relaxation time cannot be equated directly to the case of classical fluids. Still, as Chen et al demonstrated,[75] expressions for a singular relaxation time can incorporate multiple processes or models involving several degrees of freedom. These expressions typically start from a base time constant applied to the relaxation of the motions of the molecular motion. In the current treatment, this base relaxation time would apply to the gyration.

De Groot and Mazur investigated the case of viscous flow in an isotropic fluid, but allowed for asymmetry in the pressure tensor. This asymmetry required for the consideration of an independent conservation theorem for angular momentum. Furthermore, pressure asymmetry generated "internal angular momentum," S_p, which arose from the local angular velocity, ω_p, of groups of particles at a point in the system. From conservation of angular momentum, De Groot and Mazur derived a balance equation for the internal angular momentum:[54]

$$\rho \frac{dS_q}{dt} = -2\Pi_q \tag{2.76}$$

Here, Π_q is the asymmetrical component of the pressure tensor. Internal angular momentum could be easily related to the angular velocity through $S_q = I\omega_q$, where I denoted the average moment of inertia of the constituent particles. The asymmetric pressure tensor, however, needed a more nuanced treatment. By deriving relations for the conservation of

internal energy and entropy production, De Groot and Mazur found the thermodynamic force associated with the asymmetric pressure tensor.[54] This force emerged from a difference between the local and classical angular velocities, $\omega_s - \frac{1}{2}\epsilon_{spq}v_{q,p}$. Invoking Curie's principle[78] regarding thermodynamic fluxes and forces, De Groot and Mazur derived the following relation:[54]

$$\Pi_s = \nu_r(2\omega_s - \epsilon_{spq}\frac{\partial v_q}{\partial x_p}) \tag{2.77}$$

Clearly, the asymmetric pressure tensor mirrors the body force found in equation 2.73, indicating that the body force of the kinetic description can be obtained from a consideration of thermodynamic fluxes and forces. Given this closure relation, the conservation of internal angular momentum in equation 2.76 became:

$$\frac{d\omega_s}{dt} = -\frac{2\nu_r}{\rho I}(2\omega_s - \epsilon_{spq}\frac{\partial v_q}{\partial x_p}) \tag{2.78}$$

This equation is equivalent to the kinetic angular momentum equation 2.71 with the diffusion terms eliminated. Therefore, the kinetic theory is shown to obtain a more general form of a conservation equation. For the case of initially zero local angular velocity and constant vorticity, the solution to equation 2.78 becomes:

$$\omega_s = \frac{1}{2}\epsilon_{spq}\frac{\partial v_q}{\partial x_p}(1 - e^{-\frac{t}{\tau_o}}) \tag{2.79}$$

where the decay of the local angular velocity is characterized by a relaxation time constant, τ_o, that has the form:

$$\tau_o = \frac{\rho I}{4\nu_r} \tag{2.80}$$

Measurements of diatomic hydrogen and deuterium mixtures at $p = 1$ atm and $T = 77K$ by Montero et al give a value of $2.20 \times 10^{-8}s$ for the rotational relaxation time.[79] Thus, the assumptions of zero initial local rotation, constant vorticity, and absence of external forces, leads to the derivation of a characteristic relaxation time that exclusively applied to internal angular momentum. These assumptions become relevant when the characteristic

time is sufficiently reduced such that macroscale phenomena, such as the vorticity, can be approximated as constant compared with the evolution of local rotation. In these short time scales, equilibrium is achieved for the local rotation once it approaches the constant vorticity. Equation 2.80 provides a suitable first approximation of the characteristic relaxation time, τ, used in our kinetic theory description. De Groot's characterization of local angular velocity as the mean angular velocity of groups of particles matches the physical picture of our kinetic theory description. The addition of body forces into the governing kinetic theory equations can also incorporate the thermodynamic forces found in De Groot and Mazur's treatment. The rotational viscosity, ν_r, has a counterpart through the coupling coefficient κ in the MCT linear and angular momentum equations.[68] Therefore, numerical simulations of the kinetic and MCT descriptions should be able to determine the appropriate conditions for the use of equation 2.80 in this first order approximation.

2.5 Reduction to Navier-Stokes Equations

The introduction of local rotation, ω_s, as an independent variable has resulted in a slightly different physical picture from the classical fluids description shown in the Navier-Stokes equations. The angular momentum equation 2.71 is not derived from the linear momentum equation 2.70, while the classical vorticity equation can only be derived from the classical linear momentum equation previously shown in equation 2.74. Still, the physical picture from which equations 2.69, 2.70, 2.71, and 2.72 are derived differs from Boltzmann's classical picture of a monatomic gas only through the introduction of the variable of gyration. When the gyration of a particle is distinct from macroscopic rotation, as defined by the angular velocity, $\frac{1}{2}\epsilon_{sab}\frac{\partial U_b}{\partial x_a}$, the new form of the linear momentum equation 2.70 and the independent angular momentum equation 2.71 can provide an alternative description to the classical Navier-Stokes picture. When these two rotations are equivalent, the gyration provides no new insight from the classical description. Therefore, the governing equations derived in previous sections should reduce to the Navier-Stokes equations. Setting $W_s = \frac{1}{2}\epsilon_{sab}\frac{\partial U_b}{\partial x_a}$ in

the governing momentum equations 2.70 and 2.71 yields:

Reduced Linear Momentum

$$\frac{\partial}{\partial t}(\rho U_s) + \frac{\partial}{\partial x_l}(\rho U_s U_l) + \frac{\partial P}{\partial x_s} - n\tau\theta\left(\frac{\partial^2 U_s}{\partial x_l \partial x_l} + \frac{2}{3}\frac{\partial^2 U_l}{\partial x_l \partial x_s}\right) - \tag{2.81}$$
$$n\tau\theta\epsilon_{spq}\frac{\partial}{\partial x_p}\left(\frac{1}{2}\epsilon_{sab}\frac{\partial U_b}{\partial x_a}\right) - \rho F_s = 0$$

Reduced Angular Momentum

$$\tag{2.82}$$
$$\frac{\partial}{\partial t}\left(\rho\epsilon_{sab}\frac{\partial U_b}{\partial x_a}\right) + \frac{\partial}{\partial x_l}\left(\rho\epsilon_{sab}\frac{\partial U_b}{\partial x_a}U_l\right) - n\tau\theta\frac{\partial^2}{\partial x_l \partial x_l}\left(\epsilon_{sab}\frac{\partial U_b}{\partial x_a}\right) - 2\rho L_s^{\text{exterior}} = 0$$

The common terms of the microinertia j and $\frac{1}{2}$ have been eliminated from equation 2.82. A key observation from equation 2.82 is the absence of the interior body force, $\rho L_s^{\text{interior}}$, described in equation 2.73. The difference in rotational motions necessary for the inducement of gyration on a particle has vanished, thus making $\rho L_s^{\text{interior}} = 0$. Meanwhile, equation 2.82 matches the form of the vorticity equation, derived from the curl of the Navier-Stokes linear momentum equation 2.74:

$$\frac{\partial}{\partial t}\left(\rho\epsilon_{sab}\frac{\partial U_b}{\partial x_a}\right) + \frac{\partial}{\partial x_l}\left(\rho\epsilon_{sab}\frac{\partial U_b}{\partial x_a}U_l\right) - \mu\frac{\partial^2}{\partial x_l \partial x_l}\left(\epsilon_{sab}\frac{\partial U_b}{\partial x_a}\right) - \rho\epsilon_{sab}\frac{\partial F_b}{\partial x_a} = 0 \tag{2.83}$$

Looking at the reduced linear momentum equation 2.81, further manipulations will show how this equation matches the classical picture. Using the identity for the Levi-Civita tensor $\epsilon_{sab}\epsilon_{spq} = \delta_{ap}\delta_{bq} - \delta_{aq}\delta_{bp}$ and contracting the appropriate indices, equation 2.81 becomes:

$$\frac{\partial}{\partial t}(\rho U_s) + \frac{\partial}{\partial x_l}(\rho U_s U_l) + \frac{\partial P}{\partial x_s} - n\tau\theta\left(\frac{\partial^2 U_s}{\partial x_l \partial x_l} + \frac{2}{3}\frac{\partial^2 U_l}{\partial x_l \partial x_s}\right) -$$
$$\frac{n\tau\theta}{2}\left(\frac{\partial^2 U_p}{\partial x_s \partial x_p} - \frac{\partial^2 U_s}{\partial x_q \partial x_q}\right) - \rho F_s = 0 \tag{2.84}$$

Grouping together like terms yields the classical form of the Navier-Stokes linear momentum equation:

Type II N-S Equation

$$\frac{\partial}{\partial t}(\rho U_s) + \frac{\partial}{\partial x_l}(\rho U_s U_l) + \frac{\partial P}{\partial x_s} - \frac{n\tau\theta}{2}\frac{\partial^2 U_s}{\partial x_l \partial x_l} - \frac{7n\tau\theta}{6}\frac{\partial^2 U_p}{\partial x_s \partial x_p} - \rho F_s = 0 \tag{2.85}$$

The form of the classical momenta equations is achieved when local rotation is indistinguishable from macroscopic rotation. Still, the precise formulation found in equations 2.85 and 2.82 requires a more detailed treatment. The coefficient in front of the diffusion term for the original linear momentum equation 2.70 is equivalent to the classical expression $\mu = n\tau\theta$ derived by Huang.[22] In the reduced classical equation 2.85, the expression for the coefficient in front of the diffusion term is half that value, due to the contribution from the new term associated with the curl of the gyration. The temperature dependence of viscous rotational motion appears to have a slightly different limiting behavior as the particle rotation begins to resemble macroscopic motion.

2.5.1 The Classical Kinetic Equations

The previously discussed expression for the classical kinematic viscosity emerges from the same approach to the Boltzmann transport equation, with the equilibrium distribution function set as the Boltzmann distribution:

$$f^{Boltz}(x_i, v_i, t) = \frac{n}{(2\pi m\theta)^{3/2}} exp(-\frac{mv_l'v_l'}{2\theta}) \tag{2.86}$$

The distribution function has the same qualitative shape as the Boltzmann-Curtiss distribution in equation 2.5, but lacks terms that account for particle rotation. Additionally, the number density is obtained by integrating this function only over velocity space, changing the normalization function in front of the exponential.

Following the same logic as in section 2.2, a first-order approximation of the Boltzmann equation 2.2 using the Boltzmann distribution yields the classical kinetic equation:[22]

Type I N-S Equation

$$\frac{\partial}{\partial t}(\rho U_s) + \frac{\partial}{\partial x_l}(\rho U_s U_l) + \frac{\partial P}{\partial x_s} - n\tau\theta\frac{\partial^2 U_s}{\partial x_l \partial x_l} - \frac{n\tau\theta}{3}\frac{\partial^2 U_l}{\partial x_l x_s} - \rho F_s = 0 \tag{2.87}$$

The derivation of these equations allowed theorists to understand the physical basis behind coefficients in the Navier-Stokes equations, and to see how they vary with equilibrium parameters of the flow.[22] A quick comparison between the linear momentum equations 2.85

and 2.87 demonstrates how the choice of distribution function affects the final form of the governing equation, even when both equations maintain the classical Navier-Stokes form.

Figure 2.3 gives a visual demonstration for how the two kinetic approaches begin to diverge in obtaining the sets of equations that mimic their respective continuum theory counterparts. Equating the local rotation to the angular velocity introduces merges the terms in front of the Cauchy stress and viscous diffusion terms, yielding the Type II N-S equation 2.85. This form of the Navier-Stokes equation indicates that, while the local rotation's equivalence to macroscopic rotation may yield qualitative classic equations, the properties of the fluid still reflect the presence of local rotation through the new diffusion coefficient. A clear reduction in the temperature dependence of the viscous coefficient is observed while a clear increase in the coefficient of the compressive term is also apparent. These results may follow from the fact that local rotation is no longer playing a prominent role in determining the ultimate collisional dynamics of the flow. Viscous resistance, for instance, in these flows may be highly dependent on the locality of rotation. In any event, the contribution of the local rotation to the final form of the classical equations is evidently not eliminated when the particle rotation becomes equivalent to the vorticity.
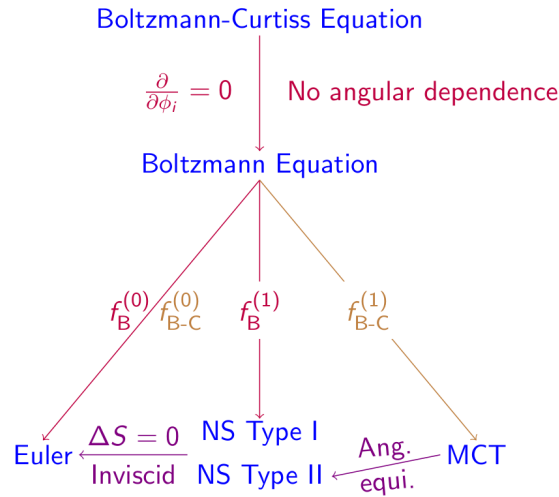
Figure 2.3: *A diagram illustrating how the kinetic approach leads to sets of governing equations that mirror the form of the classical and morphing continuum theory equations. An additional road to the form of the N-S equations exists via the Boltzmann-Curtiss distribution, when local rotation equals the angular velocity.*

2.6   Discussion

The first-order approximation to the Boltzmann-Curtiss transport equation was able to yield governing equations with terms corresponding to particular stresses in the Navier-Stokes equations and MCT. Furthermore, new material parameters, introduced by Chen in the zeroth-order approximation to fluids with spherical particles,[31] received expressions based on the relaxation time, number density, and equilibrium thermal energy. Resulting equations showed that the contribution of local rotation to the Cauchy stress and viscous diffusion were weighted equally in the kinetic description of the linear momentum equation. When transverse gradients in gyration disappear, the kinetic equation becomes the classical linear momentum equation, with the expression for the total viscosity equivalent to the result in classical fluids. It should be noticed that the current formulation is at the continuum level. The rotation here refers to the spin of the whole molecule and should not be confused with the rotation inside a molecule. The internal rotation and vibration modes are not within the scope and should be treated separately while these effects are dominant.

The approximations made to the solution of the Boltzmann-Curtiss transport equation should be understood before applying the obtained expressions to the appropriate terms within MCT. The collisional term on the right-hand side of equation 2.2 was approximated as a first-order difference scheme, where the return to equilbrium occurs after a period of time on the order of a singular time constant, τ. Therefore, the translational velocity and gyration motions must reach equilibrium within this period of time. As demonstrated in section 2.4, the neglection of diffusion and the assumption of constant vorticity leads to an approximation of the relaxation time for local rotation of groups of particles. If these groups of particles can be approximated as spheres, the preceding kinetic description still applies. The translational motion, then, should remain at a state of equilibrium, ensuring that the time constant denotes the rotational relaxation time. Absent these assumptions, the appropriate relaxation time for both degrees of freedom to equilibrate will need to be determined experimentally.

Once equilibrium parameters can be determined, preliminary expressions for the coeffi-

cients of various stresses can be determined. As mentioned in section 2.2, the coefficients for the diffusion and Cauchy stress terms contain the same expression, $n\tau\theta$. These expressions correspond to the material properties $\mu + \kappa$ and κ in equation 2.75, respectively. A direct comparison of the linear momentum equations suggests that the traditional kinematic viscosity, μ, does not have a counterpart in the kinetic theory description. This conclusion would be unfounded, as section 2.5 shows how the traditional form of the Navier-Stokes is also obtained from this description. Kinetic theory extrapolates the overall fluid behavior from a collection of individual particle motions, while MCT derives the balance laws from a continuum composed of inner structures. The coefficients from kinetic theory, found by characterizing and integrating over all the particles in the fluid, depend on the equilibrium conditions in the flow. The coefficients in MCT, meanwhile, are mathematical tools to relate stresses and strains at each point in the fluid. Because of these directions, one-to-one comparisons can easily be misleading. Therefore, the most accurate statement made in this derivation is that the first-order approximation to the Boltzmann-Curtiss equation does not yield a diffusion coefficient of a different magnitude when spherical rotation is added to classical flow. Meanwhile, the new Cauchy stress in MCT is produced in the kinetic description, and its coefficient has the same expression as the viscous diffusion. Qualitative comparisons can be made, but a direct quantative connection to coefficients within MCT is not warranted by this approach.

Chapter 3

MCT Simulation of Incompressible Flow

Predicting the conditions that lead a boundary layer to transition to turbulence is of great importance for the design of surfaces that can withstand the higher heating rates and drag forces associated with turbulent flows.[80] A consistent challenge in direct numerical simulations (DNS) of transitional flow has been efficiently capturing the physics of structures, particularly eddies or small vortices, within thin boundary layers.[13–17;81] Traditional solutions to this cost barrier have involved linearizing the N-S equations, averaging the velocity field, or creating a mathematical model for near-wall fluid behavior. Smith and Gamberoni[13] and Van Ingen[14] derived the e^N criterion, which focused on the growth rate N of the most unstable structures in a boundary layer. As he demonstrated the many applications and successes of his model, however, Van Ingen explains that the method must be recalibrated for each new experiment and for each different method of calculating the profile within the boundary layer.[82] Furthermore, Van Ingen's method superimposes the structures on the flow, leaving questions about the physical nature of individual disturbances unanswered. The computational costs of DNS and the limitations of the e^N criterion have lead the turbulence and transition (T2) community to make use of local mathematical models that rely on fundamental artifical parameters. For instance, Von Doenhoff and Braslow developed an

empirical relationship for Re_k, a Reynolds number associated with wall roughness elements of height k, and $\frac{d}{k}$, with d measuring the characteristic length of disturbances in the boundary layer.[83] Later models would focus on other physical factors such as the ratio of viscous stress to shear stress due to "streaks" in the boundary layer.[84] These streaks occur when vortices imposed on the boundary layer alternate the positions of high-speed and low-speed structures. Comparisons between these streak models and the models of Von Doenhoff and Braslow for rough-wall surfaces showed good agreement when ad-hoc closure relations were applied to velocity perturbations.[83–85] In every one of these models for the transition to turbulence within a boundary layer, local parameters, new mathematical parameters, or ad-hoc closure models were required to obtain a computationally efficient analysis that could produce any of the physics inside the boundary layer. This reliance on experiments motivated researchers to derive closure models based on the physical mechanisms driving a flow towards turbulence. Walters and Coljkat proposed a three-equation model that incorporated closure models for the RANS equations based on the transport of different types of fluctuations to different regimes of the flow.[86] Transport equations were added for turbulent kinetic energy, isotropic dissipation, as well as laminar kinetic energy. Source terms for these equations relied on assumptions about the factors that govern various terms. For instance, laminar kinetic energy was assumed to be governed by large-scale near-wall turbulent fluctuations. These physics-based closure models produced results consistent with experimental data and independent of the experimental setup. Still, Walters' reliance on physical assumptions to close the RANS equations highlights a key challenge to approaches that rely on averaging techniques. The heart of the problem lies in the characterization of near-wall fluid behavior. Each mathematical model described earlier assumes the fluid to be a continuum of non-oriented, infinitesmal points. As is well known, adapting a fine mesh to a continuum greatly increases the cost of computation for resolving motions at small scales in high Reynolds number flows. To avoid this cost, the fluids community developed averaging techniques to capture the essential mean flow. Any significant deviations from the mean flow were described as perturbations. In other words, the details of an individual structure were not the focus of the model. Microscale phenomena such as molecular rotation, eddy rotation, or

flow oscillation did not explicitly factor into the derivation of the governing equations. If any averaged equation wanted to describe the physics of eddy rotation, for instance, it had to do so via an external closure model. The challenge still remained of finding a multiscale description of the fluid that did not depend on the intuition of the researcher. In response to this challenge, Eringen derived a coherent analytical and physical description of the fluid as a series of finite mathematically defined structures. The governing equations of this new description, known as morphing continuum theory, now incorporated a new variable for the small-scale rotation of these structures.[17;70;87–89] For the case of turbulent boundary layers, Eringen's structures provide the dynamics of eddy translation and rotation at the scale of the width of the boundary layer. Eringen demonstrated analytically that all relevant parameters, such as Reynolds stress, for the classical turbulence formulation could be derived mathematically without the use of empirical or rheological closure models.[32] With specific boundary conditions, MCT has reliably produced numerical[17;70] and analytical[88–90] solutions equivalent to the Navier-Stokes solutions without the assistance of closure models in RANS or LES,[91] or the expensive computational resources in DNS. Still, the success of DNS simulations and the e^N method in predicting the transition to turbulence and producing physically realistic turbulent flows raises questions as to the added value of Eringen's theory to T2 research. Heinloo confirmed, however, that the physics of small eddy rotation was being neglected historically by the turbulence community, as it was assumed that the average angular velocity of these smaller eddies went to zero.[87] In addition, he suggested that the balance laws incorporating local rotation in the fluid could complement classical turbulence models such as $k - \omega$ and $k - \epsilon$. Key parameters such as turbulent shear viscosity μ_t and molecular dissipation ψ factored into more complex relationships to turbulent kinetic energy k. These relationships took into account the rotational anisotropic behavior of the structures. When rotational isotropy was assumed, the classical $k - \omega$ and $k - \epsilon$ equations emerged, indicating that the governing equations of MCT were perfectly compatible with previous successful descriptions of turbulence. Heinloo's conclusions illustrated not only the necessity of capturing small-scale rotation in the fluid, but also the mathematical rigor underpinning the new equations associated with local rotation in MCT.[87] Recent numerical simulations of

MCT indicate that turbulent flows can be reproduced without closure relationships when key material parameters are tuned properly.[70;92] Still, numerical implementations of Eringen's theory are not immune to the problems facing other numerical methods. Kirwan demonstrated that the choice of boundary conditions for the gyration at the wall has a significant impact on the overall velocity profile.[88] The main reason for this phenomenon involves the generation of disturbances, through the gyration, as structures pass by a solid wall. The nature of the interaction between the wall and passing structures affects the entire boundary layer flow profile. When the ratios of key microproperties reach critical values, Peddieson demonstrated that MCT can predict aspects of turbulence.[70] The choice of these properties is, however, key for generating transitional profiles. This paper will present the argument that MCT is fully capable of providing a theoretical and numerical basis for addressing boundary layer transitional and turbulent flows without the need for closure models. This success is attributed to the physics of the newly added structures, and their contribution to key stresses in the balance laws. Section 3.1 illustrates the physical picture of the fluid as envisioned by Eringen. The mathematical framework for this description of the fluid is also explained through the lens of rational continuum thermomechanics. Once the governing equations are obtained, the physical meaning of the new material parameters is inferred through nondimensionalizing the equations and obtaining key parameter ratios. Subsections in section 3.1 are provided for the discussion of appropriate boundary conditions for the new variables in MCT, and for the explanation of the finite volume method as it relates to MCT. In section 3.2, the problem of the transition into turbulence within a thin boundary layer will be explored numerically for $Re = 10^6$ over a flat plate. Computational results are compared with experimental data obtained from the European Research Community on Flow, Turbulence and Combustion (ERCOFTAC) database, showing good agreement for boundary layers of each flow regime. Finally, a brief discussion in section 3.3 is given on the future of MCT, including the potential to model compressible flows.

3.1 Morphing Continuum Theory

3.1.1 Theoretical Foundation

Classical fluid dynamics, based on the Navier-Stokes equations, treats the fluid as a continuum of structures. Though these structures contribute to the macroscopic behavior of the system, individual structures cannot drive the complete physics of the fluid singlehandedly. Furthermore, structures that are located near one another in classical fluid theory typically do not demonstrate large changes in motion or material characteristics. Changes in the fluid happen over groups of structures, and even local properties of the fluid apply to large groups of structures that behave in a similar manner. The characteristics of an individual structure are dependent primarily on the conditions of its neighboring structures. As the focus of fluids research turns to the small-scale or microscopic dynamics within the fluid, the individual properties of a structure receive a more nuanced treatment. Heinloo recounts the history of the discussion on the relationship between translational and rotational motion in turbulent fluids.[87] From the outset, he claims that the Richardson-Kolmogovorv or RK conception of turbulence required an independence of the "internal rotating degrees of freedom" from the translational motion of the bulk fluid.[87] In classical fluids, any rotational motion of the fluid is characterized by the vorticity, a property dependent on the average velocity field of the flow. For large enough eddies, the orientation of the motion of these eddies may be sufficiently characterized by the local vorticity. Heinloo notices, however, that if one described the angular motion of small-scale eddies through vorticity, eventually the mathematics would yield an average angular momentum of zero.[87] The eddies would possess no orientation.

Tracking the detailed motion of small-scale eddies, then, requires a departure from the assumptions of classical fluid dynamics. At the smallest scales, the structures must possess a finite size and an independent rotational motion. The first rigorous description of such a fluid came from Eringen.[32] His description involved a set of deformable, oriented structures that can rotate and change size indepedently from the translational motion of the fluid.

Mathematically, these new independent motions are characterized by a local vector ξ_k for its position with reference to the center of the structure and a director χ_{kK} that tracks the deformation of that structure. Figure 3.1 shows how these structures evolve in space and time. Morphing continuum theory models the evolution of the macromotion x_k along with the micromotion, as the different scales of fluid behavior continuously affect one another:

$$x_k = x_k(X_K, t) \quad X_K = X_K(x_k, t) \tag{3.1}$$

$$\xi_k = \chi_{kK}(X_K, t)E_K \quad E_K = \bar{\chi}_{Kk}\xi_k \tag{3.2}$$

$$K = 1, 2, 3 \quad k = 1, 2, 3 \tag{3.3}$$

Attaching the directors to the structure allows for the modeling of the rotation or deformation of the body of the structure as it undergoes translation. This more complex mathematical picture is useful for modeling the three-dimensional rotation and deformation of individual eddies within the turbulent region, as the structures serve as reliable models for the individual eddies. The observation that certain physical fluids demonstrated internal structure further led researchers to consider the fluid as a set of simple structures. Blood flows[32] and polymer melts[93] all contain individual structures that resist stretching or elongation, but still rotate. This local resistance to microdeformation is quantified by the microinertia, defined by the
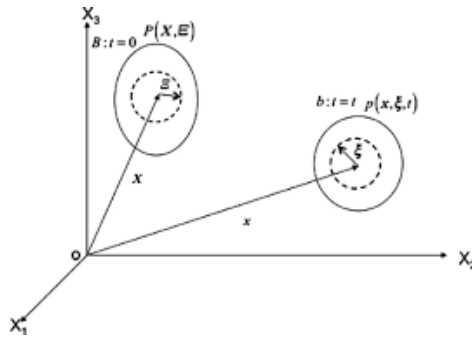
Figure 3.1: *Evolution of a structure with associated micromotion vector ξ and macromotion vector $\boldsymbol{x}$,*[17]

following expression:

$$j_{kl} \equiv i_{mm}\delta_{kl} - i_{kl} \tag{3.4}$$

Here, i_{kl} is an integrated quantity similar to the moment of inertia of the structure:

$$i_{kl} \equiv \frac{\int_{\delta v'} \rho'(\chi, \xi, t)\xi_k\xi_l dv'}{\int_{\delta v'} \rho'(\chi, \xi, t) dv'} \equiv < \xi_k\xi_l > \tag{3.5}$$

The tensor is obtained by integrating the characteristic microdeformations ξ_k over the mass of each structure $\rho'\delta v'$. Using the diagonal terms of this tensor, a single numerical value can be extracted by taking the average of the trace of the microinertia tensor:

$$j \equiv \frac{j_{mm}}{3} \tag{3.6}$$

For morphing continuum theory, the gyrations induced by rough surfaces or free-stream disturbances are the variables of interest in turbulent flow. When microisotropy is assumed, the degrees of freedom related to expansion or contraction of fluid structures vanish.[32] The resulting fluid differs from classical Navier-Stokes theory only through its local microrotation, characterized by the angular momentum $\rho j\vec{\omega}$. The equations reduce further when the structures in the fluid are approximated as spheres, leading to $j = \frac{2d^2}{5}$, where d is the diameter of the spheres.[17] Peddieson showed that these simple "micropolar fluids" predict characteristics of laminar flow and turbulence.[70] For this reason, we approximate our fluid as a microcontinuum of rigid spherical structures with constant material properties. As mentioned in the previous section, the main variables of interest for this research involve the translational motion v_k and local gyration ω_k, where k indicates the direction of motion. A more expansive approach would include temperature, heat transfer, and internal energy. For cases of extreme differences in temperature and pressure, these variables could not be neglected. The focus of this research is to observe the turbulent gyrations as they form and how they affect the flow within the boundary layer. Therefore, the only balance laws of interest involve linear and angular momentum. Following Eringen, we can state these laws

in the form:[32]

$$t_{lk,l} + \rho f_k = \rho \dot{v}_k \tag{3.7}$$

$$m_{lk,l} + e_{kij} t_{ij} + \rho l_k = \rho j \dot{\omega}_k \tag{3.8}$$

The equations include terms l_k and f_k that account for body forces in the fluid and now take into account the local angular momentum of the structures. For our flat plate simulations, the body forces will be neglected.

The key terms involve the Cauchy stress tensor t_{lk}, a stress tensor familiar to the Navier-Stokes equations, and the moment-stress tensor m_{lk}, a tensor that arises due to the transverse or perpendicular gradient of the gyration in the structures.[32] One can interpret this stress as a transfer of spinning energy through the distribution of structures from a compression or expansion of the fluid.[43;94] Any local difference in gyration produces macroscopic tension, but macroscopic tension also induces more gradients in gyration. Hence, the presence of structures adds a coupling effect, which is why the moment stress is sometimes called the couple stress. The added shear from the structures also leads to the Cauchy stress tensor becoming asymmetric, another departure from the N-S equations. To close the balance laws, Eringen derived new deformation-rate tensors a_{kl} and b_{kl} that included the added deformation of the structures:[32]

$$a_{kl} = v_{l,k} + \epsilon_{lkm} \omega_m \tag{3.9}$$

$$b_{kl} = \omega_{k,l} \tag{3.10}$$

Here, we make use of the permutation tensor ϵ_{lkm}. This independent deformation of the structures is also characterized by an additional material property κ related to the viscous resistance at the microscale. Thus, the viscous forces that dominate the swirling motion of eddies inside a turbulent boundary layer depend partially on the viscous resistance of the structures.

With the deformation-rate tensors, constitutive equations can be provided for the Cauchy and moment stress tensors:[17;32]

$$t_{kl} = -P\delta_{kl} + \lambda tr(a_{mn})\delta_{kl} + (\mu + \kappa)a_{kl} + \mu a_{lk} \tag{3.11}$$

$$m_{kl} = \frac{\alpha_T}{\theta}\epsilon_{klm}\theta_{,m} + \alpha tr(b_{mn})\delta_{kl} + \beta b_{kl} + \gamma b_{lk} \tag{3.12}$$

Note the appearance of the temperature gradient $\theta_{,m}$. The temperature gradient is relevant for energy considerations, but drops out of the angular momentum equation when equation 3.12 is substituted into equation 3.8, i.e. $\epsilon_{klm}\theta_{,ml} = 0$. Additionally, new material constants involve the second coefficient of viscosity λ, α and β. The latter two constants still require a coherent physical explanation, but only matter for three-dimensional flows. With these new formulations for the Cauchy and moment stress tensors, we can plug equations 3.11 and 3.12 into the balance laws, i.e. equations 3.7 and 3.8, obtaining:

$$\dot{\rho} + \rho v_{k,k} = 0 \tag{3.13}$$

$$-P_{,k} + (\lambda + \mu)v_{l,lk} + (\mu + \kappa)v_{k,ll} + \kappa(\epsilon_{klm}\omega_{l,m}) + \rho f_k = \rho\dot{v}_k \tag{3.14}$$

$$(\alpha + \beta)\omega_{l,lk} + \gamma\omega_{k,ll} + \kappa(\epsilon_{klm}v_{l,m} - 2\omega_k) + \rho l_k = \rho j\dot{\omega}_k \tag{3.15}$$

where ρ is density, v_k is the k-th component of the velocity vector, ω_k is the k-th component of the structure gyration, P is the pressure, μ refers to the first coefficient of viscosity, λ is the second coefficient of viscosity, ϵ_{klm} is the permutation tensor, κ is the structure viscosity coefficient, f_k refers to macroscopic body forces, γ is the structure diffusion coefficient, l_k refers to the body moment forces, j is the microinertia, and α and β are material constants. Equations 3.13, 3.14, and 3.15 constitute the three vector equations implemented into the fluid solver, with material properties inputted as parameters.

3.1.2 Finite Volume Method

In order to make use of the finite-volume code the equations must be written in the conservation form:

$$\frac{\partial \rho \phi}{\partial t} + \nabla \cdot (\vec{v}\phi) - \nabla \cdot (\Gamma_\phi \nabla \phi) = S_\phi \tag{3.16}$$

Here, ϕ refers to the conserved property of the flow. For our 2D problem, the continuity equation requires $\phi = 1$, linear momentum requires $\phi = v_x$ or v_y and angular momentum requires $\phi = j\omega_z$. For a 2D simulation in the x-y plane, any gyration vector must only have a z-component. If we integrate this equation over a volume V, we obtain:

$$\int_V \frac{\partial \rho \phi}{\partial t} dV + \int_V \nabla \cdot (\vec{v}\phi) dV$$
$$- \int_V \nabla \cdot (\Gamma_\phi \nabla \phi) dV = \int_V S_\phi dV \tag{3.17}$$

Here, dV refers to an infinitesmal three-dimensional volume. If we delineate A as the surface area surrounding volume V, dA as its infinitesmally small component, and $\hat{n}$ as the normal vector on the surface pointing outward away from the center of the volume, we can make use of Gauss's rule:

$$\int_V \frac{\partial \rho \phi}{\partial t} dV + \int_A (\phi \vec{v} \cdot \hat{n}) dA$$
$$- \int_A (\Gamma_\phi \nabla \phi \cdot \hat{n}) dA = \int_V S_\phi dV \tag{3.18}$$

In this format, discretization becomes much simpler. For a single cell of volume V_i surrounded by N_f faces, each with area A_f, we can rewrite equation 3.18 into discrete form:

$$\frac{\partial \rho \phi_i}{\partial t} V_i + \sum_f^{N_{faces}} \rho_f \tilde{v}_i \phi_i \bigg|_f \cdot \tilde{A}_f - \sum_f^{N_{faces}} \Gamma_{\phi_i} \nabla \phi_i \bigg|_f = S_{\phi i} V_i \tag{3.19}$$

When written in this format, our finite volume solver can now readily implement user-defined functions into ϕ and place them into equations of the form of equation 3.19, with various types of solvers available for marching forward in time. In this way, the governing equations, material properties, and relevant boundary conditions for MCT were numerically tested. For

our two-dimensional case, the conservative form of the governing equations are derived:[17]

$$\frac{\partial \mathbf{Q}}{\partial t} + \frac{\partial \mathbf{F}}{\partial x} + \frac{\partial \mathbf{G}}{\partial y} = \mathbf{S} \tag{3.20}$$

Taking together our balance laws from equations 3.13, 3.14, and 3.15, the vectors in equation 3.20 become:[17]

$$\mathbf{Q} = \begin{Bmatrix} \rho \\ \rho v_x \\ \rho v_y \\ \rho j \omega_z \end{Bmatrix} \tag{3.21}$$

$$\mathbf{F} = \mathbf{F}_{inv} - \mathbf{F}_{visc} \tag{3.22}$$

$$\mathbf{F}_{inv} = \begin{Bmatrix} \rho v_x \\ \rho v_x^2 + P \\ \rho v_x v_y \\ \rho j \omega_z v_x \end{Bmatrix} \tag{3.23}$$

$$\mathbf{F}_{visc} = \begin{Bmatrix} 0 \\ \lambda(\frac{\partial v_x}{\partial x} + \frac{\partial v_y}{\partial y}) + (2\mu + \kappa)\frac{\partial v_x}{\partial x} \\ \mu(\frac{\partial v_x}{\partial y} + \frac{\partial v_y}{\partial x}) + \kappa(\frac{\partial v_y}{\partial x} - \omega_z) \\ \gamma\frac{\partial \omega_z}{\partial z} \end{Bmatrix} \tag{3.24}$$

Angular momentum $\rho j \omega_z$ is implemented as a user-defined function and receives its own governing equation and boundary conditions. With our balance laws in conservative form, the relevant input variables and material properties can now be inputted into the fluid solver. The equations can be solved once appropriate boundary conditions are implemented. Note the additional property, γ, also known as the microdiffusivity, in the diffusion equation 3.24. This property determines to what extent gyrations and induced disturbances diffuse through the motion of the structures. The relative value of this property compared with the boundary

condition and the values of other microproperties will receive more treatment in later sections.

3.1.3 Relation to Navier-Stokes Equations

An important aspect of the governing equations is the fact that the Navier-Stokes equations can be recovered through legitimate mathematical arguments. If the rotational motion of the fluid is limited to the angular velocity of the macroscopic flow profile, we must scale our gyration term to half of the vorticity, i.e. $\omega_k = \frac{1}{2}\epsilon_{klm}v_{l,m}$. When this expression is substituted for ω_k, the equations for linear and angular momentum become:

$$-P_{,k} + (\lambda + \mu)v_{l,lk} + (\mu + \kappa)v_{k,ll} +$$
$$\kappa\epsilon_{klm}(\frac{1}{2}\epsilon_{lmk}v_{m,k})_{,m} + \rho f_k = \rho\dot{v}_k \tag{3.25}$$

$$(\alpha + \beta)(\frac{1}{2}\epsilon_{lmk}v_{m,k})_{,lk} + \gamma(\frac{1}{2}\epsilon_{klm}v_{l,m})_{,ll} + \rho l_k = \rho j\frac{1}{2}\epsilon_{klm}\dot{v}_{l,m} \tag{3.26}$$

The first term in equation 3.26 involves a divergence of a curl, so this term must vanish.

For equation 3.25, the following property of the permuation tensor is applied:

$$\epsilon_{klm} = \begin{cases} 0, & \text{if } k = l, k = m, \text{or } m = l \\ 1, & \text{if even} \\ -1, & \text{otherwise} \end{cases} \tag{3.27}$$

With these properties the equations reduce to a much simpler form:

$$-P_{,k} + (\lambda + \mu + \frac{1}{2}\kappa)v_{l,lk} + (\mu + \frac{1}{2}\kappa)v_{k,ll} + \rho f_k = \rho\dot{v}_k \tag{3.28}$$

$$\gamma(\frac{1}{2}\epsilon_{klm}v_{l,m})_{,ll} + \rho l_k = \rho j\frac{1}{2}\epsilon_{klm}\dot{v}_{l,m} \tag{3.29}$$

If we set $\mu^* = \mu + \frac{\kappa}{2}$, the linear momentum equation 3.28 reduces to the Navier-Stokes form:

$$-P_{,k} + (\mu^* + \lambda)v_{l,lk} + \mu^* v_{k,ll} + \rho f_k = \rho\dot{v}_k \tag{3.30}$$

Angular momentum in equation 3.29 now reduces to the familiar vorticity equation if we set $\frac{\gamma}{j} = \mu^*$.

$$\mu^*(\frac{1}{2}\epsilon_{klm}v_{l,m})_{,ll} + \frac{\rho l_k}{j} = \rho\frac{1}{2}\epsilon_{klm}\dot{v}_{l,m} \tag{3.31}$$

If we took the curl of 3.30 we would arrive at equation 3.31.

Thus, the linear and angular momentum equations for morphing continuum theory are shown to be an extension of the momentum equations in classical fluids. The limiting condition of the local rotation set to half of the vorticity ensured that the angular momentum as defined by MCT, $\rho j\omega$, would scale to the classical angular momentum, $\rho r\nu_{ang}$. Here, r refers to the distance from the point to the center of curvature and ν_{ang} is the macroscopic angular velocity equal to half of the vorticity, i.e. $\nu_{ang} = \frac{1}{2}|\nabla \times \vec{v}|$. For the Navier-Stokes equations the only way to recover this angular velocity is through the vorticity. Therefore, MCT is shown to be a mathematical extension of classical fluid dynamics.

3.1.4   Boundary Conditions and Material Parameters

From the development of morphing continuum theory, researchers discovered that the complexity of the physical picture, as illustrated by the balance laws and constitutive equations, left open questions regarding boundary conditions.[39;70;88] Kirwan and Newman declared the choice of values for gyration at the boundary to be arbitrary, with some minor restrictions they cited in order to have desirable velocity profiles near the boundary.[90] In their estimation, the fluid did not prefer any value for gyration at the boundary. In observing steady channel flows, Kirwan demonstrated that the null-stress condition at the wall leads to mathematical inconsistencies.[88] Assuming a velocity profile of $u = (u(y), 0, 0)$ and a gyration profile of $\omega = (0, 0, \omega(y))$, with the y-direction perpendicular to the plate, equations 3.14 and 3.15 reduce to the following:[88]

$$(\mu + \kappa)u^{''} + \kappa\omega^{'} = -P_{,x} \tag{3.32}$$

$$\gamma\omega^{''} - 2\kappa\omega - \kappa u^{'} = 0 \tag{3.33}$$

Integrating equation (3.32) in the y-direction yields:

$$(\mu + \kappa)u' + \kappa\omega = -P_{,x}y + C_1 \tag{3.34}$$

Constant C_1 emerges out of the indefinite integral. Setting the left-hand side of equation 3.34 to zero at the walls clearly leads to a mathematical inconsistency as C_1 is forced to take two different values. In other words, $C_1|_{y=\text{upper wall}} \neq C_1|_{y=\text{lower wall}}$. Therefore, Kirwan demonstrated that the boundary condition at the wall could not be arbitrary. In the case of Couette flow, at least, the shear stress could not be zero:

$$\kappa\omega_{wall} + (\mu + \kappa)u'_{wall} \neq 0 \tag{3.35}$$

Similar arguments showed that the condition $\omega_{wall} = \frac{u'}{2}$ produces the Navier-Stokes solution throughout the domain, and reveals no new physics from the velocity profile.[90] As mentioned in the previous subsection, the reason is that the gyration is equated to macroscopic angular momentum, restricting the gyrations at the wall to the ordinary rotation of a Navier-Stokes fluid.[39] From this discussion, the importance of modeling disturbances in the fluid near the wall becomes clear. If the bulk fluid experiences shear or moment stresses from the structures, these stresses will be amplified wherever velocity gradients are the largest. For flat plate boundary layer flows, this entails specifying the right condition for gyration at the plate. At the same time, morphing continuum theory must have the capacity to dissipate or diffuse away large disturbances, in order to capture the competing forces occuring in transitional flow. As Peddieson and Kirwan noted, this interplay involves the choice of the right combination of boundary conditions and material properties.[70;88] Implied in the shear stress condition 3.35 was a relationship between ω_{wall} and u'_{wall}. The inability to prescribe a null-stress condition lead several researchers to try a more general condition of the form:

$$\omega_{wall} + n(u'_{wall}) = 0 \tag{3.36}$$

For the general three-dimensional case, this boundary condition can be written in vector form:

$$\tilde{\omega}_{wall} = -n(\nabla \times \tilde{v}_{wall}) \qquad (3.37)$$

In deriving the specific solution to equations 3.32 and 3.33, Kirwan developed a soft constraint for n that preserved a negative velocity gradient at the upper boundary and a positive gradient for the lower boundary, conditions consistent with a no-slip boundary condition for the velocity:[88]

$$n < 1 + \frac{\mu}{\kappa} \qquad (3.38)$$

Thus, the value chosen for n affects not only the gyration but also the velocity profile, and the value of n is intricately tied to the material properties chosen for the flow. For parallel-plate flows, Kirwan demonstrated that a condition of $n > \frac{1}{2}$ amplified the velocity profile "relative to the N-S solution," thus pushing the flow towards turbulence.[88] In other words, the presence and nature of the structures, and their response to the boundary condition, leads to a macroscale amplification of the flow unseen in Navier-Stokes solutions. Meanwhile, $n < \frac{1}{2}$ served to reduce drag on the overall profile produced from near-wall velocity gradients. For the MCT flat plate simulations, laminar boundary conditions maintained a value of 0 for ω_{wall}, equivalent to a "no-spin condition" for structures near the wall. For both transitional and turbulent cases, the specific case of n = 1 for equation 3.37 was employed:

$$\tilde{\omega}_{wall} = -(\nabla \times \tilde{v}_{wall}) \qquad (3.39)$$

Therefore, the local gyration near the wall acts with equal magnitude to the large-scale vorticity. Since these disturbances must produce eddies that disrupt smooth gradients in the flow, the structures rotate in the opposite direction to the vorticity. This condition is also consistent with the concept of a rough wall, mentioned briefly in the introduction. Smooth static surfaces usually imply a no-slip condition, resulting in a smooth velocity gradient that preserves its vorticity everywhere near the wall. With sharp edges on the

wall, the direction of the vorticity and its strength are expected to vary unpredictably, generating turbulence near the wall. Finally, these disturbances near the wall must transfer their energy to other developing eddies throughout the boundary layer. The ability to transfer this energy, as is well known throughout the turbulence community, arises from the values of the fluid properties. From his dimensionalizing of the boundary-layer equations for flows of micropolar fluids over a flat plate, Peddieson arrived at three dimensionless parameters that served as parameters for his numerical simulations.[70] For our simulations, these dimensionless parameters have the form:

$$\alpha_1 = \frac{\kappa}{\mu}, \quad \alpha_2 = \frac{\kappa}{\rho\sqrt{j}\,U}, \quad \alpha_3 = \frac{\gamma}{\mu j} \tag{3.40}$$

The physical meaning of these ratios can be better understood by nondimensionalizing the linear momentum equation 3.14 and angular momentum equation 3.15. Defining our dimensionless variables:

$$
\begin{aligned}
t^* &= \frac{U_\infty t}{L} \\
u^* &= \frac{u}{U_\infty} \\
\omega^* &= \omega\frac{\delta}{U_\infty} \\
x^* &= \frac{x}{L} \\
y^* &= \frac{y}{\delta} \\
P^* &= \frac{P}{P_{out}}
\end{aligned}
\tag{3.41}
$$

Here, U_∞ refers to the inflow velocity, δ the thickness of the boundary layer, L the length of the plate, and P_{out} the outlet pressure. Note that we have scaled the gyration to the approximate value of the vorticity inside the boundary layer. Since the wall gyration in equation 3.36 is scaled to the vorticity for transitional and turbulent flow, this approximation will be valid at least in the vicinity of the wall. Substituting the expressions obtained for our original variables into the 2D form of the momentum equations yields:

$$(\frac{\rho U_\infty^2}{L})(\frac{\partial u^*}{\partial t^*} + \frac{\partial u^{*2}}{\partial x^*}) = -(\frac{P_{out}}{L})\frac{\partial P^*}{\partial x^*} + (\frac{\mu U_\infty}{L^2})\frac{\partial^2 u^*}{\partial x^{*2}} + (\frac{\mu U_\infty}{\delta^2})\frac{\partial^2 u^*}{\partial y^{*2}} + (\frac{\kappa U_\infty}{\delta^2})\frac{\partial \omega^*}{\partial y^*} \tag{3.42}$$

55

$$\left(\frac{\rho j U_\infty^2}{L\delta}\right)\left(\frac{\partial \omega^*}{\partial t^*} + \frac{\partial u^* \omega^*}{\partial x^*}\right) = \left(\frac{\gamma U_\infty}{\delta L^2}\right)\frac{\partial^2 \omega^*}{\partial x^{*2}} + \left(\frac{\gamma U_\infty}{\delta^3}\right)\frac{\partial^2 \omega^*}{\partial y^{*2}} - \left(\frac{\kappa U_\infty}{\delta}\right)\frac{\partial u^*}{\partial y^*} - \left(2\kappa \frac{U_\infty}{\delta}\right)\omega^* \quad (3.43)$$

Finally, we divide equation 3.42 by $\frac{\mu U_\infty}{\delta^2}$, and equation 3.43 by $\frac{\kappa U_\infty}{\delta}$:

$$\left(\frac{\rho U_\infty \delta}{\mu}\right)\left(\frac{\partial u^*}{\partial t^*} + \frac{\partial u^{*2}}{\partial x^*}\right) = \left(-\frac{P_{out}\delta^2}{\mu U_\infty L}\right)\frac{\partial P^*}{\partial x^*} + \left(\frac{\delta^2}{L^2}\right)\frac{\partial^2 u^*}{\partial x^{*2}} + \frac{\partial^2 u^*}{\partial y^{*2}} + \alpha_1 \frac{\partial \omega^*}{\partial y^*} \quad (3.44)$$

$$\left(\frac{1}{\alpha_2}\right)\left(\frac{\sqrt{j}}{L}\right)\left(\frac{\partial \omega^*}{\partial t^*} + \frac{\partial u^* \omega^*}{\partial x^*}\right) = \left(\frac{\gamma}{\kappa L^2}\right)\frac{\partial^2 \omega^*}{\partial x^{*2}} + \left(\frac{\gamma}{\kappa \delta^2}\right)\frac{\partial^2 \omega^*}{\partial y^{*2}} - \frac{\partial u^*}{\partial y^*} - 2\omega^* \quad (3.45)$$

From inspection, we have already obtained α_1 and α_2 from our now dimensionless equations. Deriving α_3 involves multiplying $\frac{\gamma}{\kappa\delta^2}$ by the ratio of the inertial parameters on the left-hand sides of equations 3.44 and 3.45:

$$\frac{\gamma}{\kappa\delta^2}\left(\frac{\frac{\rho U_\infty \delta^2}{\mu\, L}}{\frac{\rho j\, U_\infty}{\kappa L}}\right) = \frac{\gamma}{\mu\, j} \quad (3.46)$$

This final derivation shows that the parameters Peddieson used to gauge the onset of turbulence arise from the non-dimensional form of the governing MCT equations. Peddieson showed that these parameters emerged from a dimensionless form of the boundary-layer equations of micropolar fluid theory.[70] This derivation indicates that they are essential for the general theory as well. The physical significance of these parameters comes from the mathematical terms used to generate them. To generate α_1 we divided the couple stress related to the curl of ω, i.e. $\kappa(\nabla \times \vec{\omega})$, in equation 3.42 by the viscous diffusion of the velocity in the y-direction, i.e. $\mu\frac{\partial^2 u}{\partial y^2}$. Therefore, this term relates the tension in the fluid, experienced by and generated from the differing rotation of the structures, with the smoothing effect of the viscous diffusion within the boundary layer. An increase in its magnitude means a greater amount of energy is being transferred to gyration, a source of potential disturbances to laminar flow. Peddieson's definition of an eddy viscosity also showed a direct proportionality to α_1, indicating its contribution to the magnitude of the turbulent kinetic energy.[70] For α_2, the expression arose out of a ratio of the structures' contribution to the Cauchy stress, i.e. $\frac{\kappa U_\infty}{\delta}$ or $\kappa(\nabla \times \vec{u})$, over the inertial term $\frac{\rho j U_\infty^2}{L\delta}$, i.e. $\rho\frac{D\vec{\omega}}{Dt}$, in equation 3.43. From this expression, the parameter expresses the ratio of the viscous shear induced on the structures

over the inertial angular momentum the structures possess. The greater the shear, the more the structure's rotation is due to the effect of macroscopic shear rotating the structure and the greater the interaction of the structure with the bulk shear flow. If the inertial forces dominate, the rotation is due to its own inertial spin independent of macroscale behavior, and less interaction takes place at the microscale. The effect of this ratio on the transition to turbulence must be less pronounced, as the presence of large rotatonal motion from structures is all that is required to produce disturbances with the bulk flow. In order to produce disturbances, however, the structures must influence the regular shear flow or the flow profile will remain constant. Therefore, an increase in this parameter leads to a greater likelihood of transitional flow. Finally, the various forces involved in α_3 are investigated. The expression in equation 3.46 involves six different terms balancing each other. The $\frac{\gamma}{\kappa\delta^2}$ relates diffusion of the structures, i.e. $\gamma\nabla^2\vec{\omega}$, to the couple stresses. The fraction on the right is more complex. To summarize, inertial forces are balanced with viscous diffusion in the boundary layer for the velocity profile and with couple stresses for the gyration. The end result of this complex balance involves the ratio of macroscale diffusion through μ and microscale diffusion through γ, with $\frac{1}{j}$ used as a scaling factor. Upon reflection, this scaling factor is needed to assess how overall diffusion within the flow field is affecting an individual structure. At any rate, the value of this parameter is expected to be less vital to the development of turbulence. As mentioned in the discussion of α_1, turbulence involves large diffusion through the eddy viscosity. This coefficient is typically scaled with the macroscale viscosity μ, which tends to smooth out sharp gradients in the flow. The structure of these eddies must be maintained, so these gradients in the flow must also be maintained as well. For γ, its role is to smooth out gradients in the gyration. From the discussion of the couple stresses related to α_1, however, the presence of large changes in rotation is precisely how structures react to and contribute to disturbances in the flow. Evidently, this parameter follows a similar trend to α_2 in that it determines the extent to which a structure diffuses due to the velocity or due to gyration. Therefore, we expect α_1 to be the dominant parameter in determining whether a flow reaches a transitional state and eventually becomes turbulent.

3.2   Uniform Flow over a Flat Plate

Flow past a zero pressure gradient flat plate with $Re_L = \frac{\rho U L}{\mu + \kappa}$ of 10^6, where L is the length of the plate, is studied. The full comparison of the results obtained with the numerical simulation and the experimental results from ERCOFTAC are displayed in Figure 3.2. The figures display normalized velocities compared with normalized y-coordinates at $x = 0.5$ for the transitional case and $x = 0.75$ for turbulent flow in the domain. The turbulent boundary layer did not produce the same profile for every slice along the domain, indicating that parts of the domain were still transitioning to turbulence. This is also the reason the results from ERCOFTAC are taken from various slices along the flat plate. From the numerical parameters in Table 3.1, as well as the values Peddieson obtains,[70] it is apparent that α_1 increases by a factor of four from the transition profile to the turbulent profile. Meanwhile, the values of α_2 and α_3 remain almost constant, with a slightly noticeable decrease in α_3. This result is consistent with the discussion of the physical significance of Peddieson's parameters in Section 3.1. Couple stresses do overpower viscous diffusion, as demonstrated by the rise of α_1, while the precise cause of the gyration or diffusion of the structures, captured by parameters α_2 and α_3, does not remain relevant for the production of turbulence. For transitional flow, the profile shows good agreement throughout the domain as shown in Figure 3.2. The turbulent flow shows a slight deviation from the results as the profile gets closer to the free-stream. It is possible that the free-stream motion smoothed out disturbances occurring near the top of the boundary layer, thus producing a less turbulent profile. Experiments done with a larger set of experimental datasets and over a larger scale of Reynolds numbers could confirm if this phenomenon leads to consistent deviations near the free-stream layer. In all cases, however, near-wall behavior lines on top of experimental data, indicating that the sharper gradients in the velocity profile are resolved.
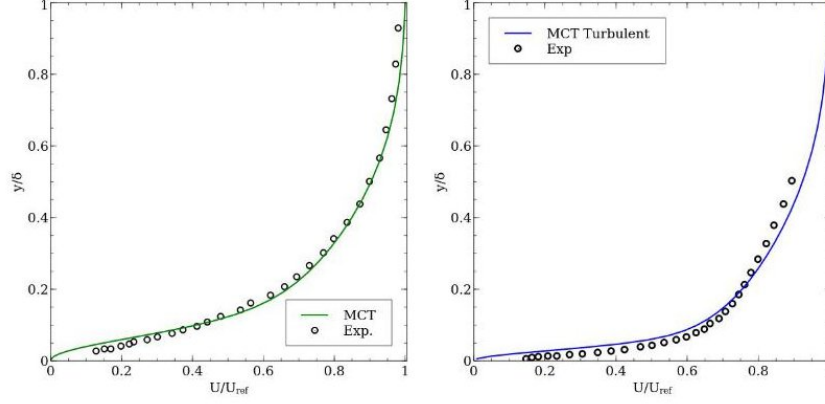
Figure 3.2: *Uniform flow $U = 5 \frac{m}{s}$ over a 2 meter flat plate, Plots of $\frac{y}{\delta}$ vs. $\frac{u}{U}$, Data obtained at $x = 0.5$ for the transitional case and $x = 0.75$ for turbulent case, Boundary Layer thickness δ obtained from point where $u = 0.99U$, Numerical simulations show good agreement with experimental data for all cases.*[95]

Parameter	Transitional	Turbulent
κ	9.6×10^{-6}	9.9×10^{-6}
γ	2.2×10^{-13}	4.7×10^{-14}
α_1	24	99
α_2	0.00135	0.0014
α_3	0.275	0.235

Table 3.1: *Material properties used as parameters for transitional, and turbulent cases, α_n parameters meant to continue parametric analysis, started by Peddieson, of influence of microproperties in transition and turbulence regimes.*[70]

3.3 Discussion

The preceding simulation and comparison with experimental data served two key purposes for this work. The successful reproduction of the experimental data related to the transition to turbulence as well as full turbulence indicates that morphing continuum theory serves as a useful tool for efficient generation of physically reliable boundary layer profiles for transitional and turbulent flows. As mentioned in chapter 1, the main goal for MCT was to bypass the high costs of DNS, while still maintaining integrity in the physics of the flow. The physics of the smaller eddies is recovered by MCT as the balance laws and constitutive relations depend on the motion and gyration of the structures.

The second key goal was to test the contribution and importance of new material pa-

rameters within MCT. New material properties related to the structures, particularly κ, are shown to drive the evolution of the boundary layer when disturbances are introduced at the wall. The dominance of the parameter α_1 indicates that the key stresses affecting the fluid, particularly the couple stresses, happen at the microscale. In order to maintain disturbances in such a thin layer, the structures must transfer energy to each other to create sharp gradients in their rotation. The relatively tiny magnitudes of α_2 and α_3, as well as their constancy between the simulations, indicate that α_1 must drive the simulation. Still, we require the former two parameters to have non-zero values, or the shear flow's interaction with a structure is not fully described. Microscale diffusion, as indicated by the choice of γ, is almost negligible.

The predominance of κ over μ in its influence over the dynamics of the boundary layer is relevant to the discussion of how the kinetic derivation in the previous chapter relates to the MCT governing equations. From a first-glance comparison, it appeared that μ did not contribute to the total viscous diffusion coefficient when both the Cauchy stress and viscous diffusion terms were present. In this simulation, the transitional and turbulent boundary-layer profiles emerged only when the value of κ exceeded μ by an order of magnitude. These more complex flows are the precise kinds of flows that distinguish MCT and the kinetic description from their classical counterparts, due to the contribution of individual structures. When the Cauchy stress term becomes more prominent, the expectation is that its coefficient will approach the value of the total viscous diffusion coefficient and this incompressible simulation demonstrates this phenomenon.

Chapter 4

MCT Simulations of Compressible Turbulence

4.1 Supersonic Flow Past a Cylinder

The interaction of a turbulent flow with a shock continues to pose several challenges to the fluid dynamics community. The interaction is of practical concern for the mutual interaction of a shock and a turbulent boundary layer. For high-speed engineering flows, turbulent boundary layers can be distorted and the boundary layer separated as a result of the interaction.[96] From experimental and theoretical analyses, a consensus has emerged that Reynolds shear stress and turbulence intensity are amplified across the shock wave.[97] In the case of a more complex geometry such as a compression corner, factors such as shock movement and boundary layer curvature also become relevant.[97] Though conventional models have been able to track the mean properties in the region where the boundary layer interacts with the shock, Humble notes that these models are still unable to give complete predictions of the properties of turbulence as it interacts with the shock.[96] This difficulty speaks to a much broader problem in analytical turbulent models of resolving rapid changes in fluid properties at small relevant length scales. Shock-turbulent boundary layer interactions amplify the need to resolve small regions of interest.

A complete physical description of turbulent interactions with an oncoming shock has been the subject of numerical and theoretical study for decades.[97–101] Turbulent flows and turbulent boundary layers continuously undergo a process of energy cascading, where large eddies transfer kinetic energy to small eddies that in turn dissipate this energy as heat. When turbulence encounters a shock, this smooth process is interrupted. Large vortices are deformed, producing more anisotropy in the flow. The distribution of eddy energy and size changes instantaneously. Compression of the flow leads to an amplification of turbulent kinetic energy and a general increase in turbulence length scales. To make these general conclusions, researchers construct turbulent kinetic energy spectra before and after turbulence interacts with a shock. The challenge for the turbulence community is to develop an efficient method of recording these spectra, while still capturing all the relevant length scales and structures of turbulent flows and boundary layers. The cost of producing high-speed flows in the laboratory, and the difficulty of measuring flows near the vicinity of the shock or inside the boundary layer, require for the development of reliable multi-scale compressible numerical solvers. As with general turbulence, traditional numerical solvers have limitations in capturing the full range of physics underlying shock-turbulence interactions. Lee noted that Direct Numerical Simulation could not account for the physical effects of the "sub-grid" length scales on the larger resolved eddies.[97] In other words, the choice of mesh resolution for DNS limits the range of eddies one can resolve, and therefore the scope of turbulent kinetic energy (TKE) spectra. Therefore, numerical techniques such as Large-Eddy Simulation combined with sub-grid models, shock-capturing schemes, and shock-fitting methods have been employed to resolve shock and turbulence length scales unresolved by DNS.[97;97;101;102] Through one or a combination of these alternatives to DNS, much progress has been made in approximating energy transfer after the shock for smaller eddies and thinner shocks. Still, the assumptions built into these numerical methods ensure that artificial issues, such as numerical dissipation or oscillation, will prevent a comprehensive description of the physical picture. Ducros created a Large-Eddy Simulation method that incorporated numerical dissipation to resolve the discontinuity at the shock while minimizing dissipation away from the shock to preserve the incoming disturbances in the flow.[100] Still, the method was restricted

for weakly compressible flows, high Reynolds numbers and low turbulent Mach numbers. Andreopoulos notes that the physics of shock-turbulence interactions depends, among many factors, on the level of compressibility in the flow and the strength of the incoming turbulence.[103] Relying on numerical schemes that work only for limited ranges of parameters limits the type of interactions one can observe from these solvers. Recently, Ryu has been using linear analysis to analytically describe turbulent structures behind the shock, where the Navier-Stokes equations have been known to break down for large Mach numbers and strong shocks, and demonstrate that DNS solutions converge to the linear analysis solutions behind the shock.[104] This attempt to bring back old analytic methods illustrates how much work remains to develop a compressible turbulence solver that can produce a physical TKE spectrum on both sides of a shock front.[98;99] In order to produce these spectra, the numerical method must rely on a theory that can accurately model the smallest eddies in close proximity to the shock. Additionally, the theory must not rely on mesh refinement to model these eddies, or it poses the same challenges as DNS creates. Such a theory already exists, and has been shown to be a reliable tool of reproducing turbulence. Eringen developed a mathematically rigorous theory that allowed for a greater insight to the microstructure of fluids.[32] In a departure from classical fluid theory, these "micropolar" fluids were composed of finite structures that possessed orientation. The analysis of the fluid had to account for the motion and deformation of these elastic structures. For turbulent flows, these structures describe the motion of individual eddies. When the governing equations were implemented into incompressible flow solvers, turbulent velocity profiles were reliably generated inside thin boundary layers.[105] Thus, the analytical and numerical descriptions of the fluid now incorporated terms directly related to the physics at the length scale of the smallest eddies. Recently, micropolar fluids have been implemented into solvers to model unsteady compressible flows to model the effect of microstructures on the lift and drag of a cylinder.[25] The intent of this paper is to demonstrate the relevance of Morphing Continuum Theory, a special case of Eringen's theory, to the problem of turbulent interactions with a shock front. Subsection 4.1.1 reiterates the theoretical background for MCT, but introduces the additional components associated with compressible flow, and particularly the energy equation. In subsection 4.1.2,

a brief description of the numerical implementation of compressible MCT is presented, with relevant initial and boundary conditions shown. Numerical results are presented in subsection 4.1.3 for free-stream turbulence passing a bow shock around a cylinder. Energy spectra for the turbulent kinetic energy and translational kinetic energy are shown, leading to a discussion of energy cascade within the flow. Final reflections on the contributions of MCT to the field of compressible turbulent flows are presented in subsection 4.1.4.

4.1.1   MCT Compressible Flow Equations

As discussed earlier, Morphing Continuum Theory uses spherical particles as the fundamental components of the fluid. These spheres still contain their own microinertia, with the characteristic length scale being the diameter d of the sphere. Chen showed that a fluid of spherical particles leads to the relation $j = \frac{2}{5}d^2$.[17] Therefore, j is a parameter available for controlling the size of eddies one wishes to describe. In addition, it is related to the rotational energy each of these eddies carries. If we describe the gyrational motion of an eddy as ω_k with k being the direction of motion, then we can define the angular velocity of the structure as $\sqrt{j}\omega_k$. The total velocity of the fluid can now be written as $v_{total} = v + \sqrt{j}\omega$, where v is the translational velocity of the structure. If the magnitude of the angular rotation is small compared to the translational motion, the motion is mathematically equivalent to the perturbed velocity found in the Reynolds-Averaged Navier Stokes equations. With a new definition for the total velocity, the definiton of the deformation rate of the fluid must be reconstituted:[32]

$$a_{kl} = v_{l,k} + \epsilon_{lkm}\omega_m \tag{4.1}$$

$$b_{kl} = \omega_{k,l} \tag{4.2}$$

The a_{kl} tensor indicates how the rotation of the particles contributes to the familiar strain-rate produced only by transverse velocity gradients in the Navier-Stokes equations. The b_{kl} tensor indicates that an entirely new strain is experienced from simple gradients in the

gyration. The physical meaning of this strain will become evident when stress tensors are expressed in terms of the deformation tensors.

In addition to the connection to the perturbed velocity, MCT provides the means of calculating the turbulent kinetic energy. Given a fluid density ρ, the rotational energy then becomes $\frac{1}{2}\rho(\sqrt{j}\omega_k)^2$ or $\frac{1}{2}\rho j\omega_k^2$. In fact, this term has been shown to be mathematically equivalent to the turbulent kinetic energy when the governing equations for momentum and energy are derived for MCT.[17] In the simulations of turbulence before and after a shock, this term will carry the information about eddy energy transfer. The governing equations for MCT are derived from balance laws for mass, linear momentum, angular momentum, and energy. In tensor form, the balance laws are written as:

$$\frac{\partial \rho}{\partial t} + (\rho v_i)_{,i} = 0 \tag{4.3}$$

$$t_{lk,l} + \rho f_k = \rho \dot{v}_k \tag{4.4}$$

$$m_{lk,l} + \epsilon_{kij} t_{ij} + \rho l_k = \rho j \dot{\omega}_k \tag{4.5}$$

$$\rho \dot{e} - t_{kl} a_{kl} - m_{kl} b_{lk} + q_{k,k} - \rho h = 0 \tag{4.6}$$

Here, l_k is the body moment density, t_{kl} the Cauchy stress tensor, f_k the body force density, m_{kl} the moment stress tensor, e the internal energy density, and q_k the heat flux.

These laws are derived directly from thermodynamics and apply to any microcontinuum, the term used for any space composed of particles.[32,40,41,106] To obtain the governing equations for MCT, constitutive equations are used to relate the Cauchy and moment stresses and the heat flux to the various velocities in the flow. These linear constitutive equations are derived to be:[17,32]

$$t_{kl} = -P\delta_{kl} + \lambda tr(a_{mn})\delta_{kl} + (\mu + \kappa)a_{kl} + \mu a_{lk} \tag{4.7}$$

$$m_{kl} = \frac{\alpha}{\theta}\epsilon_{klm}\theta_{,m} + \alpha tr(b_{mn})\delta_{kl} + \beta b_{kl} + \gamma b_{lk} \tag{4.8}$$

$$q_k = \frac{K}{\theta}\theta_{,k} + \alpha\epsilon_{klm}\omega_{m,l} \tag{4.9}$$

Here P is the pressure, μ the first coefficient of viscosity, λ the second coefficient of viscosity, ϵ_{klm} is the permutation tensor, κ the microstructure viscosity coefficient, γ the microdiffusivity, α and β material constants, $\theta_{,m}$ the temperatrue gradient, K the thermal conductivity, and a_{kl} and b_{kl} the deformation-rate tensors shown earlier. Finally, when the expressions for deformation-rate tensors and stress tensors are plugged into the balance laws, the governing equations have the form:

$$\dot{\rho} + \rho v_{k,k} = 0 \tag{4.10}$$

$$-P_{,k} + (\lambda + \mu)v_{l,lk} + (\mu + \kappa)v_{k,ll} + \kappa(\epsilon_{klm}\omega_{l,m}) + \rho f_k = \rho \dot{v}_k \tag{4.11}$$

$$(\alpha + \beta)\omega_{l,lk} + \gamma\omega_{k,ll} + \kappa(\epsilon_{klm}v_{l,m} - 2\omega_k) + \rho l_k = \rho j \dot{\omega}_k \tag{4.12}$$

$$(t_{kl}v_l)_{,k} + (m_{kl}\omega_l)_{,k} - q_{k,k} + \rho h + \rho f_l v_l + \rho l_i \omega_l = \rho \dot{E} \tag{4.13}$$

where $E = e + \frac{1}{2}(v_l v_l + j\omega_l\omega_l)$ is the total energy of the fluid.

To close this system of equations, we need to relate the pressure and density with the specific energy e. For this case, the fluid is presumed to be an ideal gas, leading to the relations:

$$e = c_v\theta = c_v \frac{p}{\rho(c_p - c_v)} \tag{4.14}$$

$$\rho E = \frac{p}{(\frac{c_p}{c_v} - 1)} + \frac{1}{2}\rho(v_l v_l + j\omega_l\omega_l) \tag{4.15}$$

Here, c_p and c_v refer to the specific heat of the fluid at constant pressure and volume respectively. The ratio $\frac{c_p}{c_v}$ was set to the value for air, 1.4. These equations establish the basis of our theory but will be modified to serve the finite volume solver, discussed in the next section.

4.1.2 Numerical Implementation

Finite Volume Method

The finite volume solver requires governing equations of the form:

$$\frac{\partial \rho \phi}{\partial t} + \nabla \cdot (\vec{v}\phi) - \nabla \cdot (\Gamma_\phi \nabla \phi) = S_\phi \qquad (4.16)$$

Here, ϕ refers to the conserved property of the flow. For the 2D problem, the continuity equation requires $\phi = 1$, linear momentum requires $\phi = v_x$ or v_y, angular momentum requires $\phi = j\omega_z$, and energy requires $\phi = E$. The density in equation 4.16 is obtained at each time step from the ideal gas law.

Integrating equation 4.16 over a volume V yields:

$$\int_V \frac{\partial \rho \phi}{\partial t} dV + \int_V \nabla \cdot (\vec{v}\phi) dV - \int_V \nabla \cdot (\Gamma_\phi \nabla \phi) dV = \int_V S_\phi dV \qquad (4.17)$$

Here, dV refers to an infinitesmal volume. If we delineate A as the surface area surrounding volume V, dA as its infinitesmally small component, and $\hat{n}$ as the normal vector on the surface pointing outward away from the center of the volume, equation 4.17 can be rewritten as:

$$\int_V \frac{\partial \rho \phi}{\partial t} dV + \int_A (\phi \vec{v} \cdot \hat{n}) dA - \int_A (\Gamma_\phi \nabla \phi \cdot \hat{n}) dA = \int_V S_\phi dV \qquad (4.18)$$

For a single cell of volume V_i surrounded by N_f faces, each of area A_f, equation 4.18 becomes:

$$\frac{\partial \rho \phi_i}{\partial t} V_i + \sum_f^{N_{faces}} \rho_f \tilde{v}_i \phi_i \bigg|_f \cdot \tilde{A}_f - \sum_f^{N_{faces}} \Gamma_{\phi_i} \nabla \phi_i \bigg|_f = S_{\phi i} V_i \qquad (4.19)$$

The finite volume solver can now implement user-defined functions into ϕ and solve them in equations of the form of 4.19. In this way, the governing equations, material properties, and boundary conditions for MCT were numerically implemented.

For the two-dimensional compressible case, the conservative form of the governing equations have been modified to be in conservative form.[17] A conservative differential equation

is defined as:

$$\frac{\partial \mathbf{Q}}{\partial t} + \frac{\partial \mathbf{F}}{\partial x} + \frac{\partial \mathbf{G}}{\partial y} = \mathbf{S} \tag{4.20}$$

Taking together our governing equations 4.10, 4.11, 4.12 and 4.13, the vectors in 4.16 can be shown to be:

$$\mathbf{Q} = \left\{ \begin{array}{c} \rho \\ \rho v_x \\ \rho v_y \\ \rho j \omega_z \\ \rho E \end{array} \right\} \tag{4.21}$$

$$\mathbf{F} = \mathbf{F}_{inv} - \mathbf{F}_{visc} \tag{4.22}$$

$$\mathbf{F}_{inv} = \left\{ \begin{array}{c} \rho v_x \\ \rho v_x^2 + P \\ \rho v_x v_y \\ \rho j \omega_z v_x \\ (\rho E + P) v_x \end{array} \right\} \tag{4.23}$$

$$\mathbf{F}_{visc} = \left\{ \begin{array}{c} 0 \\ \lambda(\frac{\partial v_x}{\partial x} + \frac{\partial v_y}{\partial y}) + (2\mu + \kappa)\frac{\partial v_x}{\partial x} \\ \mu(\frac{\partial v_x}{\partial y} + \frac{\partial v_y}{\partial x}) + \kappa(\frac{\partial v_y}{\partial x} - \omega_z) \\ \gamma\frac{\partial \omega_z}{\partial x} \\ F_{visc[2]} v_x + F_{visc[3]} v_y + F_{visc[4]} \omega_z - q_x \end{array} \right\} \tag{4.24}$$

$$\mathbf{G} = \mathbf{G}_{inv} - \mathbf{G}_{visc} \tag{4.25}$$

68

$$\mathbf{G}_{inv} = \begin{Bmatrix} \rho v_y \\ \rho v_x v_y \\ \rho v_y^2 + P \\ \rho j \omega_z v_y \\ (\rho E + P) v_y \end{Bmatrix} \qquad (4.26)$$

$$\mathbf{G}_{visc} = \begin{Bmatrix} 0 \\ \mu(\frac{\partial v_x}{\partial y} + \frac{\partial v_y}{\partial x}) + \kappa(\frac{\partial v_x}{\partial y} + \omega_z) \\ \lambda(\frac{\partial v_x}{\partial x} + \frac{\partial v_y}{\partial y}) + (2\mu + \kappa)(\frac{\partial v_x}{\partial y}) \\ \gamma \frac{\partial \omega_z}{\partial y} \\ G_{visc[2]} v_x + G_{visc[3]} v_y + G_{visc[4]} \omega_z - q_y \end{Bmatrix} \qquad (4.27)$$

$$\mathbf{S} = \begin{Bmatrix} 0 \\ 0 \\ 0 \\ \kappa(\frac{\partial v_y}{\partial x} - \frac{\partial v_x}{\partial y} - 2\omega_z) \\ \rho h \end{Bmatrix} \qquad (4.28)$$

Angular momentum $\rho j \omega_z$ is implemented as a user-defined function, and must be assigned its own separate equations and boundary conditions in the solver.

Initial and Boundary Conditions

To observe the transfer of energy among various eddies, an initial spectrum of energies was specified at the inlet of a 10 m domain. A cylinder was placed at x = 0. No-slip boundary conditions were set at the surface of the cylinder. At the inlet of x = -5, the gyration was specified to give an energy spectrum of the form:

$$E(k) = u_o^2 (\frac{k}{k_o})^2 exp[-2(\frac{k}{k_o})^2] \qquad (4.29)$$

Here, u_o is the root-mean-square velocity, k is a wavenumber of a given oscillation in the energy, and k_o is the wavenumber yielding the maximum energy in the spectrum.

The spectrum was chosen to match the spectrum produced by Lee to generate a low 7 Reynolds number for turbulence.[97] Here, the Reynolds number was defined to be $Re = \frac{\rho u_o}{(\mu + \kappa k_o}$ so as to have a dimensionless number that captures the forces on the length scale of the eddies.[97] The initial Reynolds number was set at 16. and k_o set to be 4, following Lee.[97] In MCT, these disturbances are produced by the gyration term, ω_z. Therefore, the initial conditions were specified such that $E(k) = \frac{1}{2}\rho j \omega_z^2$ would be equal to the turbulent kinetic energy. The wavelengths were produced through a random number generator and served as the wavelengths of ω_z through an input sine wave. With these oscillations occurring throughout the domain, it was necessary to specify homogenous boundary conditions at the boundaries to prevent reflection of any disturbances back towards the shock wave. The magnitude of the wave for ω_z was set to be a maximum of $\frac{u_o}{\sqrt{j}}$. The maximum turbulent kinetic energy would then have the value $\frac{1}{2}\rho u_o^2$. The value of this root-mean-square velocity is determined by the specified turbulent Mach number. The definition and physical significance of this parameter will be discussed in the next subsection.

Material Properties

In Peddieson's treatment of micropolar fluids, he used three non-dimensonal parameters to gauge the onset of turbulence. These parameters can be extracted from the governing equations through dimensionless analysis.[70] For incompressible flow over a flat plate, these parameters have been used to produce turbulent velocity profiles within a boundary layer.[105] The parameters are defined as follows:

$$\alpha_1 = \frac{\kappa}{\mu}, \quad \alpha_2 = \frac{\kappa}{\rho\sqrt{j}\,U}, \quad \alpha_3 = \frac{\gamma}{\mu j} \tag{4.30}$$

In the flat plate study, α_1 proved to be the pivotal parameter in moving from a transitional to turbulent profile.[105] This parameter serves as a ratio between the microstructures' con-

tribution to the Cauchy stress, $\kappa\epsilon_{klm}\omega_{l,m}$ to the viscous diffusion term, μv_{ll} in the linear momentum equation 4.11. In other words, changes in the gyration of the microstructures leads to a tension in the fluid that disrupts the otherwise smooth laminar flow. The macroscopic viscous diffusion attempts to smooth disruptions created by differences in gyration, and so the balance of these forces is critical for determining whether a flow has reached turbulence. This result indicated that the tension created by differences in rotational motion of microstructures needed to exceed viscous diffusion by a considerable amount in order to maintain turbulence within an incompressible boundary layer.

Parameter	Value
α_1	99
α_2	.0014
α_3	.235
$M_t = \frac{u_o}{c}$	.14
$Re = \frac{\rho_\infty u_o}{\mu k_o}$	16.7

Table 4.1: *Dimensionless parameters α_n, Turbulent Mach Number M_t, and Reynolds number.*[105]

Table 4.1 gives the values of the three dimensionless parameters for α_n that successfully generated turbulence in the incompressible case. In addition, the table specifies the turbulent Mach number, defined by the expression $\frac{\sqrt{q}}{c}$, where q is the Reynolds stress defined in MCT as $j\omega_z^2$, and c is the sound speed at 298 K. For our initial conditions, this expression reduces to the fraction $\frac{u_o}{c}$. Therefore the value of u_o is determined from the initial turbulent Mach number. The value specified for M_t in the table indicates that the turbulent fluctuations produce sizable contributions to density and pressure fluctuations in the macroscopic flow. As mentioned earlier, numerical solvers often require low values of M_t in the free-stream turbulence to reproduce the interaction with the shock faithfully.[100] The problem of capturing sub-grid length scales becomes more important when the turbulence becomes more compressible, as the smallest eddies could be impacted by density fluctuations. This simulation incorporates no sub-grid models and will allow for the effects of compressible turbulence to be taken into account.

(a) Translational KE   (b) Turbulent KE   (c) Eddy Structure
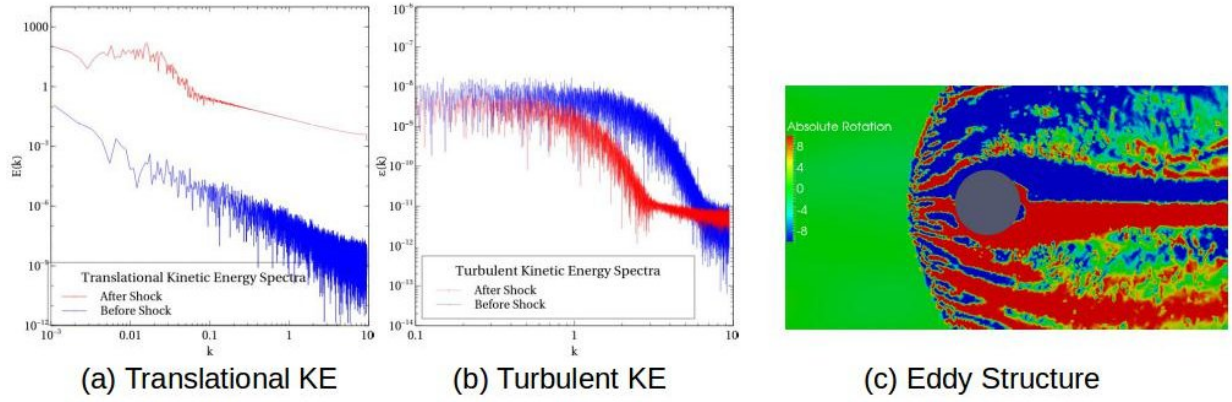
Figure 4.1: *Comparison of gyration energy $\frac{1}{2}\rho j\omega_z^2$ and translational energy $\frac{1}{2}\rho v^2$ behind shock at x = -2.5, highlighted in blue, and in front of shock at x = -.55, highlighted in red. Small wavelength eddies lose energy in interaction with shock wave and a transfer of energy is observed to translational kinetic energy for low wavenumbers. Plot of absolute rotation, $\epsilon_{klz}v_{l,k} - 2\omega_z$, shows structure and scope of eddies behind the shock*

4.1.3   Results

The spectra in figure 4.1 show Fast Fourier Transforms of the data taken at points before and after the shock. The data was taken only after the simulation yielded statistically stationary data. The point monitors were chosen to be constantly upstream and downstream of the shock. The vertical axes of the data correspond to the kinetic energy at each wavelength k. For the translational energies, the energy is low for the wavelengths before the shock because there are few oscillations in the translational velocity. The spike in translational energies and departure from constant slope for relatively low wavelengths demonstrates that the natural decay of kinetic energy was interrupted by the inverse cascade of energy from eddies due to their interactions with the shock wave. The random pattern in the spike of energies for wavelengths of $k < 0.1$ indicates that these were the wavelengths most directly affected by turbulent eddies. The translational energy decay is found to be linear in a log-log plot. When eddies are induced to transfer energy to translational motion, a nonlinear pattern of energy transfer is observed (see Figure 4.1 (a)).

The amplification of turbulent kinetic energy at all eddy wavelengths observed by Lee

et al for all was not observed here.[97] The shapes of the gyration energy spectra, however, correspond well with typical TKE spectra.[97] The largest eddies still produce the highest level of energy and gradually transfer their energy to smaller eddies through energy cascade and eventually dissipation. In this case, the turbulent kinetic energy spectrum show a trend of a loss of energy for short wavelength eddies after the turbulence passes through the shock. The TKE spectrum after the shock shows a spread in the distribution of eddy sizes. The largest and smallest eddy energies come close to pre-shock energy levels, suggesting that different eddies are compressed or expanded upon passing through the shock. This is consistent with the relatively high value of M_t, which allowed for more compressibility in our turbulent fluctuations.

Figure 4.1 also depicts the eddy structure behind the shock through the absolute rotation, defined by $\epsilon_{klz} v_{l,k} - 2\omega_z$. This quantity measures the difference between the self-spinning motion of the microstructures, measured by the gyration ω_z, and the macroscopic angular velocity, captured by half of the vorticity. When the gyration of the microstructures is equal to the macroscopic angular velocity, the absolute rotation vanishes and the governing equations for MCT reduce to the Navier-Stokes equations.[17] After the shock, the absolute rotation jumps in magnitude and reveals the structure of the eddies near the cylinder. This picture illustrates that the flow behind the shock is multi-scale. The gyration does not scale with the vorticity and is non-zero. Therefore, absolute rotation must contribute to the angular momentum equation 4.12 governing the rotation and bending of the eddies in the fluid. Furthermore, the flow behind the shock lacks symmetry and demonstrates a wide scale of eddy sizes, consistent with the random and multi-scale character of turbulence.[107]

4.1.4 Discussion

The preceding simulation gives an example of MCT generating compressible turbulent flow using the parameter values that achieved turbulent incompressible profiles in the previous chapter. The preeminence of the coupling coefficient reinforces comparisons between the kinetic and MCT descriptions. The turbulent kinetic energy spectra generated demonstrate

similar shapes to traditional spectra obtained in the literature. A clear case of inverse cascade of energy from turbulent eddies to the macroscopic motion of the flow is demonstrated by the nonlinear spike shown in the translational energies. The shape of the spectra indicate that MCT is able to obtain reasonable approximations of the physical behavior of eddies as they pass through the shock. The shape and structure of the turbulence can be visualized by observing the amplification of the absolute rotation after the shock, providing an alternative method of observing turbulence structure unavailable to DNS. The spectra were obtained without the need for local models near the shock and without sub-grid scale models. In the small length scale regimes where compressible turbulent boundary layers interact with oncoming shocks, Morphing Continuum Theory should serve as a useful tool for future numerical simulations. Still, this data was not compared with experimental data for compressible turbulence flows, a task left for section 4.2.

4.2 Transonic Flow over an Axisymmetric Hill

The demand for comprehensive, robust, and efficient numerical methods for modeling turbulence, while also yielding new physical insights into well-studied cases, is a continuous challenge to each new model.[108–111] The reliability of direct numerical simulation (DNS) in producing results that conform to experimental data is well documented, but these results are obtained at the expense of considerable computational resources.[14–17;106] The primary difficulty is the ability to resolve all relevant scales of motion, and in particular the smallest eddies. For these eddies, viscous diffusion of energy into heat is the primary mode of energy transfer. Since this cascade process is how energy is ultimately dissipated, no complete description of turbulent physics can omit these scales of motion. In order to resolve these eddies in DNS, the mesh must be continuously refined, driving up the computational costs.

Due to this hurdle, the Navier-Stokes equations have been modified with averaging or filtering techniques, producing the familiar large-eddy simulation (LES) and Reynolds-averaged Navier-Stokes (RANS) methods. Though these techniques do obtain credible results at cheaper costs, they still require closure models that change depending on the system being

studied. Typically, different versions of well-tested models are applied to canonical problems to test their viability, cost, and potential for solving more complex problems. Rodi et al's tests of different versions of the $k - \epsilon$ model for vortex-shedding flow illustrate the limits of various closure models and the occasional necessity of combining different models to approximate increasing levels of turbulence around a bluff body.[109] Walters and Coljkat proposed a three-equation model that incorporated closure models for the RANS equations based on the transport of different types of fluctuations to different regimes of the flow.[86] Depending on the nature of the results, or the geometry of the flow, different RANS models may be utilized. These models do not come from any first principles and are typically *ad hoc*, based off particular experiments or observations. They can be successful in adapting to new problems. Still, the smallest relevant length scales in turbulent motion may be smoothed over in the case of averaging, or filtered out as in the case of LES.

Developing a theory that captures these smallest length scales without resorting to *ad hoc* closure models is the goal of morphing continuum theory (MCT).[17;70;87–89] When the dynamics of a fluid's inner structure are considered, the resulting governing equations provide new terms that account for the motion or deformation of individual eddies. These terms arise from the independent local rotation of finite-sized particles in the fluid that give the fluid its inner structure. Recent successes in numerical simulations of two-dimensional boundary layer flows and compressible turbulent flows have produced visualizations of shock-turbulent interactions, turbulent kinetic energy transfer, transitional profiles, and other experimental fluids phenomena.[77;105;112] The key to these simulations is the ability to generate data consistent with experiment and DNS results, without the associated high computational costs.[17;77;105;112] Additionally, the new variable of local rotation, the new material properties associated with the inner structure, and the new governing equations allow for alternative strategies of visualizing large structures within the flow. These tools can help with the visualization of three-dimensional turbulent boundary layer flow. To prove MCT's applicability to physical cases of turbulence, the theory must be able to capture the structures involved in three-dimensional turbulence. This paper will derive new, objective, mathematical tools from MCT for visualizing structures within the three-dimensional flow.

The aim of this paper is to demonstrate the capability of MCT to produce compressible, three-dimensional, turbulent flow data that demonstrate at least qualitative consistency with experimental and numerical results. In addition, the effectiveness of the objective Q-criterion will be tested in its ability to visualize structure in three-dimensional turbulence. Subsection 4.2.1 discusses the importance of having an objective Q-criterion, and derives this criterion using the strain-rate in MCT. Subsection 4.2.2 will deal with the conversion of the analytical equations to a form suitable for numerical application. The numerical values for the material properties will be introduced, with their values determined by key dimensionless parameters. Subsection 4.2.3 will produce the results from the three-dimensional compressible axisymmetric hill simulation and compare them with experimental and numerical data. Contour plots of the new, frame-indifferent Q-criterion will unveil large structures such as hairpin vortices within the flow. Finally, subsection 4.2.4 will present concluding remarks on the reliability of the new MCT data, the value added by the new objective Q-criterion, and the future of MCT in modeling three-dimensional turbulence.

4.2.1 The Q-criterion of MCT

The subject of the identification of a vortex has been discussed for decades, with various mathematical and physical arguments given for how to isolate true vortices in the flow.[113–116] Qualitative definitions involving swirling motion or quantitative arguments based on the presence of high vorticity were among the first criteria proposed to distinguish vortices in the flow. The Q-criterion, defined by Hunt, focused on restricting the value of the velocity-gradient tensor and requiring the existence of a local minimum in the pressure.[114]

This practice of determining which facets of the flow counted as true vortices continued with the study of invariants. The local pressure minimum criterion eventually evolved into a requirement that the well-known λ_2 invariant remain negative in the flow. In these cases, vortices become apparent for steady Navier-Stokes flows, with the observer sitting in a Gallilean coordinate system.[116] Haller noted, however, that simple rotations of the coordinate system caused both the Q and λ_2 criteria to break down. Haller's discussion expanded

into a broader investigation of what kind of criteria succeeded in identifying vortices, independent of the physical situation and choice of coordinate system. Specifically, the invariants used to determine the presence of a vortex needed to preserve "objectivity," or indifference to a precise change in the reference coordinate system.[68;116]

One invariant that satisfies this criterion emerges from the deformation-rate tensor, a_{ij}, defined in equation 4.1.[106] This strain encompasses the traditional strain-rate produced from the velocity gradient and adds the local rotation supplied by the gyration of individual particles. Including both of these motions is essential to calculating objective quantities in MCT. Eringen demonstrates that objectivity is maintained in a morphing continuum by taking into account macroscopic and sub-scale deformations simultaneously, both of which are featured in equation 4.1.[106] Only by accounting for these motions can a_{ij} remain indifferent to coordinate transformations. This characteristic of the deformation in MCT is essential for maintaining a rigorous standard for vortex identification. This paper will seek to reformulate the Q-criterion as a first step towards establishing an objective criterion for identifying a vortex.

From linear algebra, one invariant calculates the level of asymmetry in a two-dimensional matrix, e.g. the strain-rate tensor. Setting this invariant to be II_a, the expression for this value has the form:[113]

$$II_a = \frac{1}{2}(a_{ii}a_{jj} - a_{ij}a_{ji}) \qquad (4.31)$$

where a_{ij} is the deformation-rate tensor. If the fluid obeys the continuum assumption, then this expression expresses a balance between the magnitude of the vorticity and the shear strain rate.[113] Since the deformation-rate tensor in equation 4.1 contains the shear rate and the gyration, this new invariant involves a balance of more aspects of the flow.

If the expression for a_{ij} from equation 4.1 is substituted into equation 4.31, the invariant becomes:

$$II_a = \frac{1}{2}[(v_{i,i})(v_{j,j}) - (v_{j,i} + \epsilon_{jim}\omega_m)(v_{i,j} + \epsilon_{ijl}\omega_l)] \qquad (4.32)$$

Multiplying and canceling the appropriate terms yields:

$$II_a = \frac{1}{2}[v_{i,i}v_{j,j} - v_{j,i}v_{i,j} - 2v_{j,i}\epsilon_{ijm}\omega_m + 2\omega_m\omega_m] \tag{4.33}$$

where the identities $\epsilon_{jim} = -\epsilon_{ijm}$ and $\epsilon_{jim}\epsilon_{ijl} = -2\delta_{ml}$ have been employed. Letting all the indices go to their respective coordinates in the three-dimensional Euclidean coordinate system, it is clear that the diagonal terms associated with the compressibility of the fluid disappear when the indices from the shear terms equal one another. Therefore, the invariant used for vortex visualization in MCT under Euclidean coordinates has the form:

$$II_a = [v_{x,x}v_{y,y} + v_{x,x}v_{z,z} + v_{y,y}v_{z,z} - (v_{x,y}v_{y,x} + v_{x,z}v_{z,x} + v_{y,z}v_{z,y})$$
$$- (v_{y,x} - v_{x,y})\omega_z - (v_{x,z} - v_{z,x})\omega_y - (v_{z,y} - v_{y,z})\omega_x + \omega_x^2 + \omega_y^2 + \omega_z^2] \tag{4.34}$$

The final version of the invariant contains the expected shear strain-rate components from both the large and small scales of motion. The familiar velocity gradient terms, contained in the Q-criterion for the Navier-Stokes equations, are now balanced with the magnitude of the gyration for individual particles. If the gyration terms disappear, the Navier-Stokes Q-criterion is recovered.[113;114] This fact is a consequence of the governing equations of MCT reducing to the Navier-Stokes equations when the gyration is set to zero. Also, if the gyration equals zero and the macroscopic stresses cancel one another out, then the macroscopic flow simply has no preferred rotational direction. Finally, if all stresses become zero then, naturally, no vortical motion could possibly exist and the invariant dissapears once more. As observed by Jeong et al for the Navier-Stokes' Q-criterion, a non-zero value for equation 4.2.1 is expected to produce visible eddies but may not be sufficient to visualize a true vortex.[113] Future investigations into this criterion and how it relates to other formal definitions of vortices are needed to make a conclusive case that MCT identifies true vortices. Still, the new expression from MCT allows for a new objective tool of visualizing eddies and turbulent structures of various sizes in the three-dimensional flow.

4.2.2   Numerical Implementation

Kurganov-Noelle-Petrova Scheme

For this work, the finite volume method is used to discretize the MCT balance laws. The spatial domain is divided into connected control volumes, or cells, with the physical variables solved at the center of each cell.

The transport equation for any conserved property can be written in the following form:

$$\frac{\partial \phi}{\partial t} + \nabla \cdot (\mathbf{v}\phi) - \nabla \cdot (\Gamma_\phi \nabla \phi) = S_\phi \tag{4.35}$$

Here, ϕ refers to the transport variable, Γ_ϕ is the diffusion coefficient, and S_ϕ is the source function for ϕ. If $\phi = \rho$, equation 4.35 becomes the continuity equation 4.10. Setting $\phi = \rho v_i$ yields the linear momentum equation 4.11, while $\phi = j\rho\omega_i$ yields the new governing equation for the angular momentum 4.12. Finally, if $\phi = \rho E$ the new energy equation 4.13 is obtained.

The finite volume method requires that the governing equations in their integral form be satisfied over the control volume. Applying spatial integration to Eq. 4.35 gives:

$$\int_V \frac{\partial \phi}{\partial t} dV + \int_V \nabla \cdot (\mathbf{v}\phi) dV - \int_V \nabla \cdot (\Gamma_\phi \nabla \phi) dV = \int_V S_\phi dV \tag{4.36}$$

The diffusion term in equation 4.35 can be approximated as:

$$\int_V \nabla \cdot (\Gamma_\phi \nabla \phi) dV = \int_S (\Gamma_\phi \nabla \phi) \cdot d\mathbf{S} \approx \sum_f (\Gamma_\phi \nabla \phi)_f \cdot \mathbf{S}_f \tag{4.37}$$

where $\mathbf{S}_f$ represents the surface vector of the face, and $\sum_f$ denotes the summation over the faces of the control volume. The term $(\Gamma_\phi \nabla \phi)_f$ can be obtained from the weighted average of the gradients at the centroids of the face multiplied by the diffusivity at the centroid:

$$(\Gamma_\phi \nabla \phi)_f = g(\Gamma_\phi \nabla \phi)_O + (1 - g)(\Gamma_\phi \nabla \phi)_N \tag{4.38}$$

where the subscripts O and N represent the nodes at the center of the owner cells and neighbor cells respectively. Here, g is the geometric interpolation factor related to the position of the element face f with respect to the cell center O. The gradient term $\nabla \phi$ located at the

cell center is computed using the Green-Gauss theorem:[117]

$$(\nabla\phi)_c = \frac{1}{V_c}\sum_f \phi_f \mathbf{S}_f \tag{4.39}$$

The nonlinear convection term in equation 4.35 requires a special treatment. The scheme adopted for the convection term should be able to capture any shock waves and discontinuities, and at the same time avoid oscillations. The convection term can be approximated as:

$$\int_V \nabla\cdot(\mathbf{v}\phi)dV = \int_S (\mathbf{v}\phi)\cdot d\mathbf{S} \approx \sum_f \mathbf{v}_f\phi_f \cdot \mathbf{S}_f \tag{4.40}$$

Notable methods found in the literature that are able to effectively produce accurate non-oscillatory solutions are: piecewise parabolic method (PPM);[118] essentially non-oscillatory (ENO);[119;120] weighted ENO (WENO);[121] and the Runge-Kutta discontinuous Galerkin (RKDG) method.[122] All of these methods involve Riemann solvers, characteristic decomposition and Jacobian evaluation, making them troublesome to implement.

In the present solver a simple forward-Euler scheme is implemented for the unsteady term:

$$\int_V \frac{\partial\phi}{\partial t}dV = \frac{\phi_c^n - \phi_c^o}{\triangle t}V_c \tag{4.41}$$

where V_c represents the cell volume, the subscript c gives the cell center, and superscripts n and o refer to the new and old time values respectively. In these schemes, different temporal solvers can be substituted. One can input a higher-order Runge-Kutta time integration scheme to achieve a higher level of accuracy. Kurganov et al demonstrated that stability is achieved with the implementation of a modified Euler method.[123] For this scheme, the diffusion terms in the momenta equations are solved at the new time step, meaning that the implicit character that allows for numerical stability of the KNP algorithm is preserved. The scheme implemented in this study is a second-order semi-discrete, non-staggered scheme, introduced by Kurganov, Noelle and Petrova (KNP) as a generalization of the Lax-Friedrichs scheme.[123] The interpolation procedure from the cell center to the face center implemented

in this scheme is split into two directions corresponding to the outward or inward direction of the face normal:

$$\sum_f \mathbf{v}_f \phi_f \mathbf{S}_f = \sum_f \left[\alpha \mathbf{S}_{f+} \mathbf{v}_{f+} \phi_{f+} + (1-\alpha) \mathbf{S}_{f-} \mathbf{v}_{f-} \phi_{f-} + \boldsymbol{\omega}_f (\phi_{f-} + \phi_{f+}) \right] \qquad (4.42)$$

where $\mathbf{S}_{f+}$ is the same as $\mathbf{S}_f$ and $\mathbf{S}_{f-} = -\mathbf{S}_f$. The subscript $f+$ is denoted for the directions coinciding with $\mathbf{S}_{f+}$, and $f-$ for the opposite direction, α the weighted coefficient, and ω_f is the diffusive volumetric flux. The two terms $\mathbf{S}_{f+} \mathbf{v}_{f+} \phi_{f+}$ and $\mathbf{S}_{f-} \mathbf{v}_{f-} \phi_{f-}$ in equation 4.42 represent the flux evaluated at the $\mathbf{S}_{f+}$ and $\mathbf{S}_{f-}$ directions respectively. The last term, $\boldsymbol{\omega}_f (\phi_{f-} + \phi_{f+})$, is an additional diffusive term based on the maximum speed of propagation of any discontinuity that may exist at the face. The weighting coefficient α is based on the local speed of propagation shown below:

$$\psi_{f+} = max \left(c_{f+} |\mathbf{S}_f| + \phi_{f+}, c_{f-} |\mathbf{S}_f| + \phi_{f-}, 0 \right) \qquad (4.43)$$

$$\psi_{f-} = max \left(c_{f+} |\mathbf{S}_f| - \phi_{f+}, c_{f-} |\mathbf{S}_f| - \phi_{f-}, 0 \right) \qquad (4.44)$$

Here c is the speed of sound of the fluid. The weighting factor is:

$$\alpha = \frac{\psi_{f+}}{\psi_{f+} + \psi_{f-}} \qquad (4.45)$$

and the diffusive volumetric flux is:

$$\boldsymbol{\omega}_f = \alpha(1-\alpha)(\psi_{f+} + \psi_{f-}) \qquad (4.46)$$

Initial and Boundary Conditions

An inlet boundary layer profile with a thickness of $\delta = 0.039m$ was specified with an otherwise uniform flow of $M_\infty = 0.6$ at the inlet of a $20H \times 2.305H \times 10H$ domain with $H = 0.078m$ as per Castagna.[124] The inflow velocity profile was specified by using the mean velocity values of Castagna's precursor simulation[124] and comparing the profile with the inflow profile measured experimentally by Simpson.[125] Figure 4.3 shows that the inflow profiles match very well near the wall and overpredict the velocity in the log layer where $y^+ > 60$. The profiles share a boundary layer thickness of $\delta = \frac{H}{2} = 0.039m$. This discrepancy was kept

81

to see if MCT could still capture experimental flow phenomena in the bulk flow. Turbulent fluctuations were specified by equating the root-mean-square (rms) of the new variable of gyration with the root-mean-square (rms) velocities specified by Castagna and compared with Spalart.[124;126] Figure 4.4 compares the normalized root-mean-square data from MCT and Castagna with the experimental data obtained by Spalart.[126] The discrepancies are the same for both MCT and Castagna, since Castagna's data was directly transferred to the gyration variable, via the expression $\sqrt{j}\omega_{i,rms} = u_{i,rms}$. Therefore, the kinetic energy generated by fluctuations in Castagna's velocity profile matches the rotational kinetic energy produced by the gyration. Discrepancies between the DNS and experimental data were most notable in the log-layer. These discrepancies were preserved in the gyration, again to see if MCT could still produce better agreement with experiment given the same initial flow data.

Inflow density, total viscosity $\mu + \kappa$, and freestream velocity U_∞, were all set to ensure

(a) Internal Mesh (b) Bump Mesh
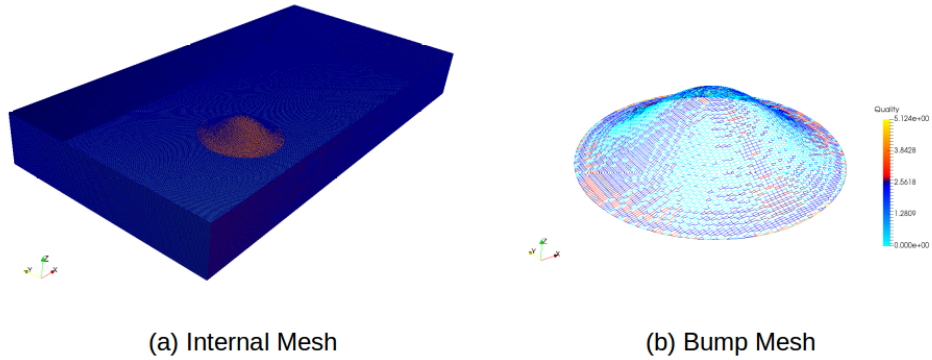
Figure 4.2: *Wireframe of the meshes for the rectangular domain and hill. Axisymmetric hill was set at 8.4H away from the interior, to allow for flow to develop on leeward side and to prevent effects from outlet. The bump mesh was tailored to the curvature of the hill. The hill radius was set at $R = 2H$ according to Castagna.[124]*

the Reynolds number, Re_H, based on the height H matched Castagna's value of 6500. The time-step for the MCT simulations was 5×10^{-8} s, shorter than that of Castagna's value of 3.04×10^{-5} s. The smaller mesh cells near the wall required these small time step values, but the resulting data benefited from increased temporal accuracy. Non-reflective boundary
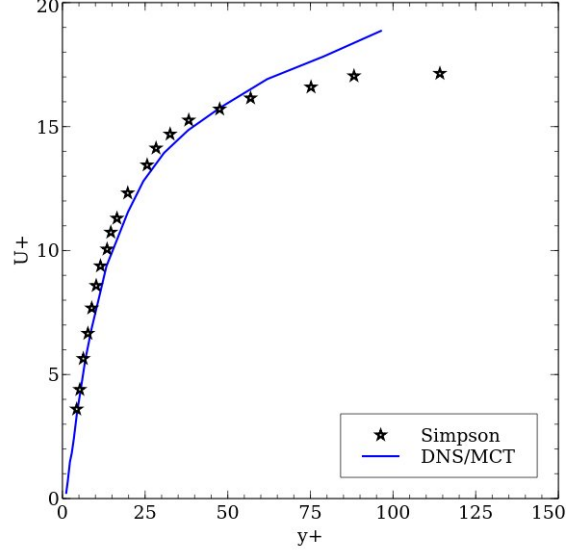
Figure 4.3: *Comparison of DNS inlet profile obtained by Castagna[124] from a precursour simulation with the experimental profile used by Simpson.[125]*
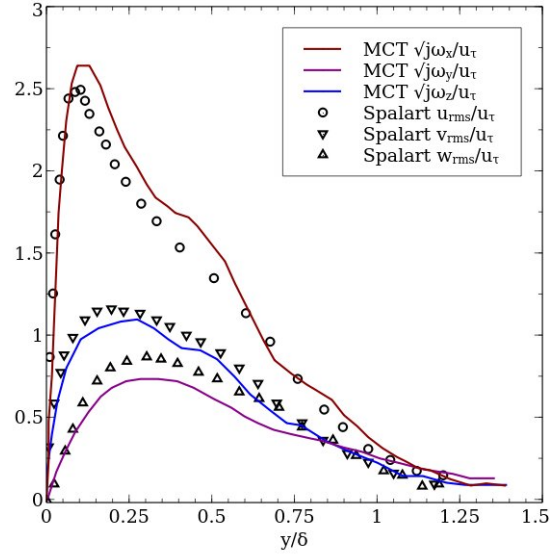
Figure 4.4: *Comparison of MCT/DNS velocity perturbations the experimental profile obtained by Spalart.[126]*

conditions were set at the top and outlet of the domain to prevent unphysical pressure effects from affecting the dynamics at the hill and to follow Castagna's setup.[124] Periodic boundary conditions were set in the spanwise direction, also in line with Castagna's conditions.[124] Zero gradient, and no-slip boundaries for the velocity, were set at the floor and hill. The mesh near the hill was tailored to the shape of the hill, determined by the mathematical functions

83

Parameter	Value
Maximum Aspect Ratio	8.62886
Time Step	5×10^{-8} s
Maximum Skewness	5.124
Δy_{min}^{+}	0.148
Number of cells: $y^{+} < 10$	30
Total Number of Cells	6.72×10^{6}

Table 4.2: *Parameters for mesh quality and time resolution used in MCT simulations*

set in Castagna.[124] Table 4.2 lists the key statistics associated with this custom mesh. A key note is the number of cells for this mesh, totaling around 6.7M elements. With the unstructured mesh, however, the viscous sublayer, defined by the limit $y^{+} < 10$, contained 30 cells as opposed to the 10 cells needed in Castagna's mesh.[124] Still, the argument that MCT can provide results comparable to DNS data without the associated computational costs is supported by the dramatic decrease in mesh cell number.

Material Properties

Three non-dimensonal parameters to gauge the onset of turbulence are introduced by Peddieson[70] and are later explained by Wonnell and Chen.[112] These parameters can be extracted from the governing equations through dimensionless analysis.[70] For incompressible flow over a flat plate, these parameters produced turbulent velocity profiles within a boundary layer that matched experimental data produced by the European Research Community on Flow, Turbulence and Combustion (ERCOFTAC).[95,105] The parameters are defined as follows:

$$\alpha_1 = \frac{\kappa}{\mu}, \ \ \alpha_2 = \frac{\kappa}{\rho\sqrt{j}\,U}, \ \ \alpha_3 = \frac{\gamma}{\mu j} \tag{4.47}$$

In the flat plate study, α_1 proved to be the pivotal parameter in matching an experimental turbulent profile.[105] This parameter serves as a ratio between the particles' contribution to the Cauchy stress, $\kappa\epsilon_{klm}\omega_{m,l}$ to the classical viscous diffusion term, μv_{ll}, in the linear momentum equation 4.11. Local variation in the gyration of the particles leads to a tension in the fluid that disrupts the otherwise smooth laminar flow. The classical viscous diffusion attempts to smooth disruptions created by differences in gyration, and so the balance of

these forces is critical for determining whether a flow has reached a turbulent state. This result indicates that the tension created by differences in rotational motion of particles needs to exceed viscous diffusion by a considerable amount in order to maintain turbulence within an incompressible boundary layer.

Table 4.3 gives the values of the three dimensionless parameters for α_n that successfully generated turbulence in the incompressible case. The problem of capturing sub-grid length scales becomes more important when the turbulence becomes more compressible, as the smallest eddies could be impacted by density fluctuations. The balance of compressibility with viscous fluctuations occurs at all scales of motion. This balance is reflected in the new total viscosity, $\mu + \kappa$, of the fluid found in the Reynolds number, Re_H. The contribution of individual structures to the total viscous resistance of the fluid is captured through κ. This simulation incorporates no sub-grid models and will allow for the effects of compressible turbulence to be taken into account.

Parameter	Value
α_1	99
α_2	0.0014
α_3	0.235
$M_\infty = \frac{U_\infty}{c}$	0.6
$Re_H = \frac{\rho_\infty \breve{U}_\infty H}{\mu + \kappa}$	6500

Table 4.3: *Dimensionless parameters α_n, Mach Number M, and the boundary layer Reynolds number matching experiments and DNS.[105;124;125] Speed of sound determined for air at $T_\infty = 293K$*

4.2.3   Results

Results were obtained after the freestream flow made 1.2 trips through the domain to follow Castagna's example, or around $t = 0.009s$.[124] Figure 4.5 highlights the formation of the separation bubble on the windward side of the hill using streamlines of the flow along the centerline $y = 0$. The leeward side does not show any apparent separtion bubble. Meanwhile the outline of the MCT windward side bubble falls slightly below some of the recirculation in the MCT data. The reattachment point for the MCT data, at $x = -1.66H$, is slightly downstream of Castagna's point of $x = -1.7H$, but the size of the windward bubble in MCT

X = -2.69H

X = -1.66H
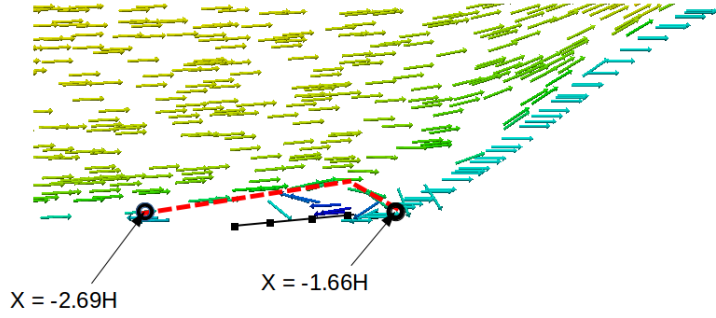
**Figure 4.5**: *Streamline plot compared with separation bubble boundaries obtained by Castagna.[124] MCT data demonstrate a far larger windward side separation bubble, but no significant separation on the leeward side. MCT windward bubble delineated by red dotted line. Large recirculation leads to greater buildup of pressure before the hill peak.*
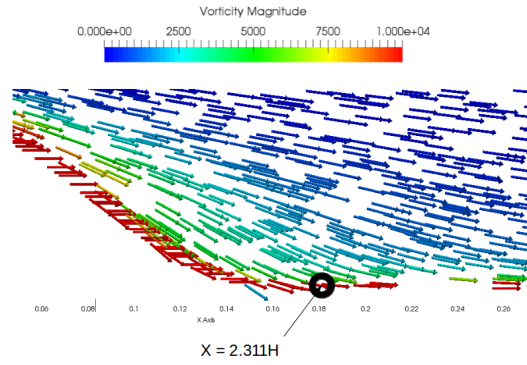
X = 2.311H

Figure 4.6: *Streamline plot of the leeward side of the bubble colored by the vorticity, with the local maximum peak at $x = 2.311H$ highlighted. Large differences in the vorticity likely responsible for pressure peak in this region.*

clearly exceeds that of Castagna's predictions. Inflow turbulence generated near the wall from the gyration and velocity fluctuations may have lead to a much earlier separation point for the MCT flow.

Figure 4.7 shows that experimental data for the pressure coefficient obtained from Simpson[125] line up more closely with MCT than the numerical results from Castagna.[124] These successful comparisons add confidence to the statement that numerical simulations of MCT produce realistic, physical flow data without the need for excessively dense grids or high computational costs. The pressure peak downstream of the hill appears at $x = 2.311H$.

86
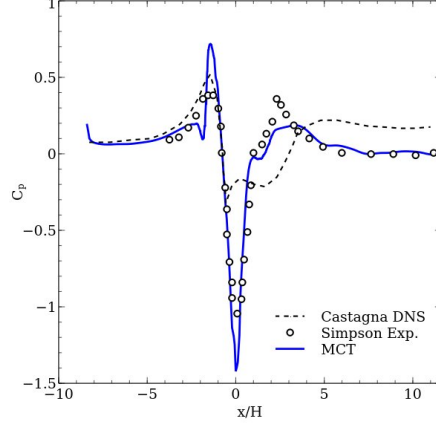
Figure 4.7: *Comparison of $C_p = \frac{p_{static} - p_{atm}}{.5 * \rho * U_\infty^2}$ between experimental data from Simpson, simulation data from Castagna, and numerical data along the centerline $z = 0$.*[124;125]

The DNS study failed to capture this peak, but MCT clearly demonsrates a local peak in this region. After this peak, MCT captures the further evolution of the wall pressure while Castagna's data overpredicts the surface pressure. Figure 4.6 shows the streamline plot on the leeward side of the hill colored by the magnitude of the vorticity. The rapid differences in the vorticity found near the secondary local peak are likely the cause of the local variance in pressure. Simpson noted that the pressure coefficient could be directly related to the vorticity flux,[125] and the resolution of this vorticity near the wall likely helps the resolution of the surface pressure.

Near the wall, turbulent fluctuations in MCT data behave in recognizable patterns, but contain noticeable differences from Navier-Stokes simulations. Figure 4.8 compares the turbulence intensities from Castagna[124] and MCT data at the same Reynolds number. Qualtiatively similar results are found near the edge of the boundary layer downstream of the hill, and near the wall upstream of the hill. MCT results demonstrate the characteristic peak and decline in turbulence intensity, with some noticeable differences in the wall-normal data. Downstream of the bump at $x = 11.6H$, the boundary layer in the MCT data shrinks considerably, leading to a wider spread of the turbulence intensity. The downstream behavior is likely affected by the formation of structures such as hairpin vortices, which will be discussed later.

More in-depth information of the structure of the flow is found using the Q-criterion
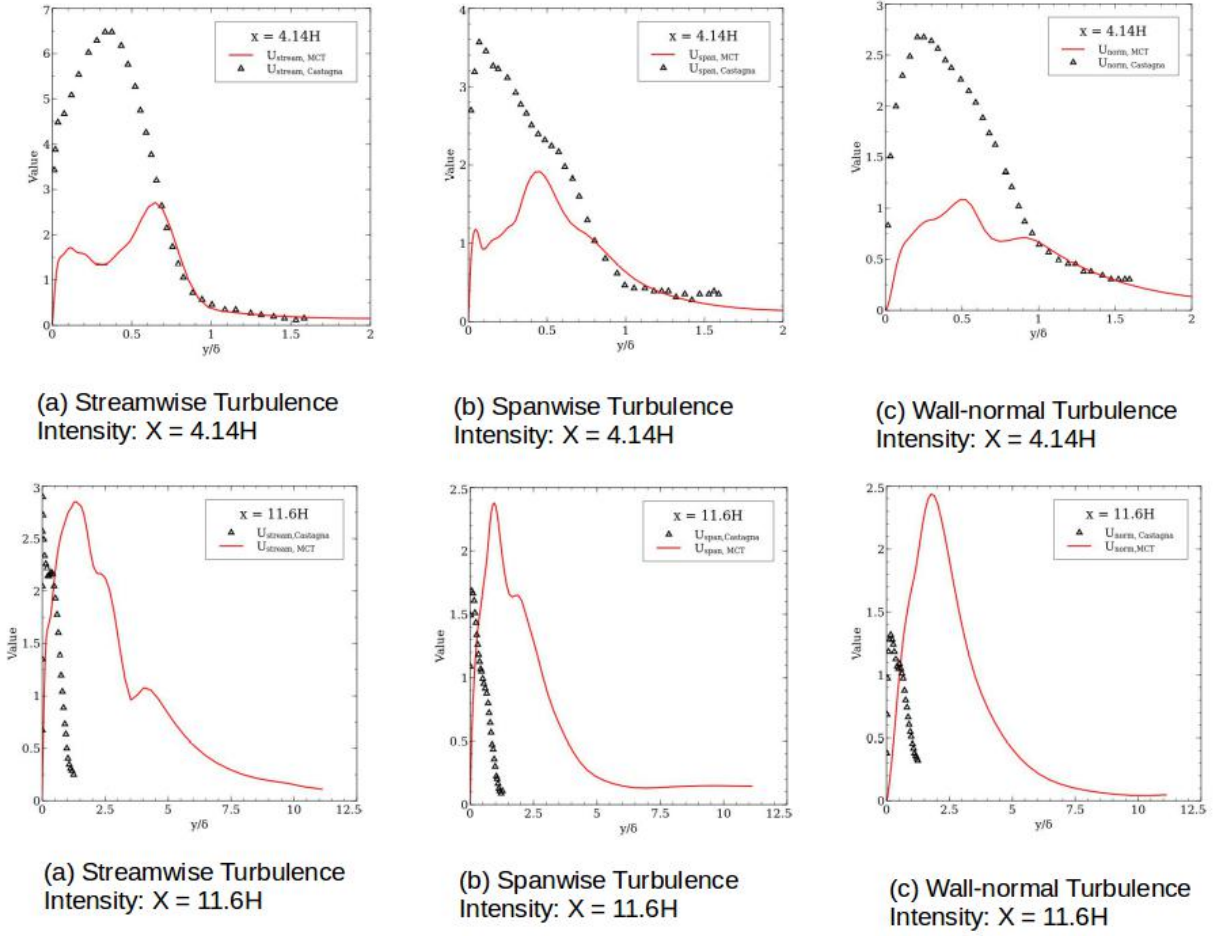
Figure 4.8: *Comparison of turbulence intensities, averaged in the spanwise direction, at x = 4.14H and x = 11.6H with DNS data obtained by Castagna.*[124]

defined by equation 4.2.1. Figure 4.9 shows the isosurface of the Q-criterion colored by the gyration. Figure 4.9 reveals structures within the turbulence, and particularly hairpin vortices downstream of the hill. Periodic regular hairpin vortices emerge for the Q-value of 5×10^5, with the arches of these vortices characterized by a low value of gyration. Since these structures are all described by the same value for the Q-criterion, these lower regions of gyration must correspond to higher values of velocity gradients. Here, the macroscale component of the flow is dominant. Near the floor, however, gyration plays a more critical role in determining local evolution of strucutre near the wall. Overall, the new Q-criterion

provides the tool to visualize the evolution of large-scale structures that form within the flow and see how small and large scale rotations affect the dynamics and topology of the bulk flow.
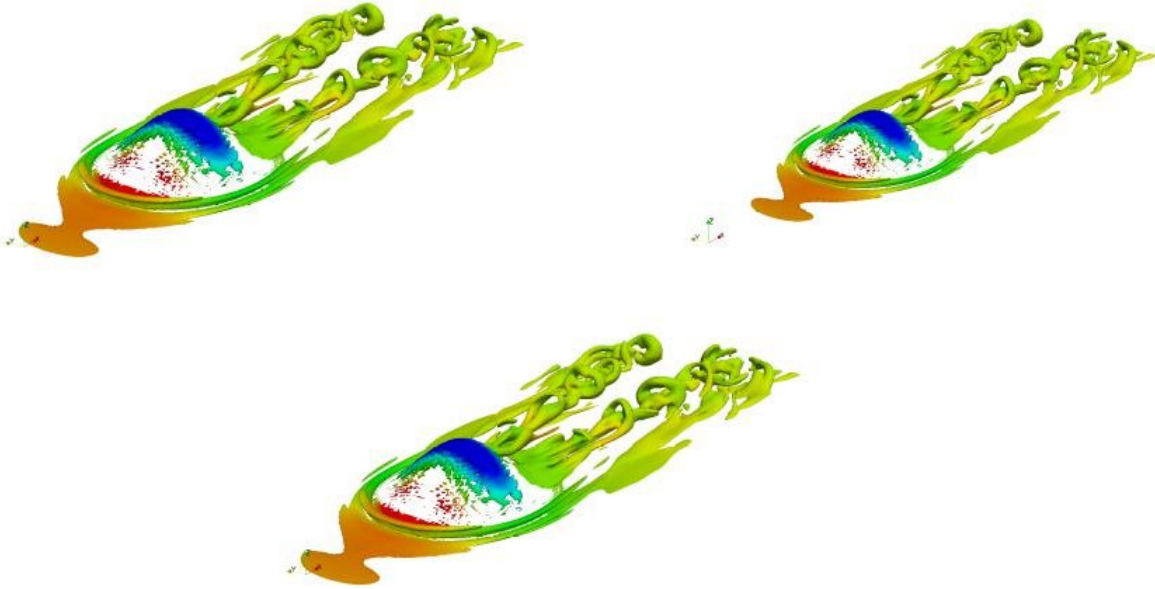
Figure 4.9: *Topology of hairpin vortices as visualized by the Q-criterion at 5×10^5, colored by the values of the gyration. Low gyration values for hairpin vortex indicate less variation in small-scale rotation.*

4.2.4 Discussion

Direct comparisons with the experimental results of Simpson[125] and the numerical data of Castagna[124] suggest that MCT can reproduce several aspects of flows simulated using the N-S equations on coarser grids and provide new tools for visualizing the behavior of flow structures. The obtained plot of the separation bubble lines on the windward side of the bump yields recirculation qualitatively similar to DNS results, and the associated pressure coefficient matches more closely with experimental data likely due to the presence of large vorticity differences near the wall. Turbulence intensities are shown to be qualitatively similar to Castagna's data, though differences are found primarily near the wall. The sharp

drop in mesh size as compared with Castagna[124] show that turbulent fluctuations, hairpin vortices, and pressure trends can be obtained without incurring high computational costs. Furthermore, MCT adds an objective Q-criterion for flow visualization, and can observe variation in local rotation in these structures through the gyration variable. Since the gyration acts on the flow only at the smallest scales, an analysis can be done to see how the inner structure of the flow affects the behavior of larger structures. The contour plots suggest that hairpin vortices contain regions of high gyration near the wall but develop regions of low gyration at the top. These regions can show where small or large scale differences in rotation predominate.

These initial comparisons with DNS and experimental data represent a first step for MCT to model compressible turbulence and identify vortices. The choice of parameters for material coefficients in MCT produce compressible turbulence results in closer alignment with experimental data. The new Q-criterion makes possible a new discussion of what variables and which length scales matter for the formation and evolution of structures within turbulent flows. Future work with canoncial cases involving the formation of vortices will illuminate how sub-scale motion affects the formation or decay of large and small vortices. Altering values for κ which denote the contribution of the inner structure to the evolution of turbulence will show the role gyration plays in the shape and stability of vortices. Identifying vortices and distinguishing them from large or small-scale eddies in the flow will give a better assessment of the structure of the turbulence, which will in turn yield better information on the turbulence intensity, pressure, and stress profiles. With the multiscale character of MCT, this information on the structure of turbulence can be obtained from smaller mesh sizes and fewer computational resources.

Chapter 5

Discussion and Conclusion

5.1 Discussion

The main purpose of this work was to give a kinetic description of fluids that would yield insight into material properties or coefficients that MCT had utilized to simulate turbulence without incurring the high costs of DNS. The key distinction between the classical Boltzmann approach to kinetic theory and the preceding derivation is the nature of the individual structures within the fluid. The Boltzmann particles contained no size and could only move via a translational velocity. Here, the particles contain a finite size and thus contain three extra degrees of freedom through their rotation. Therefore, an independent angular momentum equation was needed to account for the transport of this new rotation. This equation, in turn, introduced a new stress that focused entirely on the contribution of the gyration. This stress, unlike the familiar Cauchy stress, has no known counterpart in the classical kinetic description.

Each of these observations of the picture of the fluid portrayed by kinetic theory has a familiar backdrop within MCT. A morphing continuum does start with a space composed not of points but of finite-sized structures. Since these structures are all connected within a continuum, their application to more traditional fluid elements such as eddies makes it an attractive tool for attacking problems such as turbulence. Mathematical principles imbedded

in this continuum lead to new deformation rates, which in turn lead to new stress tensors. Hence, the Cauchy stress contains terms with no classical counterpart and a new moment stress is needed to deal with forces generated by local differences in rotation. One may be tempted to conclude that the physical meaning behind new coefficients in MCT is apparent by observing how the overall flow changes when their values are adjusted. The coupling of the linear and angular momenta equations in MCT, however, ensures that the coupling coefficient, κ, can play multiple roles. The relationship between κ and the more familiar coefficient associated with the kinematic viscosity, μ, has been shown to be more complex with the dimensional analysis done in chapter 3. These complications ensure the relevance of an approach designed to base the abstractions within MCT in a more realistic physical setting.

Due to the similarities between the morphing continuum of MCT and the collection of rotating particles in the kinetic approach, it is not surprising to see the two sets of equations match in form. With all of these new aspects introduced into a kinetic description, however, the relationship between the two approaches to flows with local spin needs more clarification. The kinetic approach discretizes the fluid in question, extrapolating the behavior of the fluid from the interaction of these particles. The associated model for the singular relaxation time will affect the expected values of all coefficients. Numerical simulations that test how well the expressions within the kinetic equations match with the parameters used in MCT will have to choose conditions that allow for a good approximation of the relaxation time, in addition to equilibrium temperature and number density. Turbulent gas flow, hypersonic flow, and high-altitude flows are some of the examples where kinetic theory can be tested with regards to MCT.

5.2   Conclusion

The first-order approximation to the Boltzmann-Curtiss equation has provided equations that give insight into the contribution of material parameters introduced by MCT. The equal expressions for the coefficient in front of the Cauchy stress and the viscous diffusion suggests

that the additional rotation of particles does not increase the total viscosity of the flow. When the Cauchy stress is non-zero, the kinetic equations indicate that the coupling coefficient, κ, must predominate in determining the total viscosity. Numerical simulations of transitional and turbulent flow provide evidence for this result. The kinetic equations reduce to the Type II Navier-Stokes form, with different expressions for the classical viscosity when the local rotation is equivalent to the angular velocity. Therefore, the additional rotation in the particles affects how the final viscosity depends on the number density, relaxation time, and temperature. Viscous resistance in a gas composed of spherical particles evidently changes when local rotation is no longer independent from macroscopic rotation, suggesting that the presence of the distinct local rotation generates viscous resistance. For incompressible and irrotational flows, however, the kinetic equations reduce to the classic kinetic equations derived from the Boltzmann approach. This result is consistent with the fact that the only difference between the current and classical approaches is the existence of the local rotation. The final equations demonstrate that kinetic theory can provide a physical framework for the mathematics and preliminary numerical results of MCT.

Future work with the kinetic description in this work can focus on the nonequilibrium effects generated in polyatomic gas flows discussed in chapter 2. The additional rotation present in polyatomic gases is not explicity accounted for by the classical Boltzmann distribution and is treated as an internal variable. These flows, however, demonstrate additional angular momentum which effects the collisional dynamics of the equilibrium flow, causing the true distribution function to depart greatly from the Boltzmann form. The Boltzmann-Curtiss distribution and its first-order approximation can help yield insight into the explicit contribution of local rotation to total viscosity, conductivity, relaxation, and other effects observed in non-equilibrium flows. Therefore, comparisons can reach beyond MCT and perhaps help this kinetic description become a key tool in analyzing polyatomic gas flows.

Bibliography

[1] V. Eswaran and S. B. Pope. Direct numerical simulations of the turbulent mixing of a passive scalar. *The Physics of Fluids*, 31(3):506–520, 1988.

[2] H. Le, P. Moin, and J. Kim. Direct numerical simulation of turbulent flow over a backward-facing step. *Journal of Fluid Mechanics*, 330:349–374, 1997.

[3] R. D. Moser, J. Kim, and N. N. Mansour. Direct numerical simulation of turbulent channel flow up to $Re_\tau = 590$. *Physics of Fluids*, 11(4):943–945, 1999.

[4] S. Pirozzoli, F. Grasso, and T. B. Gatski. Direct numerical simulation and analysis of a spatially evolving supersonic turbulent boundary layer at m= 2.25. *Physics of Fluids*, 16(3):530–545, 2004.

[5] J. H. Chen, A. Choudhary, B. De Supinski, M. DeVries, E. R. Hawkes, S. Klasky, W. K. Liao, K. L. Ma, J. Mellor-Crummey, N. Podhorszki, et al. Terascale direct numerical simulations of turbulent combustion using s3d. *Computational Science & Discovery*, 2(1):015001, 2009.

[6] X. Wu and P. Moin. Direct numerical simulation of turbulence in a nominally zero-pressure-gradient flat-plate boundary layer. *Journal of Fluid Mechanics*, 630:5–41, 2009.

[7] M. Lee and R. D. Moser. Direct numerical simulation of turbulent channel flow up to $Re_\tau \approx 5200$. *Journal of Fluid Mechanics*, 774:395–415, 2015.

[8] J. D. Anderson. *Hypersonic and high temperature gas dynamics*. AIAA, 2000.

[9] W. Hayes. *Hypersonic flow theory*. Elsevier, 2012.

[10] H. Struchtrup. Macroscopic transport equations for rarefied gas flows. In *Macroscopic Transport Equations for Rarefied Gas Flows*, pages 145–160. Springer, 2005.

[11] Y. B. Zel'Dovich and Y. P. Raizer. *Physics of shock waves and high-temperature hydrodynamic phenomena*. Courier Corporation, 2012.

[12] R. W. C. P. Verstappen and A. E. P. Veldman. Direct numerical simulation of turbulence at lower costs. *Journal of Engineering Mathematics*, 32(2-3):143–159, 1997.

[13] A. M. O. Smith and N. Gamberoni. Transition, pressure gradient, and stability theory. 1956.

[14] J. L. Van Ingen. A suggested semi-empirical method for the calculation of the boundary layer transition region. *Technische Hogeschool Delft, Vliegtuigbouwkunde, Rapport VTH-74*, 1956.

[15] R. D. Joslin, C. L. Streett, and C. L. Chang. Spatial direct numerical simulation of boundary-layer transition mechanisms: Validation of pse theory. *Theoretical and Computational Fluid Dynamics*, 4(6):271–288, 1993.

[16] J. Fürst, P. Straka, J. Příhoda, and D. Šimurda. Comparison of several models of the laminar/turbulent transition. In *EPJ Web of Conferences*, volume 45, page 01032. EDP Sciences, 2013.

[17] J. Chen, C. Liang, and J. D. Lee. Numerical simulation for unsteady compressible micropolar fluid flow. *Computers & Fluids*, 66:1–9, 2012.

[18] J. Smagorinsky. General circulation experiments with the primitive equations: I. the basic experiment. *Monthly Weather Review*, 91(3):99–164, 1963.

[19] M. Germano, U. Piomelli, P. Moin, and W. H. Cabot. A dynamic subgrid-scale eddy viscosity model. *Physics of Fluids A: Fluid Dynamics*, 3(7):1760–1765, 1991.

[20] D. K. Lilly. A proposed modification of the Germano subgrid-scale closure method. *Physics of Fluids A: Fluid Dynamics*, 4(3):633–635, 1992.

[21] P. M. Gerhart and R. J. Gross. *Fundamentals of Fluid Mechanics.* Addison-Wesley, 1985.

[22] K. Huang. *Statistical Mechanics.* John Wiley & Sons, 1987.

[23] T. J. R. Hughes, L. Mazzei, A. A. Oberai, and A. A Wray. The multiscale formulation of large eddy simulation: Decay of homogeneous isotropic turbulence. *Physics of Fluids*, 13(2):505–512, 2001.

[24] Y. Bazilevs, C. Michler, V. M. Calo, and T. J. R. Hughes. Isogeometric variational multiscale modeling of wall-bounded turbulent flows with weakly enforced boundary conditions on unstretched meshes. *Computer Methods in Applied Mechanics and Engineering*, 199(13-16):780–790, 2010.

[25] C. Liang, J. Chen, and J. D. Lee. Spectral difference solution of two-dimensional unsteady compressible micropolar equations on moving and deformable grids. In *Proceedings of the 50th AIAA Aerospace Sciences Meeting including the New Horizons Forum and Aerospace Exposition*, 2012.

[26] L. F. Richardson. *Weather Prediction by Numerical Process.* Cambridge University Press, 1922.

[27] C. F. Curtiss. The classical Boltzmann equation of a gas of diatomic molecules. *Journal of Chemical Physics*, 75:376–378, 1981.

[28] C. F. Curtiss. The classical Boltzmann equation of a molecular gas. *Journal of Chemical Physics*, 97:1416–1419, 1992.

[29] C. F. Curtiss and J. S. Dahler. Kinetic theory of nonspherical molecules. v. *Journal of Chemical Physics*, 38:2352–2363, 1963.

[30] R. S. C. She and N. F. Sather. Kinetic theory of polyatomic gases. *Journal of Chemical Physics*, 47:4978–4993, 1967.

[31] J. Chen. An advanced kinetic theory for morphing continuum with inner structures. *Reports on Mathematical Physics*, 80(3):317 – 332, 2017.

[32] A. C. Eringen. Theory of micropolar fluids. *Journal of Mathematics and Mechanics*, 16:1–18, 1966.

[33] J. O. Hirschfelder, R. B. Bird, and C. F. Curtiss. *Molecular theory of gases and liquids*. Wiley, 1964.

[34] J. T. Hynes, R. Kapral, and M. Weinberg. Molecular rotation and reorientation: Microscopic and hydrodynamic contributions. *Journal of Chemical Physics*, 69:2725–2733, 1978.

[35] J. T. Jenkins and M. W. Richman. Kinetic theory for plane flows of a dense gas of identical, rough, inelastic, circular disks. *Physics of Fluids*, 28:3485–3494, 1985.

[36] B. Rahimi and H. Struchtrup. Macroscopic and kinetic modelling of rarefied polyatomic gases. *Journal of Fluid Mechanics*, 806:437–505, 2016.

[37] C. Truesdell and W. Noll. The non-linear field theories of mechanics. In *The non-linear field theories of mechanics*. Springer, 2004.

[38] C. S. Wang-Chang, G. E. Uhlenbeck, and J De Boer. The heat conductivity and viscosity of polyatomic gases. *Studies in Statistical Mechanics*, 2:241, 1964.

[39] G. Ahmadi. Turbulent shear flow of micropolar fluids. *International Journal of Engineering Science*, 13(11):959–964, 1975.

[40] A. C. Eringen. *Microcontinuum field theories: I. Foundations and Solids*. Springer, 1999.

[41] A. C. Eringen. *Microcontinuum field theories: II. Fluent media*. Springer, 2001.

[42] A. D. Kirwan Jr. Theory of turbulent eddies. *The Physics of Fluids*, 10(9):S84–S86, 1967.

[43] V. K. Stokes. *Theories of fluids with microstructure: an introduction.* Springer Science & Business Media, 2012.

[44] J. Meng, Y. Zhang, N. G. Hadjiconstantinou, G. A. Radtke, and X. Shan. Lattice ellipsoidal statistical bgk model for thermal non-equilibrium flows. *Journal of Fluid Mechanics*, 718:347–370, 2013.

[45] A. Munafo, M. Panesi, and T. E. Magin. Boltzmann rovibrational collisional coarse-grained model for internal energy excitation and dissociation in hypersonic flows. *Physical Review E*, 89:023001, 2014.

[46] T. Arima, T. Ruggeri, and M. Sugiyama. Rational extended thermodynamics of a rarefied polyatomic gas with molecular relaxation processes. *Physical Review E*, 96:042143, 2017.

[47] B. C. Eu. Kinetic theory and irreversible thermodynamics. *Accounts of Chemical Research*, 19:153–160, 1986.

[48] B. C. Eu. *Nonequilibrium Statistical Mechanics: Ensemble Method.* Springer, 1998.

[49] B. C. Eu. *Generalized Thermodynamics: Thermodynamics of Irreversible Processes and Generalized Hydrodynamics.* Springer, 2002.

[50] R. S. Myong. Thermodynamically consistent hydrodynamic computational models for high-Knudsen-number gas flows. *Physics of Fluids*, 11:2788–2802, 1999.

[51] R. S. Myong. A computational method for Eu's generalized hydrodynamic equations of rarefied and microscale gasdynamics. *Journal of Computational Physics*, 168:47–72, 2001.

[52] R. S. Myong. A generalized hydrodynamic computational model for rarefied and microscale diatomic gas flows. *Journal of Computational Physics*, 195:655–676, 2004.

[53] H. Grad. Statistical mechanics, thermodynamics, and fluid dynamics of systems with an arbitrary number of integrals. *Communications on Pure and Applied Mathematics*, 5:455–494, 1952.

[54] S. R. De Groot and P. Mazur. *Non-Equilibrium Thermodynamics*. North-Holland, 1962.

[55] R. F. Snider and K. S. Lewchuk. Irreversible thermodynamics of a fluid system with spin. *Journal of Chemical Physics*, 46:3163–3172, 1967.

[56] V. K. Stokes. Couple stresses in fluids. *Physics of Fluids*, 9:1709–1715, 1966.

[57] D. J. Evans and W. B. Streett. Transport properties of homonuclear diatomics: II. dense fluids. *Molecular Physics*, 36:161–176, 1978.

[58] L. Boltzmann. Zur theorie der elastischen nachwirkung. *Annalen der Physik*, 241: 430–432, 1878.

[59] J. C. Maxwell. Clerk Maxwell's kinetic theory of gases. *Nature*, 8:122–123, 1873.

[60] S. I. Sandler and J. S. Dahler. Kinetic theory of loaded spheres. ii. *Journal of Chemical Physics*, 43:1750–1759, 1965.

[61] R. S. Myong. On the high Mach number shock structure singularity caused by overreach of maxwellian molecules. *Physics of Fluids*, 26:056102, 2014.

[62] J. G. Parker. Rotational and vibrational relaxation in diatomic gases. *Physics of Fluids*, 2:449–462, 1959.

[63] J. S. Dahler and N. F. Sather. Kinetic theory of loaded spheres. i. *Journal of Chemical Physics*, 38:2363–2382, 1963.

[64] L. Monchick. Small periodic disturbances in polyatomic gases. *Physics of Fluids*, 7: 882–896, 1964.

[65] E. H. Carnevale, C. Carey, and G. Larson. Ultrasonic determination of rotational collision numbers and vibrational relaxation times of polyatomic gases at high temperatures. *Journal of Chemical Physics*, 47:2829–2835, 1967.

[66] L. Monchick, A. N. G. Pereira, and E. A. Mason. Heat conductivity of polyatomic and polar gases and gas mixtures. *Journal of Chemical Physics*, 42:3241–3256, 1965.

[67] P. Valentini, C. Zhang, and T. E. Schwartzentruber. Molecular dynamics simulation of rotational relaxation in nitrogen: Implications for rotational collision number models. *Physics of Fluids*, 24:106101, 2012.

[68] J. Chen. Morphing continuum theory for turbulence: Theory, computation, and visualization. *Physical Review E*, 96:043108, 2017.

[69] J. Chen, J. D. Lee, and C. Liang. Constitutive equations of micropolar electromagnetic fluids. *Journal of Non-Newtonian Fluid Mechanics*, 166:867–874, 2011.

[70] J. Peddieson. An application of the micropolar fluid model to the calculation of a turbulent shear flow. *International Journal of Engineering Science*, 10:23–32, 1972.

[71] G. M. Kremer. *An introduction to the Boltzmann equation and transport processes in gases*. Springer Science & Business Media, 2010.

[72] V. K. Gupta, P. Shukla, and M. Torrilhon. Higher-order moment theories for dilute granular gases of smooth hard spheres. *Journal of Fluid Mechanics*, 836:451501, 2018.

[73] GR Fowles and GL Cassidy. *Analytical Mechanics*. Thomson, 2004.

[74] D. Baraff. An introduction to physically based modeling: rigid body simulation iunconstrained rigid body dynamics. *SIGGRAPH Course Notes*, 1997.

[75] H. Chen, S. Kandasamy, S. Orszag, R. Shock, S. Succi, and V. Yakhot. Extended Boltzmann kinetic equation for turbulent flows. *Science*, 301(5633):633–636, 2003.

[76] P. L. Bhatnagar, E. P. Gross, and M. Krook. A model for collision processes in gases. i. small amplitude processes in charged and neutral one-component systems. *Physical Review*, 94:511, 1954.

[77] L. B. Wonnell and J. Chen. Morphing continuum theory: Incorporating the physics of microstructures to capture the transition to turbulence within a boundary layer. *Journal of Fluids Engineering*, 139:011205, 2017.

[78] P. Curie. *Oeuvres de Pierre Curie: publiées par les soins de la Société de physique*. Gauthier-Villars, 1908.

[79] S. Montero and J. Pérez-Ríos. Rotational relaxation in molecular hydrogen and deuterium: Theory versus acoustic experiments. *Journal of Chemical Physics*, 141:114301, 2014.

[80] K. Berger, S. Rufer, R. Kimmel, and D. Adamczak. Aerothermodynamic characteristics of boundary layer transition and trip effectiveness of the hifire flight 5 vehicle. In *39th AIAA Fluid Dynamics Conference*, page 4055.

[81] O. Reynolds. An experimental investigation of the circumstances which determine whether the motion of water in parallel channels shall be direct or sinuous and of the law of resistance in parallel channels. *Philos. Trans. R. Soc. London*, 174:935–82, 1883.

[82] J. Van Ingen. The e^N method for transition prediction. historical review of work at tu delft. In *38th Fluid Dynamics Conference and Exhibit*, page 3830, 2008.

[83] A.E. Von Doenhoff and A.L. Braslow. Effect of distributed surface roughness on laminar flow. chapter of boundary layer and flow control-its principles and applications, volume 2, edited by GV Lachmann, 1961.

[84] O. Vermeersch. *Étude et modélisation du phénomène de croissance transitoire pour des couches limites incompressibles et compressibles*. PhD thesis, Toulouse, ISAE, 2009.

[85] B. Aupoix, D. Arnal, H. Bézard, B. Chaouat, F. Chedevergne, S. Deck, V. Gleize, P. Grenard, and E. Laroche. Transition and turbulence modeling. *AerospaceLab*, (2): 1–13, 2011.

[86] D. K. Walters and D. Cokljat. A three-equation eddy-viscosity model for reynolds-averaged navier–stokes simulations of transitional flow. *Journal of Fluids Engineering*, 130(12):121401, 2008.

[87] J. Heinloo. Formulation of turbulence mechanics. *Physical Review E*, 69(5):056317, 2004.

[88] A. D. Kirwan. Boundary conditions for micropolar fluids. *International Journal of Engineering Science*, 24(7):1237–1242, 1986.

[89] R. Mehrabian and G. Atefi. A Cosserat continuum mechanical approach to turbulent channel pressure driven flow of isotropic fluid. *Journal of Dispersion Science and Technology*, 29(7):1035–1042, 2008.

[90] A. D. Kirwan Jr and N. Newman. Plane flow of a fluid containing rigid structures. *International Journal of Engineering Science*, 7(8):883–893, 1969.

[91] S. Kawai and J. Larsson. Wall-modeling in large eddy simulation: Length scales, grid resolution, and accuracy. *Physics of Fluids*, 24(1):015105, 2012.

[92] M. Alizadeh, G. Silber, and A. G. Nejad. A continuum mechanical gradient theory with an application to fully developed turbulent flows. *Journal of Dispersion Science and Technology*, 32(2):185–192, 2011.

[93] R Drouot and G. A. Maugin. Phenomenological theory for polymer diffusion in non-homogeneous velocity-gradient flows. *Rheologica Acta*, 22(4):336–347, 1983.

[94] R. D. Mindlin. Micro-structure in linear elasticity. *Archive for Rational Mechanics and Analysis*, 16(1):51–78, 1964.

[95] J. Coupland. Ercoftac special interest group on laminar to turbulent transition and retransition. *T3A and T3B Test Cases*, 1990.

[96] R. A. Humble, F. Scarano, and B. W. Van Oudheusden. Experimental study of an incident shock wave/turbulent boundary layer interaction using piv. *AIAA paper*, 3361: 2006, 2006.

[97] S. Lee, S. K. Lele, and P. Moin. Interaction of isotropic turbulence with shock waves: effect of shock strength. *Journal of Fluid Mechanics*, 340:225–247, 1997.

[98] B. A. Bhutta and C. H. Lewis. PNS predictions of external/internal hypersonic flows for NASP propulsion applications. Vra–tr–90–01, VRA, Inc., Blacksburg, VA, June 1990.

[99] E. W. Miner and C. H. Lewis. Hypersonic ionizing air viscous shock-layer flows over nonanlytic blunt bodies. Nasa cr–2250, May 1975.

[100] F. Ducros, V. Ferrand, F. Nicoud, C. Weber, D. Darracq, C. Gacherieu, and T. Poinsot. Large-eddy simulation of the shock/turbulence interaction. *Journal of Computational Physics*, 152(2):517–549, 1999.

[101] P. S. Rawat and X. Zhong. Numerical simulation of shock-turbulence interactions using high-order shock-fitting algorithms. In *Proceedings of the 48th AIAA Aerospace Sciences Meeting Including the New Horizons Forum and Aerospace Exposition, Aerospace Sciences Meetings*, volume 114, 2010.

[102] S. Ghosal, T. S. Lund, P. Moin, and K. Akselvoll. A dynamic localization model for large-eddy simulation of turbulent flows. *Journal of Fluid Mechanics*, 286:229–255, 1995.

[103] Y. Andreopoulos, J. H. Agui, and G. Briassulis. Shock wave-turbulence interactions. *Annual Review of Fluid Mechanics*, 32(1):309–345, 2000.

[104] J. Ryu and D. Livescu. Turbulence structure behind the shock in canonical shock–vortical turbulence interaction. *Journal of Fluid Mechanics*, 756, 2014.

[105] J. Chen and L. Wonnell. A multiscale morphing continuum description for turbulence. In *Bulletin of the American Physical Society*, volume 60. 68th Annual Meeting of the APS Division of Fluid Dynamics, 2015.

[106] A. C. Eringen. Simple microfluids. *International Journal of Engineering Science*, 2(2):205–217, 1964.

[107] H. Tennekes and J. L. Lumley. *A first course in turbulence.* MIT press, 1972.

[108] D. C. Wilcox. Reassessment of the scale-determining equation for advanced turbulence models. *AIAA Journal*, 26(11):1299–1310, 1988.

[109] W. Rodi. Comparison of LES and RANS calculations of the flow around bluff bodies. *Journal of Wind Engineering and Industrial Aerodynamics*, 69:55–75, 1997.

[110] S. H. Park and J. H. Kwon. Implementation of k-omega turbulence models in an implicit multigrid method. *AIAA Journal*, 42(7):1348–1357, 2004.

[111] H. Pitsch. Large-eddy simulation of turbulent combustion. *Annual Review of Fluid Mechanics*, 38:453–482, 2006.

[112] L. B. Wonnell and J. Chen. A morphing continuum approach to compressible flows: Shock wave-turbulent boundary layer interaction. In *46th AIAA Fluid Dynamics Conference*, pages AIAA 2016–4279, 2016.

[113] J. Jeong and F. Hussain. On the identification of a vortex. *Journal of Fluid Mechanics*, 285:69–94, 1995.

[114] J. C.R. Hunt, A. A. Wray, and P. Moin. Eddies, streams, and convergence zones in turbulent flows. *Center for Turbulence Research CTR-S88*, page 193, 1988.

[115] Q. Chen, Q. Zhong, M. Qi, and X. Wang. Comparison of vortex identification criteria for planar velocity fields in wall turbulence. *Physics of Fluids*, 27(8):085101, 2015.

[116] G. Haller. An objective definition of a vortex. *Journal of Fluid Mechanics*, 525:1–26, 2005.

[117] M. Darwish, A. Abdul Aziz, and F. Moukalled. A coupled pressure-based finite-volume solver for incompressible two-phase flow. *Numerical Heat Transfer, Part B: Fundamentals*, 67(1):47–74, 2015.

[118] P. Colella and P. R. Woodward. The piecewise parabolic method (PPM) for gas-dynamical simulations. *Journal of Computational Physics*, 54(1):174–201, 1984.

[119] C. W. Shu and S. Osher. Efficient implementation of essentially non-oscillatory shock-capturing schemes. *Journal of Computational Physics*, 77(2):439–471, 1988.

[120] A. Harten, B. Engquist, S. Osher, and S. R. Chakravarthy. Uniformly high order accurate essentially non-oscillatory schemes, iii. *Journal of Computational Physics*, 71 (2):231–303, 1987.

[121] X. D. Liu, S. Osher, and T. Chan. Weighted essentially non-oscillatory schemes. *Journal of Computational Physics*, 115(1):200–212, 1994.

[122] B. Cockburn and C. W. Shu. The Runge–Kutta discontinuous Galerkin method for conservation laws v: multidimensional systems. *Journal of Computational Physics*, 141(2):199–224, 1998.

[123] A. Kurganov, S. Noelle, and G. Petrova. Semidiscrete central-upwind schemes for hyperbolic conservation laws and hamilton–jacobi equations. *SIAM Journal on Scientific Computing*, 23(3):707–740, 2001.

[124] J. Castagna, Y. Yao, and J. Yao. Direct numerical simulation of a turbulent flow over an axisymmetric hill. *Computers & Fluids*, 95:116–126, 2014.

[125] R. L. Simpson, C. H. Long, and G. Byun. Study of vortical separation from an axisymmetric hill. *International Journal of Heat and Fluid Flow*, 23(5):582–591, 2002.

[126] P. R. Spalart. Direct simulation of a turbulent boundary layer up to $R_\theta = 1410$. *Journal of Fluid Mechanics*, 187:61–98, 1988.